EXPERIMENTAL CHARACTERIZATION OF HTGR REACTOR CAVITY GAS DYNAMICS FOLLOWING A PRIMARY SYSTEM RUPTURE

A Dissertation
Presented in Partial Fulfilment of the
Requirements for the
Degree of Doctor of Philosophy
with a
Major in Mechanical Engineering
in the
College of Graduate Studies
University of Idaho
by
Silvino Alejandro Balderrama Prieto

Approved by:
Major Professor: David Arcilesi, Ph.D.
Committee Members: Richard N. Christensen, Ph.D.; Tao Xing, Ph.D.; Michael McKellar, Ph.D.; Piyush Sabharwall, Ph.D.
Department Administrator: Gabriel Potirniche, Ph.D.

August 2022

ABSTRACT

For a High-Temperature Gas-cooled Reactor (HTGR), there is a probability that the helium pressure boundary (HPB) suffers a breach that could lead to the depressurization of the system. The helium is discharged into the cavity section of the vented low-pressure containment building, and the cavity is eventually vented under specific conditions. Under the postulated accident event, the nuclear reactor can undergo significant damage if air makes its way from the breach towards the reactor core. Even though the probability of such an event is very low, this scenario has gained the attention of regulators, plant designers, and operators because of the possible catastrophic consequences. The University of Idaho - Idaho Falls Campus designed and built a $1/20^{th}$ scaled-down HTGR based on the preliminary design of the Gas Turbine Modular Helium Reactor to analyze the gas dynamics of helium-air interaction and venting of the air located within the reactor cavity following a break on the HPB.

In this study, a sensitivity study is executed to analyze the air and helium concentration within the containment building as a result of a break in the HPB. This effort aims to shed light on the gas dynamics within the vented low-pressure containment of an HTGR during the accident, as mentioned above. Additionally, this study evaluates the system behavior under varying conditions to reduce the oxygen concentration at the location of the break to reduce the probability of air ingress. Some of the varying conditions evaluated are the time of active ventilation, break size and location, and ventilation location.

The experimental results presented in this study indicate that an active ventilation time of 22 seconds allows the system to vent most of the air from the cavity section compared to 50, 65, and indefinitely time scales. Additionally, the experimental results indicate that leaving the ventilation duct system open for too long results in lower temperatures in the cavity section. The break size also influenced the oxygen concentration, where the system vents more air with small breaks than relatively large ones. The location and orientation of the break have little effect on the temperature and oxygen concentration measurements. Nonetheless, it did significantly influence the velocity of the gases being vented. The location of the ventilation system did significantly influence the oxygen concentration. The placement of the ventilation system near the bottom floor of the power conversion vessel (PCV) containment building results in a higher oxygen concentration in the cavity region of the reactor pressure vessel and a lower concentration in the PCV cavity region. Contrarily, a lower oxygen concentration in the pressure vessel cavity and higher in the PCV is the outcome when the ventilation duct is placed near the roof of the containment building of the PCV. Velocities as a result of the initial depressurization and natural circulation were recorded. Experimental results indicate that the velocities at the bottom of the axial cross-vessel are higher than at the top.

Acknowledgements

I want to express my deep gratitude to my advisor, Dr. David Arcilesi, who supported me throughout the completion of this work. His words of encouragement and constructive criticism were vital elements that helped me to complete this study. I want to thank Dr. Richard Christensen. He was also a great asset during the execution of this effort, as he challenged my ideas to help me develop the skills necessary to perform more rigorous analyses on my experimental data.

A special acknowledgment to Alice Allen, who helped me overcome multiple obstacles and supported me most when I needed help.

I would also like to thank my family and friends, particularly my mother, Tomasa Prieto Alvarez, and my father, Silvino M. Balderrama Alvarez, for their support and encouragement. Without their support, I would not be able to achieve my dreams and goals of becoming a nuclear and mechanical engineer.

I want to acknowledge two particular colleagues/friends, Jan Lambrechtsen and Robin Roper, who helped me when I was running experiments and writing my dissertation. Their support during our weekly accountability group meetings was vital to encouraging me to continue working and meet deadlines.

Last but not least, special gratitude goes to Shirley Yong, who supported me in the good and bad times. She helped me uncountable times during the last year of my dissertation.

Dedication

This dissertation is wholeheartedly dedicated to the memory of my father, Silvino M. Balderrama Alvarez, who could not witness the completion of this work. May his soul rest in eternal peace.

TABLE OF CONTENTS

LIST OF TABLES

List of Figures

Nomenclature

$\dot{m}$	Mass flow rate
g'	Reduced gravity
g	Acceleration due to gravity
k	Thermal conductivity
k_i	Thermal conductivity of gas component i
k_j	Thermal conductivity of gas component j
k_{mix}	Thermal conductivity of a gas mixture
m	Mass
m_{vessel}	Mass of gas within vessel
r	Radius
r_m	Radius of model
r_p	Radius of prototype
t	Time
v	Velocity
v_*	Velocity at throat
v_o	Initial velocity of gas prior expansion
w	mass fraction

Capital Letters

$\dot{V}$	Volumetric flow rate

$\overline{R}$	Specific gas constant
A	Area
A_*	Area of throat/outlet
C_d	Discharge coefficient
C_p	Heat capacity at constant pressure
C_v	Heat capacity at constant volume
C_{pi}	Specific heat capacity for mixture components
D	Diffusivity
Fr_m	Froude number of model
Fr_p	Froude number of prototype
Fr_R	Ratio of prototype and model Froude number
Gr_m	Grashof number of model
Gr_p	Grashof number of prototype
Gr_R	Ratio of prototype and model Grashof number
H	Characteristic length
Ma	Mach number
MW	Molecular weight
P	Pressure
P_*	Pressure at throat
P_d	Downstream pressure
P_o	Initial pressure of gas prior expansion

P_r	Pressure ratio
P_u	Upstream pressure
P_{atm}	Atmospheric pressure
$P_{C.V.}$	Pressure in control volume
P_{vessel}	Vessel pressure
R	Universal gas constant
R_i	Specific gas constant for mixture components
Re_m	Reynolds number of model
Re_p	Reynolds number of prototype
Re_R	Ratio of prototype and model Reynolds number
Sc_m	Schmidt number of model
Sc_p	Schmidt number of prototype
Sc_R	Ratio of prototype and model Schmidt number
T	Temperature
T_*	Temperature at throat
T_o	Initial temperature of gas prior expansion
T_s	Surface temperature
T_∞	Bulk fluid temperature
T_{vessel}	Vessel temperature
V	Volume
$V_{C.V.}$	Volume of control volume

Greek Letters

β	Coefficient of thermal expansion
γ	Heat capacity ratio
μ	Dynamic viscosity
μ_{mix}	Dynamic viscosity of a gas mixture
ν	Kinematic viscosity
ρ	Density
ρ_*	Density at throat
ρ_1	Density of gas 1
ρ_2	Density of gas 2
ρ_o	Initial density of gas prior expansion
$\rho_{C.V.}$	Density of control volume
ρ_{mix}	Density of a gas mixture
ρ_{vessel}	Density of gas within vessel
σ	Standard deviation
τ	Discharge time constant

Acronyms

2D two-dimensional. 17

ALARA As Low As Reasonable Achievable. 3

AVR Arbeitsgemeinschaft Versuchsreaktor. 8

CFD Computational Fluid Dynamics. 20, 54, 56, 69, 136

CO Carbon Monoxide. 15, 16

CO$_2$ Carbon Dioxide. 15, 16

FSV Fort St. Vrain. 8

GA General Atomics. ix, 11, 12

Gen-IV Generation IV. 1

GFR Gas-cooled Fast Reactor. 1

GIF Generation IV International Forum. 1, 8

GT-MHR Gas Turbine-Modular Helium Reactor. viii, ix, 6, 12, 16, 17, 28, 33–36, 38, 42, 48, 49

HPB Helium Pressure Boundary. 2–5, 11–14, 16, 17, 28, 101, 135, 136

HTG-10 High-temperature Test Reactor. 9

HTGR High-Temperature Gas-cooled Reactor. viii, ix, xii–xiv, 1–8, 10, 11, 13–15, 18, 28, 38, 42, 45, 47–49, 68, 90, 102, 104, 105, 110, 115, 116, 124, 129, 132–134

INL Idaho National Laboratory. 15

LFR Lead-cooled Fast Reactor. 1

LOCA Loss-Of-Coolant Accident. 2, 3, 5, 10, 12, 16, 38, 124, 129, 134

LWRs Light Water Reactors. 1, 2, 10

MOOSE Multi-physics Object-Oriented Simulation Environment. 136

MSR Molten-Salt Reactor. 1

O_2 Oxygen. viii, x, 15, 16, 53–55, 62, 63, 78–80, 112, 113, 119, 121, 136

O.D. outer diameter. 43

PBMR Pebble Bed Modular Reactor. 16

PCV Power Conversion Vessel. ix–xi, xiii, 2, 7, 11, 42, 43, 46–49, 51, 52, 54–56, 67, 69, 90, 91, 94, 106, 108, 110, 112–115, 126, 127, 129, 135, 136

R&D Research and Development. 1

RB Reactor Building. ix–xiii, 2–5, 19, 20, 45, 51, 54–56, 67, 68, 74, 75, 79, 82–84, 87–93, 95–99, 103–108, 112, 113, 127, 129

RCCS Reactor Cavity Coolant System. 16

RPV Reactor Pressure Vessel. viii–xi, xiii, 2, 5, 6, 11, 12, 14, 17, 19, 29, 41–46, 48, 49, 51, 52, 67, 72, 74, 76, 77, 85, 86, 94, 104, 112, 115–118, 123, 125, 127, 129, 135, 136

SCWR Supercritical Water-cooled Reactor. 1

SFR Sodium-cooled Fast Reactor. 1

SS-316 Stainless-Steel 316. 43, 44, 47

TAMU Texas A&M University. ix, 18–20

TRISO TRi-structural ISOtropic. 7

U.K. United Kingdom. 1, 7

U.S. United States. 1, 7, 8, 16

UI-IF University of Idaho - Idaho Falls. viii, ix, 6, 38, 47–49, 59, 68, 136

USNC Ultra Safe Nuclear Corporation. 19

V&V Verification and Validation. 16

VHTR Very-High-Temperature Reactor. 1, 8, 10, 16, 17

VLPC Vented Low-Pressure Containment. x, 2–5, 12, 18, 42, 50, 55, 69, 134, 136

CHAPTER 1

INTRODUCTION

1.1 BACKGROUND

The objectives of the United States (U.S.) energy policy and the goals of the Generation IV International Forum (GIF) are interchangeable as they ultimately envision a generation of sustainable, affordable, secure, and reliable energy that can meet current and future energy needs. The GIF is an international cooperative group of researchers and policymakers that focuses on the multinational collaboration of Research and Development (R&D) on Generation IV (Gen-IV) nuclear reactor concepts. The group's effort in about ten years was to evaluate multiple nuclear reactor concepts, which aimed to meet the social, economic, and environmental requirements of the 21st century (Pioro and Duffey, 2018). The GIF identified six reactor design concepts that can help meet the world's future energy needs. These reactor concepts are: (1) Sodium-cooled Fast Reactor (SFR), (2) Supercritical Water-cooled Reactor (SCWR), (3) Lead-cooled Fast Reactor (LFR), (4) Molten-Salt Reactor (MSR), (5) Gas-cooled Fast Reactor (GFR), and (6) Very-High-Temperature Reactor (VHTR) (Pioro and Duffey, 2018). The HTGR technology, which falls within the Gen-IV VHTR design concept, has been studied for several decades. It offers multiple advantages over the already deployed fleet of Light Water Reactors (LWRs). The first-ever built HTGR was the Dragon reactor in the United Kingdom (U.K.) (Beck and Pincock, 2011). Thereafter, multiple HTGRs were designed and built-in multiple countries, including China, Japan, South Korea, the U.S., and Germany (Yan, 2016). The safety of HTGR systems was demonstrated to be significantly high, which motivated multiple entities to consider coupling HTGRs to systems for industrial processes that benefit from high outlet temperatures (e.g., hydrogen production) (GIF, 2014). Although HTGRs were demonstrated to operate safely, there is a probability of some accidents that can take place in these high-temperature systems. One potential accident scenario, which is the focus of this study, is the ingress of air into the reactor core as a result of a break on the Helium Pressure Boundary (HPB).

During the regular operation of an HTGR, the primary system is pressurized at high temperatures with helium, and the cavity of the RB contains relatively cold air, with respect to the reactor coolant (Balderrama Prieto *et al.*, 2021), at atmospheric pressure. A Loss-Of-Coolant Accident (LOCA) event representative of an HTGR is characterized as a break on the HPB that causes an excessive loss of helium coolant. The coolant is forced to exit the HPB due to the pressure difference into the cavity of the RB through the HPB breach. The hot helium mixes with the cold air in the RB cavity as the system depressurizes. Once the depressurization is complete, there is the probability of an air ingress through the original break as the pressure of the primary circuit is no longer higher than the pressure of the cavity unless countermeasures are taken. When air enters the reactor coolant primary circuit and makes its way towards the reactor core, the oxygen from the air can cause an oxidation reaction once it is in direct contact with in-core nuclear grade graphite structures and fuel elements (Ferng and Chi, 2012; Haynes *et al.*, 2017; Takeda, 2008; Alshehri *et al.*, 2021).

The RB houses several components of the nuclear reactor, including the RPV, PCV, and axial cross-vessel duct. In case of a failure in one of these components and a potential release of radioactive material, the containment building serves as a barrier to avoid releasing radioactive material into the environment. In anticipation of a possible LOCA event, the RB is equipped with a ventilation system. During the system's transient depressurization, the internal pressure of the RB cavity is expected to increase. A VLPC building is typically included in the baseline design for both prismatic and pebble-bed nuclear reactors as a countermeasure for possible pressure buildup, as opposed to the air-tight RB of LWRs, which do not have any ventilation systems (Li *et al.*, 2020). The RB ventilation system is activated whenever the pressure of the RB cavity exceeds a preset level. In the event of a LOCA, as hot helium exits the HPB, the pressure of the RB cavity increases, followed by the activation of the venting system that allows it to vent passively (Takeda, 2008). As helium occupies more space within the cavity section, the air is pushed out through the venting system to the atmosphere. After venting, the ventilation system shuts down in avoidance of a flow reversal to lower the probability of air ingress into the reactor coolant pressure boundary as the ventilation system can act as a source of fresh air.

The VLPC for HTGRs generally has a rectangular geometry, contrary to pressurized water reactors whose RB geometry is circular. While its design relies on the As Low As Reasonable Achievable (ALARA) principle (Li *et al.*, 2020; Subki, 2020), the final design of the RB can vary from reactor to reactor, including the ventilation system's placement. Ideally, the ventilation system is placed in a position that allows for optimal passive ventilation. Ultimately, the best-case scenario is to vent all the air in the RB cavity following a LOCA event to minimize the probability of air ingress into the HPB, which can result in an oxidation reaction. However, multiple conditions can dictate the probability of air ingress. A report published by Ball (2014) indicates that the factors that can significantly influence the damage of the reactor as a result of an air ingress are the location and size of the break, flow path resistances, core temperature distribution, and long term availability of oxygen in the reactor building (Ball, 2014).

This study aims to shed light on the possibility of optimizing the ventilation of the RB cavity following a break in the HPB. Particular emphasis is given to characterizing the gas dynamics of air and helium in the RB cavity during and after the depressurization of the system. Additionally, different case scenarios are evaluated to account for different flow distributions to reduce the oxygen concentration at the break's location and reduce the probability of air ingress.

1.2 MOTIVATION

While HTGRs come with multiple safety systems and are proven to operate with a high degree of safety, it is paramount to analyze potential accident scenarios to quantify better uncertainties associated with the prediction of the outcomes associated with such accidents and develop and improve the performance and safety of mitigation systems (Ball, 2014). A LOCA event in an HTGR has gained the attention of multiple research entities because of the possibility of air ingress into the nuclear reactor as a result of a break in the HPB. Although the probability of such an accident scenario is very low, it is of significant interest to regulators, plant designers, and operators as the reactor core can endure significant damage due to the oxidation reaction that occurs when oxygen from air and graphite are in direct contact (Ball, 2014).

The VLPC is the final barrier to the transport and release of radionuclides into the environment. The response of it will be driven based on the accident scene. For a slow depressurization, for instance, the air and helium can be vented while the radioactive material, if present, can be filtered (Li *et al.*, 2020). Thereafter, the ventilation of the VLPC is shut, isolating the system from the environment. In the event of a fast depressurization, the ventilation system of the VLPC opens, which results in a large amount of air and helium being vented to the environment until the pressure in the cavity is lowered to near atmospheric pressure. Thenceforth, the ventilation system closes (Hicks, 2011; Moe, 2010). In this case, a small amount of radioactive material can be vented without filtering (Li *et al.*, 2020). Albeit a wide range of studies have focused on developing tools and gathering data that can provide a better prediction of the effects of air ingress into the system and the probability of oxidation, limited information is available to the public about efforts made to optimize this system in order to vent out as much air as possible out of the RB cavity while minimizing the release of radioactive material. Additionally, information about the gas dynamics within the RB cavity is scarce as multiple studies focus on the gas dynamics within the HPB and assume initial conditions for the cavity section.

1.3 OBJECTIVES

The accurate prediction of possible outcomes from an accident scenario is paramount in the nuclear industry to develop mitigation systems and make necessary improvements to the reactor designs. For an HTGR, understanding the effects of helium/air gas dynamics within the cavity of the RB is far-reaching because an accurate prognosis can help optimize air venting and reduce the probability of air ingress.

This study expands the body of knowledge by contributing information about the gas dynamics of air and helium during and after depressurization of the pressure vessel. Characterization of the gas dynamics following an accident scenario provides insights into how to optimize the ventilation of the VLPC during accident scenarios representative of HTGRs. Additionally, the characterization of the gases within the cavity section can be insightful for future air ingress studies. The following objectives have been set to mark the efforts required to characterize the gas dynamics of the system and evaluate optimization efforts:

1. Experimentally quantify the air concentration within the VLPC for different case scenarios that involve the depressurization of the RPV through outlets of different sizes and locations in conjunction with different placements of the ventilation system.
2. Measure temperatures, pressures, and velocities of the gases during and after the transient depressurization.

It is believed that pursuing this research topic will not only fill a gap in the mitigation of accidents for HTGRs, but it will also provide more accurate conditions of the RB cavity following the depressurization of the system. The experimental data presented can be used for future studies as initial conditions to better predict air ingresses into the HPB of HTGRs.

1.4 OUTLINE

The subsequent sections of this document are arranged logically to help the reader capture a complete picture of the efforts. The following chapters of this document encompass the following:

- Chapter 2: a literature review of the overall technological progress made towards the development of HTGRs along with a survey of past studies done concerning accident scenarios representative of HTGRs, oxidation of nuclear grade graphite as a result of air ingress, and a review of numerical efforts made to model LOCA events.

- Chapter 3: describes analytical approaches used to predict the depressurization of the RPV. Additionally, this chapter provides information about efforts toward developing an analytical solution that can calculate the density difference between helium and air in the cavity section during a depressurization event. This analytical solution is complemented with a description of the prediction of the density difference of helium and air of the GT-MHR prototype.
- Chapter 4: outlines some of the efforts made towards the scaling analysis of the UI-IF HTGR. This analysis includes a description of the relevant non-dimensionless numbers in this accident scenario. This chapter also describes the experimental facility and instrumentation used to measure intrinsic and extrinsic properties of interest.
- Chapter 5: discussion of the nature of the experiments, a detailed overview of how the experimental data was collected, and information about the different focus studies.
- Chapter 6: presents the experimental results gathered in this study along with an interpretation of the data.
- Chapter 7: summarizes the results gathered, provides an interpretation of the results, and addresses limitations, assumptions, and future work.

CHAPTER 2

SURVEY OF LITERATURE

2.1 HIGH-TEMPERATURE GAS-COOLED REACTOR

The High-Temperature Gas-cooled Reactor, also referred to as HTGR, is a nuclear reactor design concept initially introduced in 1942 by Farrington Daniels (McDowell *et al.*, 2011). Daniels performed early studies at Oak Ridge National Laboratory in 1945, where he came up with a reactor design that established the basics characteristics of HTGRs, including the use of helium as reactor coolant in a direct gas turbine system, the selection of graphite as structural material and moderator, and the use of uranium carbide and thorium carbide as fissile and fertile materials (Simnad, 1991). At this time in history, it was pointed out the need to develop small units of power generation ($5 - 50$ MW$_e$) that generate electricity at a low cost, and the unit is small enough to be transported easily (Simnad, 1991). This reactor concept was later revived in the U.K. and the U.S. with the construction of experimental HTGR reactors.

In the U.K., a $20MW_{th}$ HTGR experimental reactor was built and operated between 1964 and 1975 (Beck and Pincock, 2011; McDowell *et al.*, 2011). This reactor was known as the DRAGON reactor, the first HTGR to achieve criticality without producing electricity (McDowell *et al.*, 2011). Since it did not produce electricity, the reactor design did not include a PCV nor a cross-vessel duct. The project was proposed to the European Nuclear Energy Agency in 1958 and was managed by the Organization for Economic Co-operation and Development (Beck and Pincock, 2011). During its years of operation, experiments were conducted to help accelerate the technology of gas-cooled reactors. Examples of the experiments conducted in this reactor include irradiation creep in graphite samples and the corrosion and carbon transport in the presence of impurities and irradiation (Simnad, 1991). Additionally, the Dragon reactor pioneered the use of TRi-structural ISOtropic (TRISO)-coated particle fuel (Yan, 2016).

A few years after the construction of the Dragon reactor, the U.S. built its first HTGR, the Peach Bottom Unit 1. It operated from 1966 unit 1974 to demonstrate the viability of producing electricity using this reactor concept. This reactor was the first HTGR to produce electricity and have a cross-vessel as part of its design. It successfully operated for eight years, where information was collected regarding the physics, materials and fuels, and the engineering of HTGRs (Simnad, 1991).

Germany built a pebble bed reactor, the Arbeitsgemeinschaft Versuchsreaktor (AVR), a $15MW_e$ reactor that achieved criticality in August 1966 (Simnad, 1991). The AVR performed several experiments where performance data was gathered from new fuel designs. In the U.S., a prismatic core HTGR known as the prototypical Fort St. Vrain (FSV) operated from 1976 to 1989. This prototypical reactor demonstrated steam turbine power generation at 39% thermal efficiency, and it validated the prismatic core physics with high burn-up (90 GWd/t) using thorium fuel (Yan, 2016). After deploying these nuclear reactors in the U.S. and Europe, a surge of HTGR technology emerged in Asia, mainly in China and Japan.

Fast forward, in January 2000, the GIF was founded originally by nine countries motivated by the belief that nuclear energy is required in order to meet future energy needs. International collaboration is needed to accelerate the deployment of the next generation of advanced nuclear reactors (GIF, 2014). In 2001, the GIF endorsed the VHTR design as one of the six nuclear reactor concepts suitable to meet the GIF's goals. These goals consist of:

- sustainable energy generation that meets clean-air objectives and promotes long-term availability of nuclear fuel,
- improvement on minimization and management of nuclear waste,
- have a life-cycle cost advantage over other energy sources,
- financial risk level is comparable to other energy source projects,
- enhanced safety and reliability,
- low probability of reactor-core damage,

- eliminate offsite emergency response, and
- proliferation resistance and increased physical protection against acts of terrorism.

Currently, there are two reactor core configurations available, pebble bed and prismatic core (Pioro and Duffey, 2018), where the pebble bed consists of spherical fuel particles whose overall diameter is about 1 mm. The fuel is coated using layers of carbon and ceramics. These spherical particles are then crammed in a graphite matrix until a spherical pebble roughly the size of a tennis ball is created (Yan, 2016). Generally, pebble bed reactors accommodate multiple fuel pebbles within their reactor core. For instance, the the High-temperature Test Reactor (HTG-10) has $27,000$ (Yan, 2016). The heat generated by these fuel pebbles is removed through the helium coolant that flows through the void regions formed in between pebbles. Unlike pebble bed reactors, the prismatic configuration consists of multiple prismatic blocks where the fuel rods are placed longitudinally. The helium coolant flows through these blocks in designated channels. Both reactor core designs use a graphite reflector and are enclosed in a steel pressure vessel. Figure 2.1 depicts the fuel/reactor core difference between these two reactor concepts.

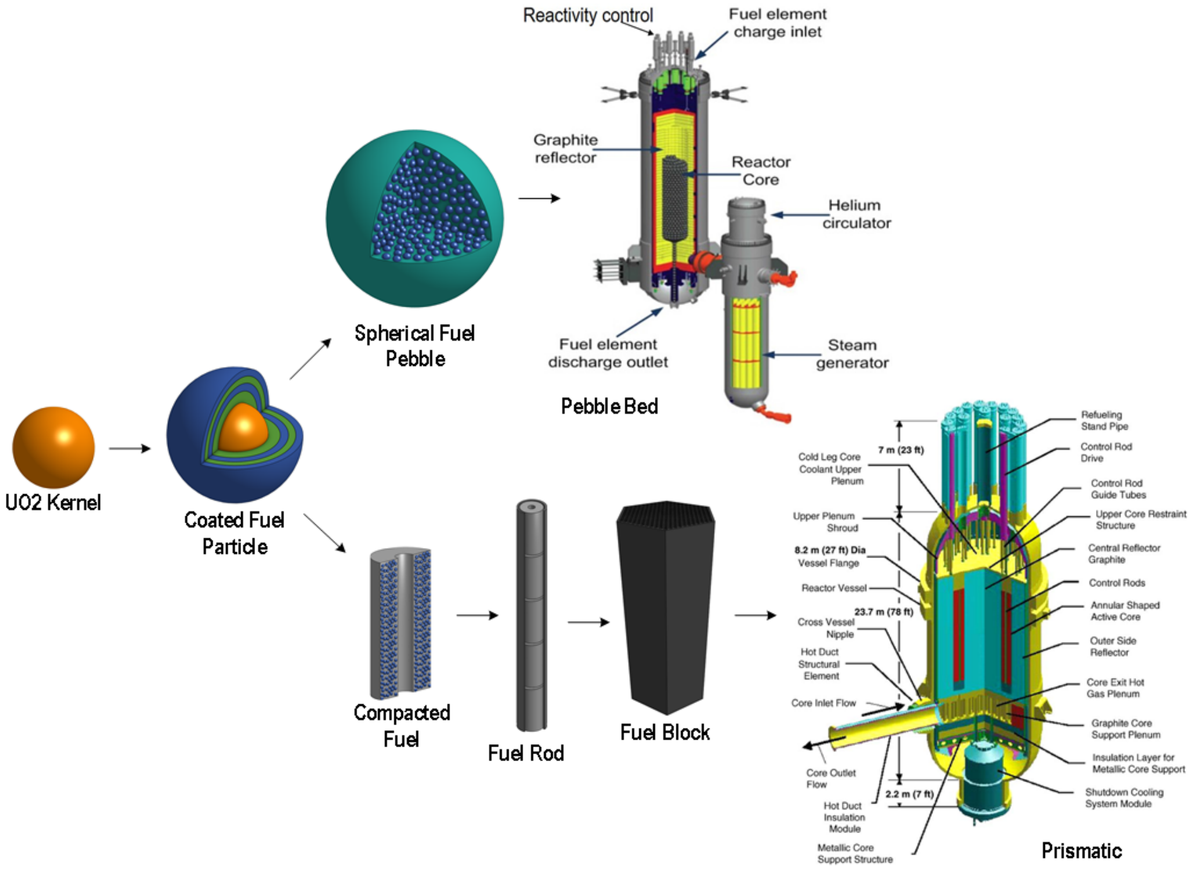

Figure 2.1: TRISO fuel loaded into a pebble bed and prismatic reactor. Schematics of the pebble bed and prismatic reactors obtained from Dong (2018) and Gauthier *et al*. (2006), respectively.

While a HTGR concept possesses multiple advantages over LWRs, multiple individuals within the nuclear industry are concerned about a possible air ingress from a LOCA event, which forms part of the design-basis accident list for VHTR (Oh, 2006; Ball *et al*., 2008).

2.2 LOSS-OF-COOLANT ACCIDENT EVENT

Pebble bed and prismatic reactor concepts are equipped with high-degree passive safety systems that minimize the probability of fission product release during normal and off-normal operating conditions, including beyond design basis events. Additionally, VHTR systems are designed to limit fuel temperatures under all plant conditions including accidents (Moses, 2010).

One potential accident scenario representative of an HTGR is air ingress due to a break on the HPB, also referred to as the primary circuit. During normal operation of the system, the RPV, PCV, and cross-vessel contain pressurized helium. Outside the HPB is the cavity section, which is generally filled with air at atmospheric pressure (Arcilesi *et al.*, 2011; Ham *et al.*, 2013; Arcilesi Jr, 2018). This cavity is enclosed by a containment building, which serves as a barrier to releasing and transporting radionuclides to the environment (Moe, 2010). A generic configuration of the previously described barriers is displayed in Figure 2.2.

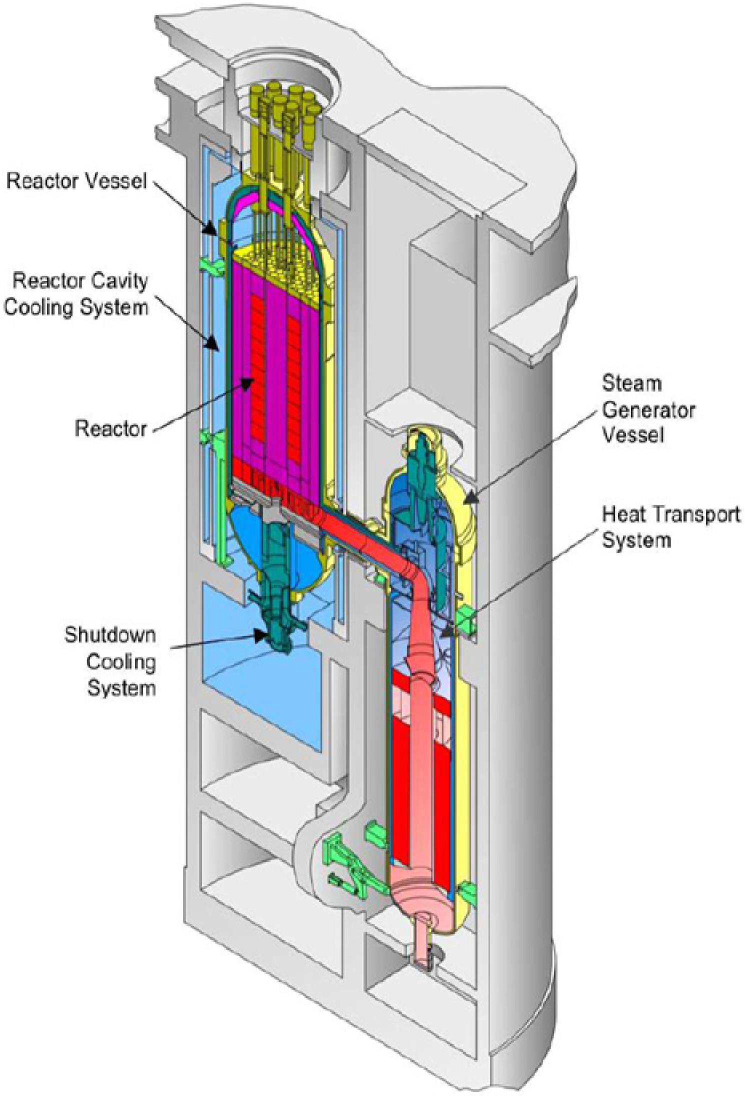

FIGURE 2.2: Schematic of GA HTGR design within its containment building (Atomics, Gerneral, 2014).

For safety purposes, a VLPC building is the baseline design of this reactor concept (Moe, 2010; Hicks, 2011). During a depressurization event, the cavity is vented using louvers that are activated whenever the pressure of the containment building exceeds preset levels. This safety mechanism allows gases from the cavity section to be vented to the environment until the cavity pressure reaches atmospheric levels, at which the louvers close (Moe, 2010; Ham *et al.*, 2013; Hicks, 2011). GA adopted this concept for their nuclear reactor design, where the containment building of the GT-MHR is equipped with a ventilation system. If the pressure of the cavity is higher by 6.89 kPa (1 psi) than the atmospheric pressure, the louvers are opened until it reaches an atmospheric pressure again (Arcilesi Jr, 2018; Ham *et al.*, 2013; Dilling *et al.*, 1994; General Atomics, 1996). Some containment building designs could potentially include dampers between the cavity of the RPV and RPV that may restrict the flow in certain areas (Moe, 2010).

During a LOCA event, a breach on the HPB is followed by a fast depressurization of the system as a result of the pressure difference between the primary circuit and the cavity section (Arcilesi Jr, 2018; Ham *et al.*, 2013). Relatively hot helium is discharged into the containment building until a pressure equilibrium is reached between the inside and outside of the HPB (Ham *et al.*, 2013; Moe, 2010). Once the depressurization process is complete, there is a possibility of air entering, initially located in the containment building, into the primary circuit, as shown in Figure 2.3. Albeit the probability of such air ingress phenomena is low (Ball *et al.*, 2008; Ferng and Chi, 2012), the chance of this happening is not zero.

The consequences of air ingress within the HPB cannot be neglected because a chemical reaction occurs when air enters in direct contact with high-temperature graphite. Upon the interaction between air and high-temperature graphite, oxidation and an exothermic chemical reaction take place, which can compromise the integrity of the reactor core (Arcilesi Jr, 2018; Oh, 2006; Ham *et al.*, 2013; Haque, 2008). For this chemical reaction to take place, in-core graphite structure and fuel should be at a temperature higher than 500^{o}C when in contact with air (Haque, 2008). Once in contact, carbon monoxide and carbon dioxide are released. Additionally, fission product release can take place from the original break as fuel elements can be damaged from

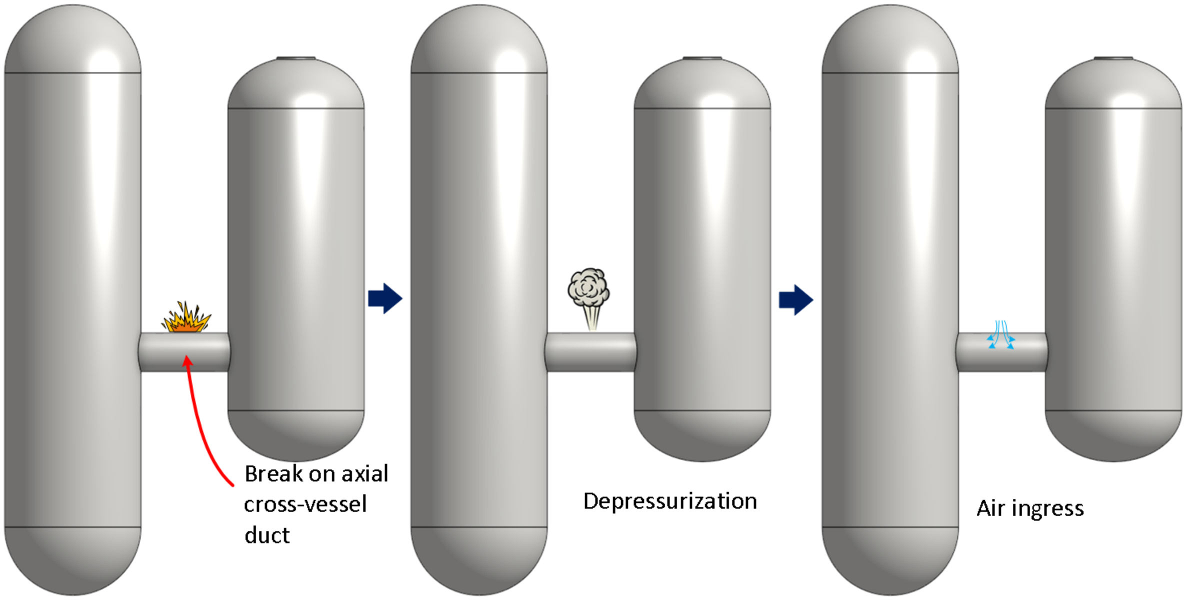

Figure 2.3: General representation of air ingress into the primary circuit of a HTGR.

the oxidation reaction (Oh, 2006; Takeda, 2008; Oh and Kim, 2010; Ferng and Chi, 2012).

Due to the detrimental consequences on the integrity of the nuclear reactor as a result of this possible accident scenario, several studies, including the present study, agree with the importance of further examining the gas dynamics of the system during and after the breach of the HPB. Consequently, multiple researchers have conducted experiments and numerical analyses to have further information about the possibility, possible consequences, and actions that can be taken to minimize the probability of air ingress. Section 2.3 summarizes some studies conducted on this accident scenario.

2.3 PAST STUDIES ON AIR INGRESS

Sensitivity studies are needed for postulated air ingress analysis, given the wide range of possible scenarios. Some factors that can influence the amount of air ingress include but are not limited to flow resistances, core temperature distribution, size, and location of the break (Ball, 2014). While a break can take place anywhere on the HPB, some sections are more likely to fail than others. Most of the studies in this subsection assume that a break occurs in the cross-vessel duct section. Although a few studies considered the possibility of a break on other sections, most of them analyze the gas dynamics of this accident scenario within the RPV. A summary of these studies is provided below.

Hishida and Takeda (1991) published a study that focused on analyzing the gas dynamics of an HTGR during and after a break in the primary pipe. This study explains that a break of the primary pipe of an HTGR is one of the design-based accident scenarios and a catastrophic one (Hishida and Takeda, 1991). Thus, the analyses focused primarily on a case scenario where the break occurs in the cross-vessel section. The accident scenario is described as a break in the cross-vessel duct, followed by an immediate depressurization of the system. Once the outside and inside pressure equalize, helium, the lighter gas, is expected to be mainly concentrated in the upper sections of the system. At the same time, the air is anticipated to be in lower sections. The air is assumed to enter the system's primary conduit and make its way towards the reactor core due to molecular diffusion (Hishida and Takeda, 1991). Experimental and numerical analyses were conducted to shed light on the gas dynamics of this system during a transient molecular diffusion air ingress event. A U-shaped tube is used for experimental purposes to mimic the internal gas channels within the reactor core, as shown in Figure 2.4. Nitrogen is used in lieu of air because it was desired to analyze the gas dynamics within this system using a two-component, He-N_2, gas mixture. The loop is kept at a constant temperature throughout the experiments as this study tries to better understand the basic features of air ingress due to molecular diffusion and natural convection of a two-component gas. The results of this study indicated that the numerical and experimental results agree with the mole fraction distribution of nitrogen within the U-shaped tube. Also, it was found that the natural circulation of nitrogen occurs once the buoyancy force is large enough to initiate this phenomenon within the facility.

In 1996, a document was published regarding a computer code developed to analyze the air ingress during the initial stages when a break occurs within the primary pipe. In this effort, a one-dimensional transient code was developed to look into the transient behavior of the gases within the HPB (Takeda *et al.*, 1996).

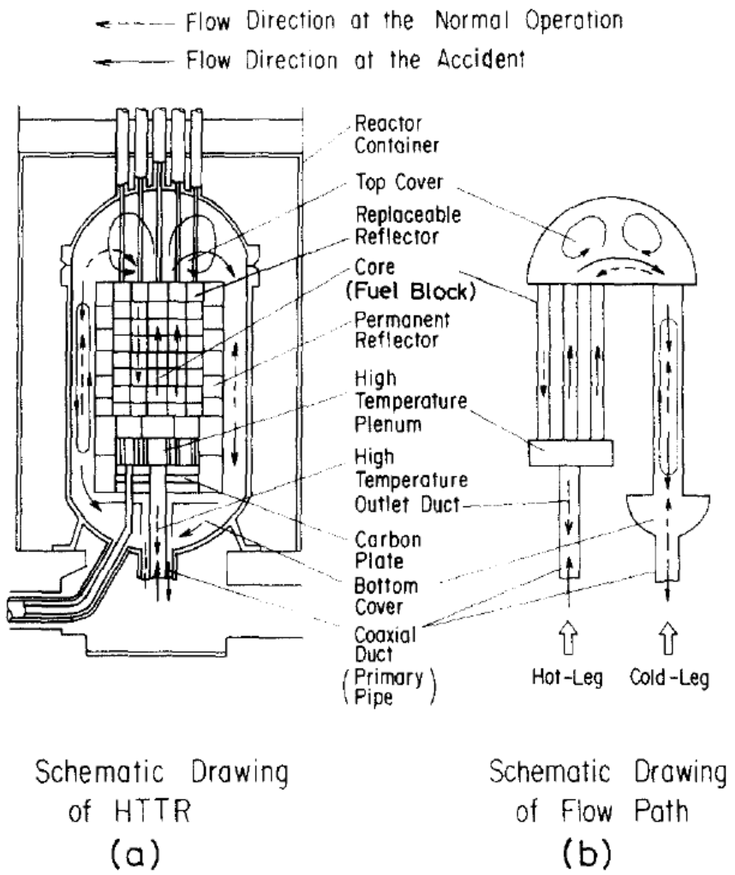

Figure 2.4: General schematic of HTGR (a), and flow path within the system (b) (Hishida and Takeda, 1991).

To validate the code, experimental data was gathered from an experimental facility equipped with a reactor core simulator, a high-temperature plenum, a water-cooled jacket that mimics the reactor vessel, and inlet and outlet pipes representing the coaxial tube. The chemical reactions taken into account are graphite oxidation and carbon monoxide combustion. The temperature of the gases was measured using 124 thermocouples, and the density of the gases, O_2, Carbon Monoxide (CO), Carbon Dioxide (CO_2), was measured at the inlet and outlet pipes. The results between the numerical and experimental data are in good agreement when comparing the density change of the gas mixture. Some differences in the calculation of the mole fractions were noted, but overall the comparison analysis yielded reasonably good results.

A report issued by Idaho National Laboratory (INL) aimed to develop and improve numerical codes that can simulate physics phenomena that take place during a LOCA event representative of a VHTR (Oh, 2006). The collaboration between the U.S. and the Republic of South Korea resulted in the development of a multi-dimensional multi-component mixture analysis code, known as GAMMA, for analyzing air ingress, the proposal of a new Reactor Cavity Coolant System (RCCS) along with experiments related to this design, neutronics models of the reactor core, improvement of safety analysis codes such as RELAP5/ATHENA and MELCOR, and the Verification and Validation (V&V) of such codes. Some of the experiments mentioned in this report aimed to understand better the gas dynamics of two different gases mixing in a closed system. Other experiments focused on testing the capabilities of the proposed RCCS design to evaluate its capability to remove heat from the cavity section using air and water.

The air ingress experiments covered in this study were performed for V&V purposes in hopes of developing models that can predict the oxidation process and the quantification of the species that result from the oxidation reaction of graphite with oxygen. The GAMMA code used in Oh (2006) modeled the behavior of the 268MW_{th} Pebble Bed Modular Reactor (PBMR), refer to Reitsma *et al.* (2006) for further information regarding this reactor design, under different conditions, including the simulation of an air ingress accident scenario following a double-ended break of the axial cross-vessel with different containment building sizes, $10\,000\,\text{m}^3$, $25\,000\,\text{m}^3$, $50\,000\,\text{m}^3$, infinite, (Oh, 2006). This sensitivity analysis studied the concentration of different gases, O_2, CO, CO_2, air ingress rate, and temperature of different sections of the reactor following a break on the HPB that resulted in a discharge of helium into the containment building and therefore its mixture with air. The case scenarios evaluated include different air volumes for the containment building. In a similar fashion, a sensitivity study was executed using the same code, GAMMA, but the reactor design evaluated is the GT-MHR. However, only one case study was evaluated, where the containment building had $50\,000\,\text{m}^3$ of air available. The results presented only cover the gas concentration of O_2, CO, CO_2, and air ingress rate. Additionally, the results of the PBMR and GT-MHR were compared against each other, and it was determined that the onset time of natural circulation of the GT-MHR is significantly delayed compared to that of the PBMR (Oh, 2006).

A study published in 2008 analyzed the oxidation rate of a $400MW_{th}$ pebble bed reactor and a $600MW_{th}$ prismatic-core modular reactor, GT-MHR, following a postulated air ingress accident scenario. The sensitivity study consisted of multiple case studies that analyzed the influence of the size of the reactor confinement, the time at which air starts entering the HPB, and the air ingress rate (Ball *et al.*, 2008). For all case scenarios, the confinement section is assumed to be initially filled with air at standard temperature and pressure conditions. For the depressurization, helium is assumed to be injected into the confinement section, which is later assumed to be well-mixed with the air. Additionally, it is assumed that this section remains at atmospheric pressure following the depressurization by considering a discharge of this mixture of air and helium. This publication reveals that an early air ingress into the primary circuit results in higher oxidation of the lower plenum. In contrast, a delayed air ingress will most likely occur in the fuel region rather than the lower plenum as it has more time to cool down. In addition, the average oxidation rate can be less for confinement with a smaller effective volume (Ball *et al.*, 2008).

In the past, molecular diffusion was considered the primary mechanism for air ingress in a VHTR. However, Kim *et al.* (2008) analyzed the possibility of density-driven stratified flow as the primary mechanism for air ingress. This study performed a numerical analysis where the GAMMA and FLUENT codes were used for such analysis. The $600MW_{th}$ GT-MHR design was used as a reference for all simulations, where the cross-vessel duct and RPV were only modeled with an infinite reactor cavity section to provide maximum air inventory. The two-dimensional (2D) simulations indicated that natural convection's onset takes about 3 to 4 minutes following the depressurization process. Additionally, the numerical results indicate that it takes about 10 minutes for the vessel to fill with air. It claims to be significantly faster than other studies considering molecular diffusion as the primary driving mechanism for air ingress. A study conducted by Takeda (2008) looked into the air ingress phenomena and developed passive safety technology that can mitigate the air ingress into the HPB and the oxidation of the graphite elements. An experimental apparatus was erected for these experiments to mimic the coolant passages within the reactor core. This study did not address the thermal-hydraulic behavior of the fluid in the cavity section, as its primary focus was the air ingress into the reactor core. This effort provided information regarding the temperature of the gas mixture and mole fraction of each gas component within a U-shaped loop with parallel heated channels under natural circulation conditions.

TAMU has performed multiple experimental and numerical analysis that focuses on analyzing the gas dynamics of helium and air in the cavity of the VLPC of an HTGR during a break accident. For such analysis, a $1/28^{th}$ scaled-down of a prototype HTGR building was designed and built on the TAMU campus. The experimental facility consists of six compartments (labeled with capital letters, A through E) as illustrated in Figure 2.5. The walls of the test facility are made of 1/2 inch thick polycarbonate sheets to facilitate the construction and installation of instrumentation. Additionally, this material can withstand relatively high temperatures and is highly transparent, allowing the usage of optical instrumentation such as particle image velocimetry, particle tracking velocimetry, and molecular tagging velocimetry (Silberberg, 2017; Yildiz, 2017; Yang *et al.*, 2018).

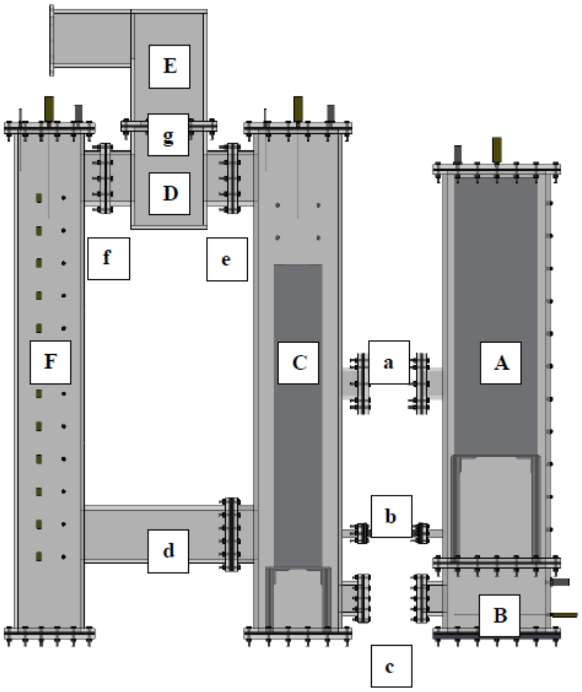

Figure 2.5: Schematic of TAMU's scaled-down experimental facility.

The experimental facility has multiple instrument ports to install thermocouples, oxygen, and pressure sensors. The instrumentation provided further information regarding mixing air and helium during a depressurization event.

In 2017, a report was released by AREVA that summarizes the results of a study that looks into the gas dynamics of the scaled-down experimental facility illustrated in Figure 2.5. This report highlights four primary objectives: identifying the main system parameters that play a significant role during the depressurization process. Additionally, it looks into the RB response during such accident events through an experimental and numerical approach. Also, the report includes information on an evaluation of the consequences of the accident scenario under consideration (Haynes *et al.*, 2017). The experimental result obtained was complemented with computer analysis. Using the CONTAIN program, the results obtained from this computer analysis were completed by Ultra Safe Nuclear Corporation (USNC) to analyze 10 accident case scenarios. Additionally, USNC developed a GOTHIC simulation of TAMU's experimental facility for benchmark purposes. The report indicates that experimental data provided further insight into the RB response during a depressurization event. The analysis conducted with CONTAIN and GOTHIC is in good agreement with experimental data. The report also mentioned some design limitations. The main constraints identified include a temperature limit of 80^{o}C at the inner surface of the RPV and a pressure limit of 1.5 psig. to preclude softening of the polycarbonate (Haynes *et al.*, 2017).

From the same experimental facility, two additional studies were published. Silberberg (2017) thesis contributed to calculating the prototype facility's leak rate and using adequate scaling analysis to compute the scaled leak rate for TAMU's experimental facility. The leak rate of the experimental facility was adjusted using needle valves. This analysis developed an analytical solution from which the analytical results were compared against the results obtained from the model. The statistical results indicate a high degree of statistical similarity. In addition, this study included five experimental runs, which were characterized to understand further the gas dynamics of a scaled-down experimental facility that undergoes a sudden depressurization event. The depressurization consisted of pressurizing one of the compartments of the experimental facility with helium to about 1 psig. A polycarbonate door clamped to the experimental facility was opened to initiate the depressurization process of the pressurized compartment. The oxygen concentration within the experimental facility was measured during this depressurization process. This study claims that the refilling process is heavily dominated by inertia during the beginning of the refilling period. It is mainly influenced by diffusion due to concentration gradients (Silberberg, 2017). These experimental results are complemented with Particle Image Velocimetry measurements, also known as PIV, to study the gas dynamics of a horizontal helium buoyant jet.

The other study developed a GOTHIC model of TAMU's scaled-down experimental facility to analyze the gas dynamics during a depressurization event. This study is divided into three phases; the first focuses on the leakage of the RB. After the depressurization process, the second phase focuses on refilling air into the RB. The third phase analyzes two hypothetical depressurization events. The computational results were compared against experimental results to evaluate the software's capability to recreate real-world phenomena. The comparison analysis yielded satisfactory results, where the computational results closely matched experimental data. As part of future work, this study recommended performing Computational Fluid Dynamics (CFD) simulations to obtain more accurate oxygen concentration results to have a deeper understanding of a Loss of Forced Cooling accident scenario (Yildiz, 2017).

CHAPTER 3

THEORY

This chapter is solely dedicated to addressing the analytical solutions developed in this study to predict the depressurization of the scaled-down pressure vessel and calculate the thermophysical properties of binary gas mixtures.

3.1 PROPERTIES OF BINARY GAS MIXTURES

For this study, it is paramount to compute the properties of a binary gas mixture, such as a helium and air mixture. Banerjee and Andrews (2007) present a set of correlations used to compute the properties of binary gas mixtures, where the density of a gas mixture, ρ_{mix}, is a function of the mole fraction of the two gases (x_1 and x_2), and their respective density (ρ_1 and ρ_2) as shown in Equation 3.1,

$$\rho_{mix} = \rho_1 x_1 + \rho_2 x_2. \tag{3.1}$$

Equation 3.1 results from applying the ideal gas law as a linear combination of the mole fraction of the gas components. The viscosity of a gas mixture, μ_{mix}, can be calculated using Equation 3.2.

$$\mu_{mix} = \mu_1 \left(1 + \frac{x_2}{x_1}\Phi_{12}\right)^{-1} + \mu_2 \left(1 + \frac{x_1}{x_2}\Phi_{21}\right)^{-1}, \tag{3.2}$$

where

$$\Phi_{ij} = \left[1 + \left(\frac{\mu_i}{\mu_j}\right)^{1/2} \left(\frac{MW_j}{MW_i}\right)^{1/4}\right]^2 \left[8\left(1 + \frac{MW_i}{MW_j}\right)\right]^{1/2}, i \neq j. \tag{3.3}$$

From above, μ represents the fluid's dynamic viscosity, and MW is the molecular weight. The thermal conductivity of a gas mixture, k_{mix}, is calculated using the relationship presented in Equation 3.4:

$$k_{mix} = k_1 \left(1 + \frac{x_2}{x_1}\Phi'_{12}\right)^{-1} + k_2 \left(1 + \frac{x_1}{x_2}\Phi'_{21}\right)^{-1}, \tag{3.4}$$

where

$$\Phi'_{ij} = 1.065 \left[1 + \left(\frac{k_i P_j}{k_j P_i}\right)^{1/2} \left(\frac{MW_j}{MW_i}\right)^{1/4}\right]^2 \left[8\left(1 + \frac{MW_i}{MW_j}\right)\right]^{-1/2}, i \neq j. \tag{3.5}$$

and

$$P_i = 0.115 + 0.354(C_{pi}/\overline{R}_i). \tag{3.6}$$

The variable k corresponds to the thermal conductivity of the fluid, C_p is the specific heat capacity, and $\overline{R}$ represents the ratio between the universal gas constant, $R = 8.3145\,\mathrm{J\,K^{-1}\,mol^{-1}}$, and the molecular weight, MW, of the gas. The correlation presented for computing a gas mixture's thermal conductivity is obtained using a kinetic theory-based formula from Mason and Saxena (1958).

The specific heat capacity at constant pressure, $C_{p,mix}$, and the specific heat capacity at constant volume, $C_{v,mix}$, for a binary gas mixture are a function of mole and mass fractions (w), respectively, as shown in Equations 3.7 and 3.8.

$$C_{p,mix} = C_{p,1}w_1 + C_{p,2}w_2. \tag{3.7}$$

$$C_{v,mix} = C_{v,1}x_1 + C_{v,2}x_2. \tag{3.8}$$

Finally, the total pressure of a gas mixture, P_{total}, is calculated by adding the partial pressures of the individual gases. This approach is known as Dalton's law of partial pressures, shown in Equation 3.9.

$$P_{total} = \sum_{i=1}^{n} P_i = P_1 + P_2 + P_3 + \ldots + P_n, \tag{3.9}$$

where P represents the pressure. The partial pressure of an individual gas, P_i, is calculated using the following relationship,

$$P_i = P_{total} x_i. \tag{3.10}$$

The thermophysical properties for pure gases, in this case for air and helium, are computed using the correlations presented in Appendix A.

3.2 ANALYTICAL SOLUTION OF A DEPRESSURIZATION PROCESS OF A PRESSURE VESSEL

Mathematical models of the vessel's depressurization were developed to predict the time the depressurization process is complete. In this section, two mathematical models were developed, where one of them assumes an adiabatic boundary condition while the other model assumes an isothermal boundary condition. Figure 3.1 shows a schematic of a pressure vessel with an outlet.

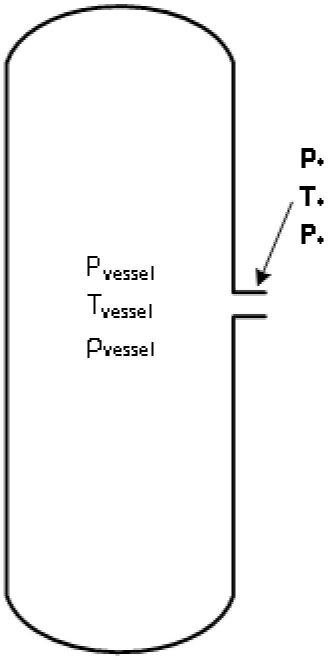

Figure 3.1: Schematic of a pressure vessel with an outlet.

One assumption adopted for the development of the analytical solution is that the velocity at the outlet is significantly larger than the velocities within the vessel during the depressurization process. One can assume that the pressure, temperature, and density while changing with respect to time, are relatively spatially uniform.

For a reversible adiabatic expansion of an ideal gas with constant heat capacity, the temperature and pressure can be calculated with the two following relationships:

$$P = P_o\Big(\frac{\rho}{\rho_o}\Big)^{\gamma}, \tag{3.11}$$

$$T = T_o\Big(\frac{\rho}{\rho_o}\Big)^{\gamma-1}, \tag{3.12}$$

from which T and ρ represent the temperature, and density, respectively. The Greek letter γ represents the heat capacity ratio, $\gamma = \frac{C_p}{C_v}$, and the subscript o is used to represent the initial state of the gas prior to expansion. Equations 3.11 and 3.12 can be used to represent the properties of the gas at the outlet as follows:

$$P_* = P_{vessel}\Big(\frac{\rho_*}{\rho_{vessel}}\Big)^{\gamma}, \tag{3.13}$$

$$T_* = T_{vessel}\Big(\frac{\rho_*}{\rho_{vessel}}\Big)^{\gamma-1}, \tag{3.14}$$

where the subscript $*$ indicates the properties of the gas at the outlet, and subscript *vessel* indicates the properties of the gas within the vessel, as shown in 3.1.

A depressurizing vessel can experience a phenomenon known as choked flow, which occurs when gas at a certain temperature and pressure passes through a constrained section, also referred to as the throat, to a lower pressure downstream section. Under certain pressure conditions, the mass flow rate of the gas passing through this throat is limited as the fluid reaches sonic conditions; velocity equals the speed of sound. Despite the upstream and downstream conditions, the flow cannot achieve supersonic conditions, velocities higher than the speed of sound, at the throat. Thus, this limiting factor is known as choked flow. Equation 3.15 is used to determine if the flow is choked,

$$P_{vessel} \geq P_{atm}\Big(\frac{\gamma+1}{2}\Big)^{\frac{\gamma}{\gamma-1}}. \tag{3.15}$$

From Equation 3.15, P_{atm} is used to indicate the atmospheric pressure, 101 325 Pa or 14.7 psi. If the vessel's pressure falls below the value computed from the right-hand-side of Equation 3.15, the flow is subsonic, and the mass flow rate of the gas leaving the vessel is lower than when the flow is choked. For sonic and subsonic conditions, different correlations are needed to compute the temperature, pressure, and density of the gas within the vessel.

From an energy and mass balance, the following correlation was derived to compute the density ratio between the throat and the vessel,

$$\frac{\rho_*}{\rho_{vessel}} = \left(\frac{2}{\gamma+1}\right)^{\frac{1}{\gamma-1}}. \tag{3.16}$$

Under sonic conditions, the velocity of the gas at the throat, v_*, is known to be the same as the speed of sound, from which it is only temperature-dependent, as shown in Equation 3.17.

$$v_* = \sqrt{\gamma \overline{R} T_*} \tag{3.17}$$

The mass flow rate at the throat can be written in the following form:

$$\dot{m} = \rho A v C_d = \rho_* A_* v_* Cd, \tag{3.18}$$

where A_* is the area of the throat, and C_d is the discharge coefficient. If we replace v_* for Equation 3.17, and ρ_* for Equation 3.16, it yields the following relationship:

$$\dot{m} = \rho_{vessel} A_* C_d \left(\frac{2}{\gamma+1}\right)^{\frac{1}{\gamma-1}} \sqrt{\gamma \overline{R} T_*}, \tag{3.19}$$

If we substitute T_* with Equations 3.14 and 3.16, the following correlation is obtained.

$$\dot{m} = \rho_{vessel} A_* C_d \left(\frac{2}{\gamma+1}\right)^{\frac{1}{\gamma-1}} \sqrt{\frac{2\gamma \overline{R} T_{vessel}}{\gamma+1}}, \tag{3.20}$$

To describe the change of mass within the vessel with respect to time, we use the following relationship:

$$\frac{dm}{dt} = -\dot{m}. \tag{3.21}$$

Knowing that the mass can be represented as $m_{vessel} = \rho_{vessel} V_{vessel}$ and replacing $\dot{m}$ for Equation 3.21, Equation 3.21 can be written as follows:

$$V_{vessel} \frac{d\rho_{vessel}}{dt} = -\rho_{vessel} A_* C_d \Big(\frac{2}{\gamma+1}\Big)^{\frac{1}{\gamma-1}} \sqrt{\frac{2\gamma \overline{R} T_{vessel}}{\gamma+1}}. \tag{3.22}$$

To simplify Equation 3.22, a new variable has been created, τ, known as discharge time constant. This constant is expressed as:

$$\tau = \frac{V_{vessel}}{A_* C_d v_o} \Big(\frac{\gamma+1}{2}\Big)^{\frac{1}{\gamma-1}+\frac{1}{2}}, \tag{3.23}$$

where v_o is the initial velocity of the gas prior to expansion. By substituting Equation 3.23 into Equation 3.22, it yields the following correlation.

$$\frac{d\rho_{vessel}}{dt} = -\frac{\rho_{vessel}}{v_o \tau} \sqrt{\gamma \overline{R} T_{vessel}}. \tag{3.24}$$

From Equation 3.17, we know that $v_o = \sqrt{\gamma \overline{R} T_o}$. Thus,

$$\frac{d\rho_{vessel}}{dt} = -\frac{\rho_{vessel}}{\tau} \sqrt{\frac{T_{vessel}}{T_o}}. \tag{3.25}$$

Equation 3.25 can be used to compute the change of density during the depressurization of the vessel. However, the temperature within the vessel can be solved through two approaches, which are discussed in the following two subsections.

3.2.1 *Adiabatic Boundary Condition*

Under adiabatic condition, the temperature of the gas within the vessel is expected drop as it expands. Heat is not added to the gas as heat transfer does not takes place on the walls of the vessel due to the adiabatic boundary condition. Hence, Equation 3.12 can be used to modify Equation 3.25,

$$\frac{d\rho_{vessel}}{dt} = -\frac{\rho_{vessel}}{\tau}\left(\frac{\rho_{vessel}}{\rho_o}\right)^{\frac{\gamma-1}{2}}. \tag{3.26}$$

By integrating Equation 3.26, it yields:

$$\rho_{vessel} = \rho_o\left[1+\left(\frac{\gamma-1}{2}\right)\frac{t}{\tau}\right]^{\frac{2}{1-\gamma}}. \tag{3.27}$$

The pressure within the vessel can be computed by combining Equation 3.11 with Equation 3.27 to obtain the following correlation,

$$P_{vessel} = P_o\left[1+\left(\frac{\gamma-1}{2}\right)\frac{t}{\tau}\right]^{\frac{2\gamma}{1-\gamma}}. \tag{3.28}$$

In a similar fashion, the temperature of the gas within the vessel can be computed by combining Equations 3.12 and 3.27 to obtain the following relationship,

$$T_{vessel} = T_o\left[1+\left(\frac{\gamma-1}{2}\right)\frac{t}{\tau}\right]^{-2}. \tag{3.29}$$

3.2.2 *Isothermal Boundary Condition*

By assuming an isothermal boundary for the inner walls of pressure vessel, the temperature of the gas within the vessel is assumed to remain relatively constant due to the assumed boundary condition, $T_{vessel} = T_o$. This condition simplifies Equation 3.25 as shown in Equation 3.30,

$$\frac{d\rho_{vessel}}{dt} = -\frac{\rho_{vessel}}{\tau}. \tag{3.30}$$

Integrating Equation 3.30, it yields the following correlation for the density.

$$\rho_{vessel} = \rho_o e^{-\frac{t}{\tau}}. \tag{3.31}$$

The above equation can be used to calculate the change of pressure using the ideal gas equation, which results in the following correlation:

$$P_{vessel} = P_o e^{-\frac{t}{\tau}}. \tag{3.32}$$

3.3 ANALYTICAL APPROACH TO CALCULATE THE HELIUM AND AIR DENSITY IN CAVITY SECTION

For this study, it is imperative to have a clear and deep understanding of the gas dynamics inside and outside of the HPB during a break of the same. Thus, this section focuses on developing an analytical solution to predict the thermophysical properties of the gases in the cavity section of the HTGR.

During regular operation, the reactor core of the GT-MHR is pressurized with helium at 7.07 MPa at the core upper plenum inlet section with an active core pressure drop of 0.051 MPa. The helium enters the reactor core with a temperature of 491^{o}C and exits at a temperature of 850^{o}C (General Atomics, 1996). While this reactor concept is designed to withstand high temperatures and pressures, there is still a probability of failure. A break of the HPB results in the hot helium's discharge into the reactor building cavity. The pressure of the cavity section, which is filled initially with relatively cold air, is at atmospheric pressure. The helium is anticipated to exit from the system in the form of a jet and mix with the cold air. The density of helium changes as it moves from the primary circuit to the throat of the break to the cavity section. Section 3.2 addresses how to compute the gas density within a vessel and at the throat of the outlet. Some studies covered in the literature review have calculated the density difference between helium and air. While the initial conditions of air may vary a little bit from study to study, the initial conditions of helium during the accident scene can change significantly based on where the break takes place. During the development of this study, a methodology has not been identified yet that addresses how to compute the temperature, pressure, and density of helium right after it leaves the HPB. Thus, a new analytical approach is presented below.

The containment building design is equipped with a ventilation system that is activated whenever the pressure in the cavity increases by 1 psid (General Atomics, 1996; Arcilesi Jr *et al.*, 2015). Thus, one can assume that when a break of the HPB takes place, the primary loop depressurizes while the containment building pressurizes. The pressurization of the containment building will continue until it reaches a 1 psid. Based on this information, an analytical solution can be developed to quantify the depressurization of the primary loop of the reactor and the pressurization of the containment building. The problem at hand can be visualized as two volumes connected, as shown in Figure 3.2. The volume on the left-hand side represents the RPV fluid region, the volume on the right-hand side is the fluid region of the containment building, and the connection between both represents the break.

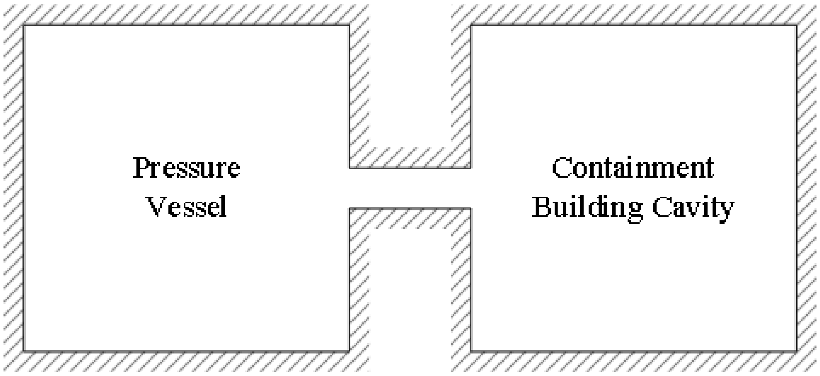

Figure 3.2: Control volumes.

For this analysis, the gases, helium and air, are assumed to be ideal gases, and the flow through the break is approximated as isentropic. The change of mass in a control volume can be represented using Equation 3.21. By replacing the mass flow rate for $\dot{m} = \rho A v$, and the mass for $m = \rho V$, it yields the following correlation,

$$\frac{d\rho_{C.V.}}{dt} = \pm\frac{\rho_* A_* v_*}{V_{C.V.}}. \tag{3.33}$$

The subscript $C.V.$ depicts the control volume. The process determines the ± sign ahead of the term on the right-hand side. For pressurization, a plus sign, "$+$", is used. A negative sign, "$-$", is used for a depressurization process. The density at the throat, ρ_*, can be calculated using Equation 3.34 if an isentropic flow is assumed,

$$\rho_* = \rho_u \Big[1 + \Big(\frac{\gamma-1}{2}\Big) Ma^2\Big]^{-\frac{1}{\gamma-1}}, \tag{3.34}$$

where ρ_u represents the upstream density. The absolute temperature at the throat, T_*, is computed using the following relationship,

$$T_* = T_u \Big[1 - \Big(\frac{\gamma-1}{2}\Big) Ma^2\Big]^{-1}. \tag{3.35}$$

From Equations 3.34 and 3.35, the variable Ma represents the Mach number. The variable T_u represents the upstream temperature. The Mach number can be computed based on the flow conditions. If the flow at the throat is choked, the Mach number is assumed to be $Ma = 1.0$. For subsonic flow, a correlation is needed. The following approach was adopted to compute the Mach number:

- *Choked Flow*: $Pr \geq \left(\frac{\gamma+1}{2}\right)^{\frac{\gamma}{\gamma-1}}$

$$Ma_i = 1.0$$

- *Subsonic Flow*: $Pr \leq \left(\frac{\gamma+1}{2}\right)^{\frac{\gamma}{\gamma-1}}$

$$Ma_i = \left\{ \frac{2}{\gamma - 1} \left[\left(\frac{P_{u,i}}{P_{d,i}} \right)^{\frac{\gamma-1}{\gamma}} - 1 \right] \right\}^{\frac{1}{2}},$$

where Pr is the pressure ratio between the upstream pressure, P_u, and downstream pressure, P_d ($Pr = P_{u,i}/P_{d,i}$). The subscript "i" represents the time step. With the correlations presented above and knowing that the velocity can be computed using Equation 3.17, the change of density within the control volume with respect to time can be solved using a finite-difference approximation. The change of pressure can be calculated using a polytropic correlation. This correlation is shown in Equation 3.36.

$$P_{C.V.,i+1} = P_{C.V.,i} \left(\frac{\rho_{C.V.,i+1}}{\rho_{C.V.,i}} \right)^{n_i}. \tag{3.36}$$

The variable n depicts the polytropic index. The temperature change is computed using the ideal gas law equation as shown below.

$$T_{C.V.,i+1} = \frac{P_{C.V.,i+1}}{\overline{R} \rho_{C.V.,i+1}}. \tag{3.37}$$

Before developing an analytical approach, it is essential to address the gas mixture in the cavity section. So far, the correlations presented assume a single gas. While the depressurization of the pressure vessel only requires accounting for the gas located in the control volume, the pressurization of the cavity section requires additional relationships to compute the density and pressure of the gas mixture. These correlations are addressed in Section 3.1. A flowchart diagram is shown in Figure 3.3 to provide a clear description of the process followed in computing the properties of helium during a depressurization event.

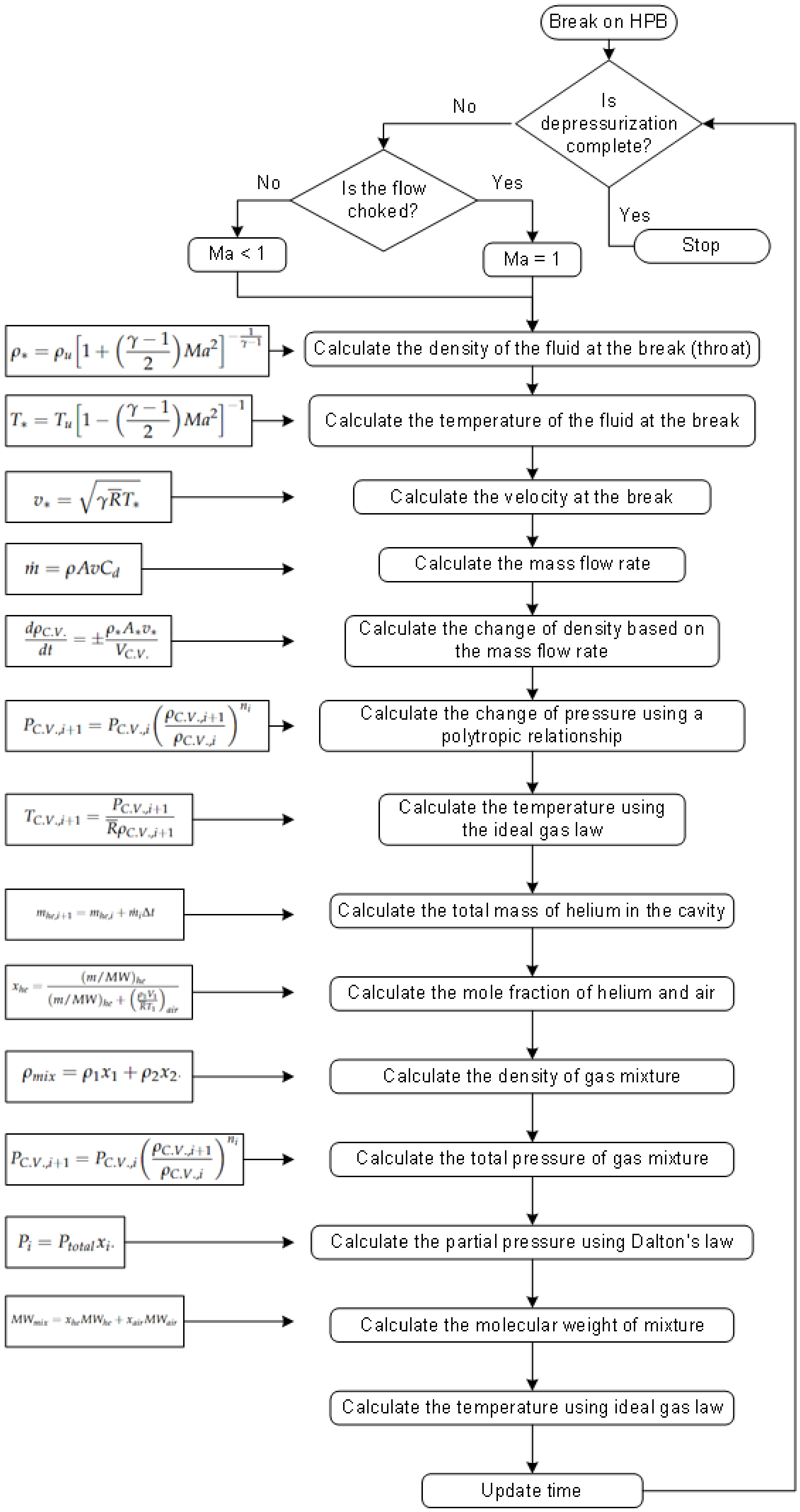

Figure 3.3: Flowchart of the calculation procedure of the depressurization and pressurization process.

3.4 PREDICTION OF ACCIDENT SCENARIO

Sections 3.2 and 3.3 primary focus on the development of analytical solutions that can be used to recreate certain conditions. In this section, the analytical solutions will be employed to calculate the rate of change in pressure, temperature, and density within the pressure vessel of the GT-MHR. Additionally, an attempt is carried out to quantify the density of helium upon its discharge into the free volume of the containment building. The initial conditions of the GT-MHR assumed for this analysis are summarized in Table 3.1.

Table 3.1: GT-MHR values used for the analytical solution of the depressurization event (General Atomics, 1996).

Section	**Free volume (m^3)**	**Species Composition**	**Pressure (MPa)**	**Temperature (^oC)**
Primary Circuit	1063.13	100% Helium	7.07	850
Cavity	7362.38	100% Air	0.101	250

The free volume of the primary circuit was calculated based on the total helium mass inventory, mass flow rate, and volumetric flow rate, $\dot{V}$.

$$\dot{m} = \rho \dot{V} = \frac{m}{V}\dot{V}. \tag{3.38}$$

Knowing that there is 10 000 lbm (4536 kg) of helium, the mass flow rate of helium is $320\,\mathrm{kg\,s^{-1}}$ (General Atomics, 1996), and assuming a volumetric flow rate of $75\,\mathrm{m^3/s}$, the total free volume of the primary circuit is $1063.125\,\mathrm{m^3}$.

Based on the information presented in Table 3.1, multiple case scenarios were analyzed. These case scenarios consist of a depressurization event, where the primary loop of the reactor is initially filled with helium. The depressurization process was calculated using polytropic correlations, where the polytropic index is assumed to have a value of 1.0 (isothermal). This assumption assumes an isothermal process. The helium from the system is discharged into the cavity of the containment building, which is assumed to be filled with air only. Temperature stratification is anticipated in the cavity section. However, this analysis assumes a uniform temperature for simplicity purposes. During the depressurization, the containment building pressure is expected to increase as helium is discharged.

Additionally, the containment building is anticipated to be air-tight sealed. This changes when the pressure of the cavity has a 1 psid. with respect to atmospheric pressure. Thus, it is fair to assume that during the depressurization event, mass conservation of helium and air is preserved. The helium in the cavity is assumed to mix with air instantaneously to have a homogeneous mixture. The pressurization of the cavity is assumed to undergo an isothermal process. In this study, the heat loss through the walls of the cavity section is neglected. While the case studies covered in this analysis have the same initial conditions, the break size diameter varies from 1 to 15 inches. The depressurization of the primary circuit for the different case studies is shown in Figure 3.4.

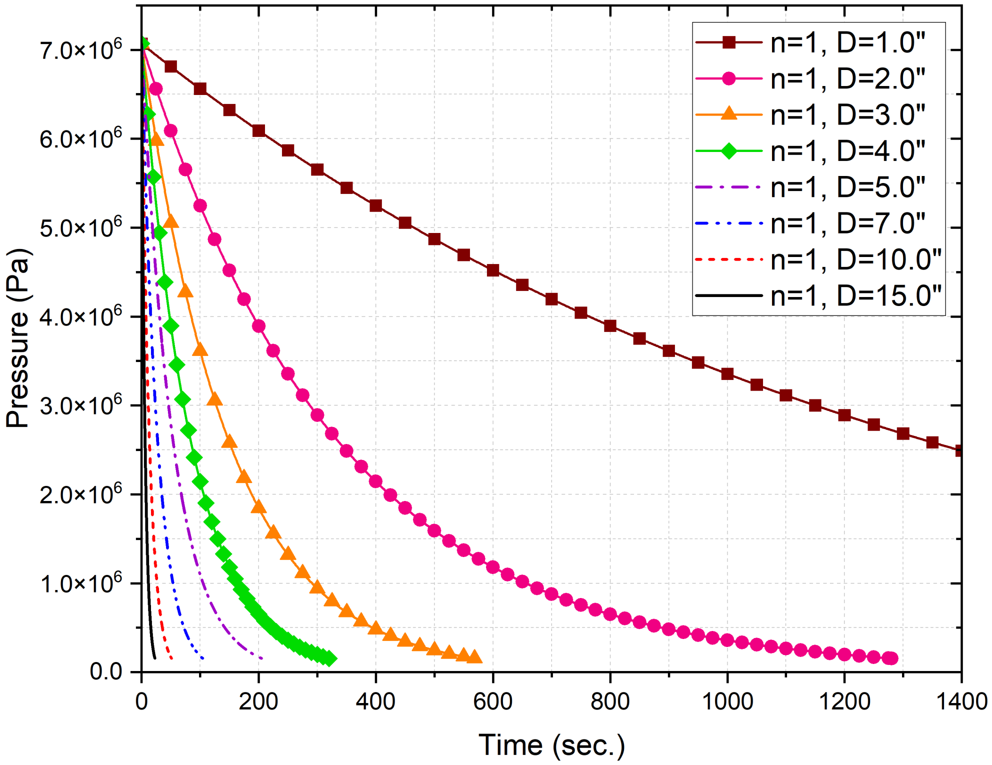

Figure 3.4: Depressurization of the GT-MHR primary circuit for different break size diameters.

As expected, the depressurization of the system is slower with a smaller break size. The rate at which the system pressurizes can help determine how fast the cavity pressurizes due to the helium discharge. Figure 3.5 shows the pressurization of the cavity during the accident event.

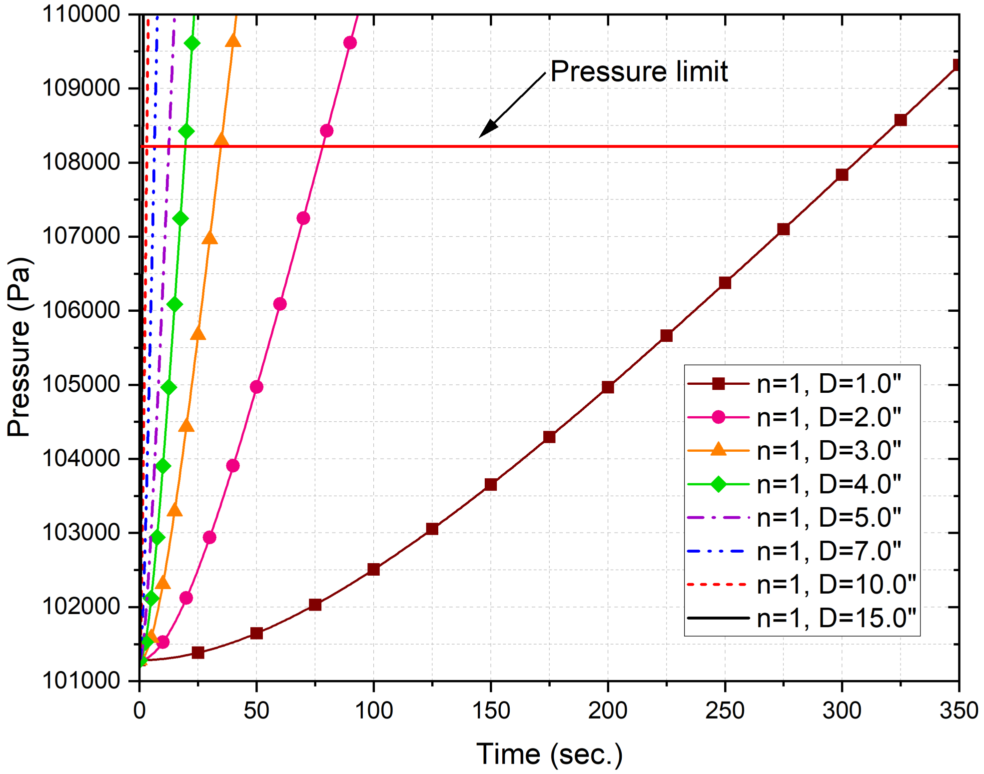

FIGURE 3.5: Pressurization of the GT-MHR containment building cavity for different break size diameters.

Previously, it was mentioned that the ventilation system of the containment building would activate when its pressure is 1 psi higher than the atmospheric pressure. This pressure threshold is illustrated in Figure 3.5 as a form of a solid red line. In an actual accident scenario, the ventilation system will activate, allowing the cavity section to depressurize. The analytical solution developed in this study did not consider the cavity's ventilation, which explains why the pressure of the cavity continues to increase beyond the preset pressure limit displayed in Figure 3.5. The timing at which the ventilation system is actuated is of great importance because the density of the gas mixture changes during the ventilation process. Thus, one can assume that the density computed using this analytical approach from the initial break until the time the cavity starts being vented can be used to estimate the density difference between air and helium. Figure 3.6 shows the calculated density evolution of air and helium within the cavity section of the system during the depressurization process.

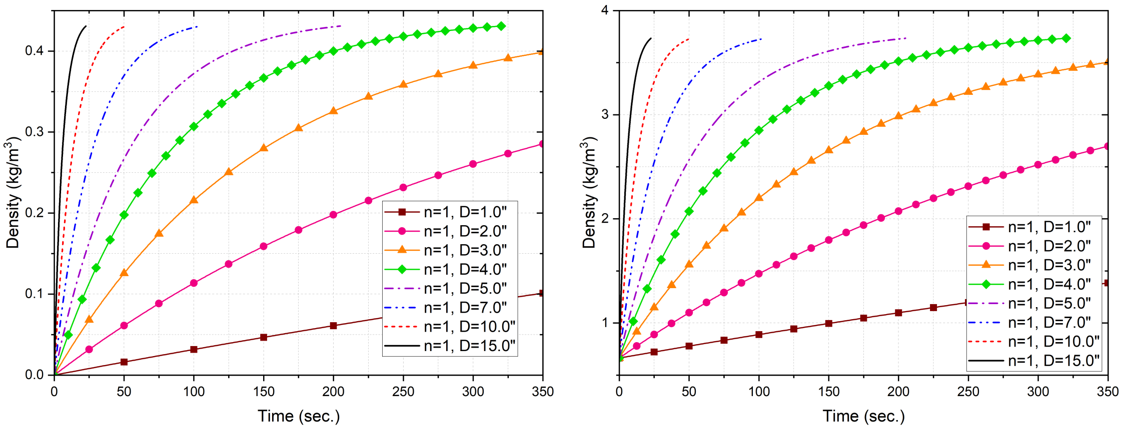

FIGURE 3.6: Helium (left) and air (right) density evolution in the cavity section during the depressurization process.

For scaling purposes, the density difference, $\Delta\rho/\rho_1$, is needed to know what the helium and air density difference is in the cavity of the model, also known as the scaled-down facility, with respect to the GT-MHR, also known as the prototype. Hence, the density difference of the prototype during an accident scenario with different breaks is computed and plotted in Figure 3.7.

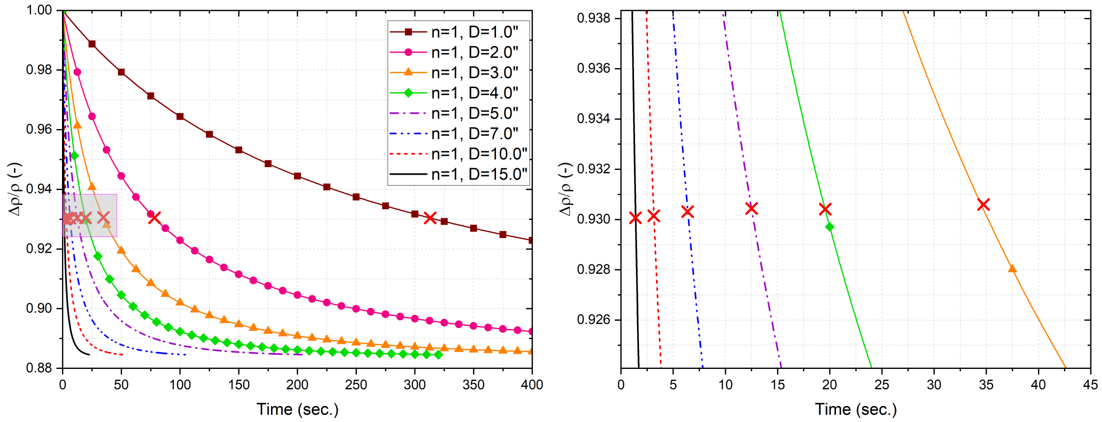

FIGURE 3.7: Density difference between helium and air in cavity section (left). Zoomed section (right) with red crosses indicating the time at which the ventilation system is anticipated to be opened.

While the density difference for the scenarios presented above change at different rates during the depressurization process, the density difference when the ventilation system is actuated is very similar to each other, $\Delta\rho/\rho_1 = 0.93036 \pm 2x10^{-4}$. Chapter 4 provides further insight into the relevance of the density difference of the prototype with respect to the model.

CHAPTER 4

SCALING AND DESIGN OF EXPERIMENTAL FACILITY

The objectives outlined in chapter 1 require an experimental facility to conduct experiments. For this particular research study, a $1/20^{th}$ scale of the GT-MHR was designed and built at UI-IF. The scaled-down HTGR experimental facility was designed with some features to increase the facility's versatility in recreating different LOCA case scenarios. The following subsections provide an overview of the experimental facility and the instrumentation used to measure temperature, pressure, velocity, and oxygen concentration.

4.1 SCALING ANALYSIS

UI-IF campus designed and built a $1/20^{th}$ scaled-down experimental facility of a HTGR. The design is based on the conceptual design of the GT-MHR. To preserve thermal-hydraulic similarity to the full-size design, a scaling analysis was performed following the methodology presented in Reyes Jr *et al*. (2010); Ishii *et al*. (1998).

The scaling analysis aimed to preserve quantities of interest for a LOCA event for a HTGR. Some of these non-dimensional numbers must be preserved to maintain similarity between the prototype and the experimental facility. Thus, the non-dimensional numbers of interest were set to unity,

$$\Psi_R = \frac{\Psi_m}{\Psi_p} = 1, \tag{4.1}$$

to ensure flow similarity. One non-dimensional number of interest is the Reynolds number, Re. The Reynolds number of the fluid leaving the vessel through the break can be computed to estimate the radius of the brake size for the model, r_m. The flow at the break should be choked at the beginning of the depressurization process. Thus, the velocity of the helium jet can be computed using Equation 3.27. The model's radius can be calculated using Equation 4.2,

$$Re_R = \frac{Re_m}{Re_p} = 1 \rightarrow r_m = \frac{(\rho v r/\mu)_p}{(\rho v/\mu)_m}. \tag{4.2}$$

The ratio of the Froude number, Fr, of the prototype and model was set to unity to solve for the density difference of the gaseous mixture in the cavity section as shown in Equation 4.3,

$$Fr_R = \frac{Fr_m}{Fr_p} = 1 \rightarrow g'_m = \frac{(v^2/Hg')_p}{(v^2/H)_m}, \tag{4.3}$$

where,

$$g' = g\Big(\frac{\rho_1 - \rho_2}{\rho_1}\Big), \tag{4.4}$$

From above, H is the characteristic length, which for this study is described as the distance between the mid-height of the axial cross-vessel and the roof of the pressure vessel cavity, g is the acceleration due to gravity, g' is the reduced gravity, ρ_1 and ρ_2 are the densities of the two gases that will mix.

Similarly, the Schmidt number is a non-dimensional number that characterizes the ratio of momentum and mass diffusivity. The material is transported due to the mean motion through the convection process and by the random thermal motion of the molecules within the fluid through diffusion. The ratio of this dimensionless number is written as follows:

$$Sc_R = \frac{Sc_p}{Sc_m} = \frac{(\mu/\rho D)_p}{(\mu/\rho D)_m}, \tag{4.5}$$

where D represents the molecular diffusivity. The theoretical molecular diffusion time scale for gas pairs of non-polar, non-reacting molecules, D_{AB}, is computed using the following relationship (Chapman and Cowling, 1990),

$$D_{AB} = \frac{1.8583x10^{-7}\sqrt{T^3\Big[\frac{1}{MW_A} + \frac{1}{MW_B}\Big]}}{P\sigma_{AB}^2\Omega_D}, \tag{4.6}$$

where σ_{AB} is the collision diameter (Lennard–Jones parameter) in Å, T is the temperature in Kelvin, the molecular weight, MW, is expressed in $kg/kmol$, the absolute pressure P is in atm, and Ω_D is the collision integral. The collision diameter and collision integral are computed using the following two relationships along with the values displayed in Table 4.1,

$$\sigma_{AB} = \frac{1}{2}(\sigma_A + \sigma_B), \tag{4.7}$$

$$\frac{KT}{\varepsilon_{AB}} = \sqrt{\left(\frac{\varepsilon_A}{K}\right)\left(\frac{\varepsilon_B}{K}\right)}. \tag{4.8}$$

Table 4.1: Intermolecular force parameters values and the collision Integral based on the Lennard-Janes Potential.

Gas	σ **(Å)**	$\frac{\varepsilon}{K}$ **(K)**
Helium	2.576	10.2
Air	3.617	97.0

Figure 4.1 shows the calculated diffusion coefficient of air and helium at different temperatures.

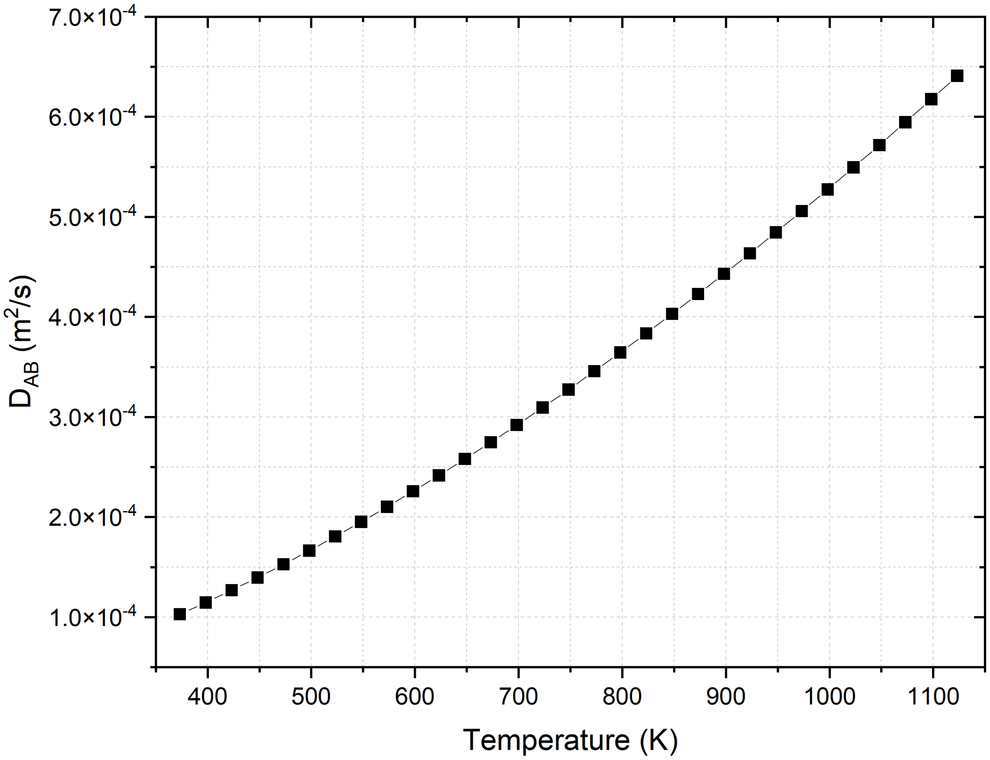

Figure 4.1: Binary diffusion coefficient of air and helium.

The Grashof number, *Gr*, is a dimensionless number of interest when looking into the buoyancy ratio to viscous forces. This dimensionless number gains relevance as the motion is driven due to density differences resulting from temperature differences. The role of the Grashof number in natural circulation is similar to the Reynolds number in forced convection. The ratio of the *Gr* is displayed in Equation 4.9,

$$Gr_R = \frac{Gr_p}{Gr_m} = 1 = \frac{[g\beta(T_s - T_\infty)H^3/\nu^2]_p}{[g\beta(T_s - T_\infty)H^3/\nu^2]_m}, \tag{4.9}$$

where ν is the kinematic viscosity, T_s is the surface temperature, and T_∞ is bulk temperature. The characteristic length for the Grashof number is different from the characteristic length of the Froude number. In this case, the characteristic length is considered from the top to the bottom of the cavity section of the RPV.

The Rayleigh number, *Ra*, is a dimensionless number used whenever natural convection is analyzed. Ideally, the model and prototype Rayleigh number ratio should be close to unity, but it is anticipated to be noticeably different. However, the magnitude of this dimensionless number can be a good indication of whether the natural convection boundary layer is laminar or turbulent. The transition from laminar to turbulent occurs when $Ra \approx 1x10^9$. This dimensionless number can be described as the product of the Grashof number and the Prandtl number, *Pr*, as shown below,

$$Ra = GrPr, \tag{4.10}$$

where the Prandtl number is described as the relationship between the momentum diffusivity and thermal diffusivity,

$$Pr = \frac{\mu C_p}{k}. \tag{4.11}$$

During the initial stages of the depressurization process, the gases in the cavity are mainly driven due to force convection; however, the inertia flow will dissipate eventually, leaving natural circulation as the primary flowing mechanism (Balderrama Prieto *et al.*, 2021). Thus, the Richardson number, *Ri*, represents the importance of the natural convection relative to the forced convection. It is mathematically expressed as,

$$Ri = \frac{Gr}{Re^2}. \tag{4.12}$$

The results of the scaling analysis and the description of the scaled-down facility are presented in the following sections.

4.2 EXPERIMENTAL FACILITY

The experimental facility discussed in this section was derived from the GT-MHR reactor conceptual design (General Atomics, 1996) with some changes to the design. The rationale behind the decision to build a $1/20^{th}$ scaled-down facility was due to space, budget, and fabrication considerations. Figure 4.2 displays the University of Idaho $1/20^{th}$ experimental facility.

FIGURE 4.2: University of Idaho $1/20^{th}$ scaled-down HTGR (front view).

The model is comprised of the following key components: a pressure vessel also referred to as RPV, a power conversion unit also known as PCV, a VLPC containment building, a pneumatic piston, and a ventilation duct. The pressure vessel is an ASME-certified vessel that resembles the RPV. It has an overall height of 47.5 inches from head to head with an outer diameter of 16 inches and wall thickness of $\frac{3}{16}$ of an inch. Its functionality was verified up to 3 MPa (435 psig.) and 810.9 K (1000^{o}F). The pressure vessel has seven outlet ports, as shown in Figure 4.3, that mimic different breaks at different heights and elevations. Six ports were welded on the vessel's lateral side, while one was positioned at the top of the vessel (refer to Figure 4.7).

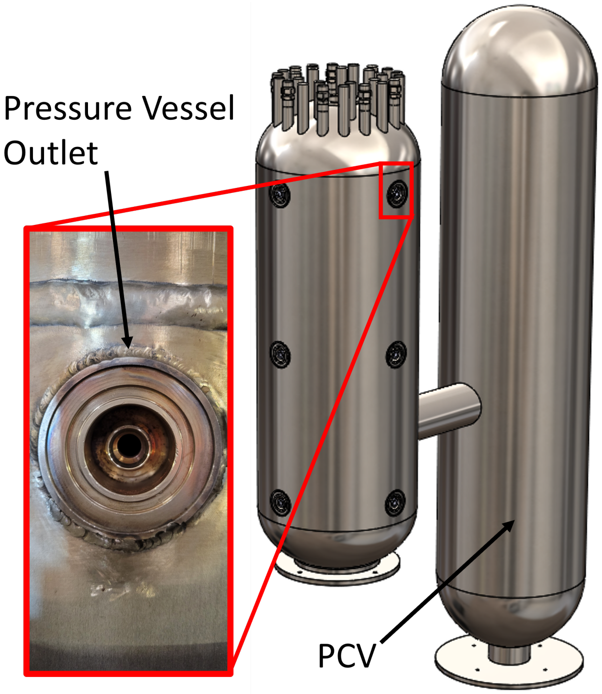

Figure 4.3: 3D CAD of the pressure vessel with 7 outlet ports and PCV.

These outlets consist of a 2.63 inch outer diameter (O.D.) small plate with a 0.50 inch Stainless-Steel 316 (SS-316) Swagelok fitting that allows the installation of thermocouples or a plug as needed. A total of six small plates, refer to Figure 4.4, were welded on the lateral wall of the pressure vessel. At the top of the same, a large plate whose O.D. is 4.5 inches was welded. This larger plate also has a 0.50 inch SS-316 Swagelok fitting welded to the plate.

The outlet chosen to mimic the break is capped and uncapped using a pneumatic piston with a metallic plug, refer to Figure 4.5. This piston is mounted to a plate and bolted down to the containment building wall facing the outlet. To plug the outlet of

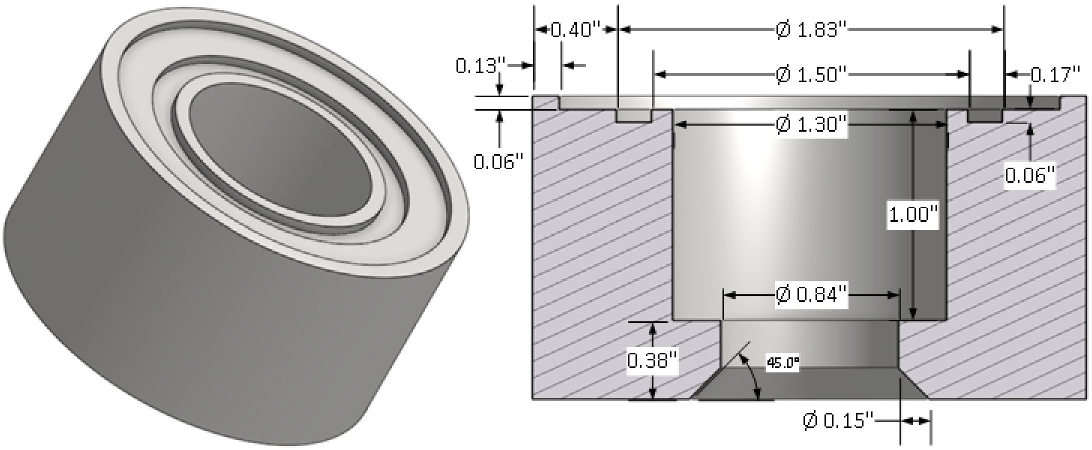

FIGURE 4.4: Schematic of a small plate with a cross-sectional view indicating its dimensions in inches.

the pressure vessel, pressurized air pushes and extends the metallic rod. This rod has a plug with a high-temperature gasket attached to the frontal face to seal the outlet properly.

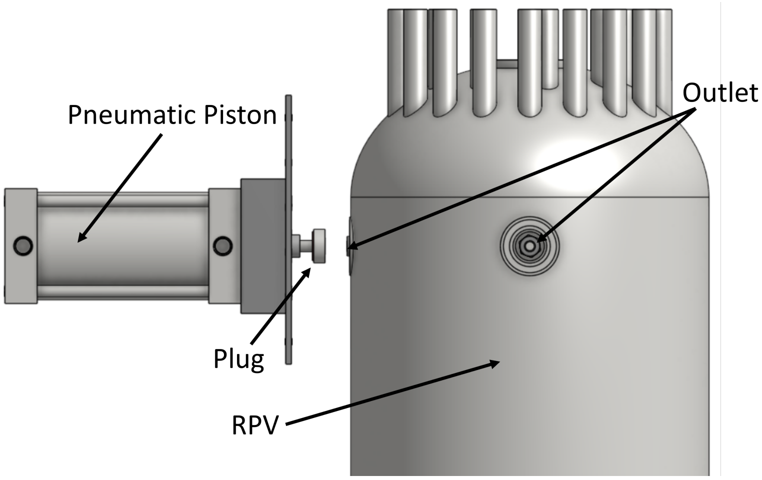

FIGURE 4.5: Schematic of pneumatic piston (left) aligned to an outlet of the RPV.

At the bottom of the vessel, a $\frac{1}{2}$ inch SS-316 Swagelok fitting was welded so a manifold could be installed. Figure 4.6 shows the manifold along with a P&ID that illustrates the instrumentation placement along with the location of the gas and vacuum lines.

To mimic the control rod drives, the SS-316 vessel counts with multiple pipes at the top of the vessel head. Nine of these pipes have a Swagelok fitting to fasten $\frac{3}{4}$

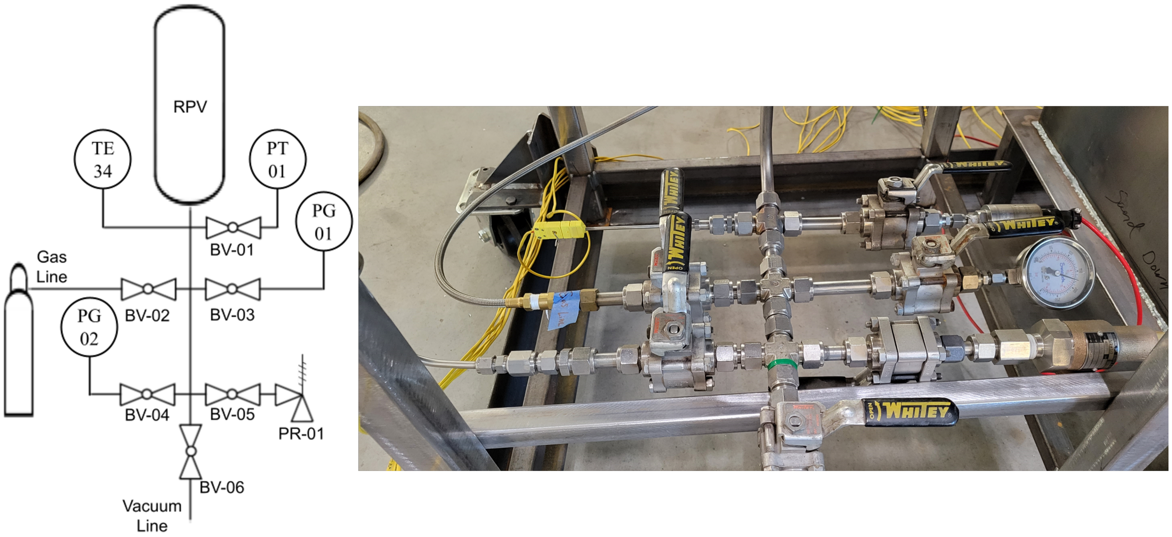

FIGURE 4.6: Manifold of the scaled-down HTGR (right) with its corresponding P&ID (left).

inch electric heater rods into the ports. These heater rods have a diameter of 0.75 inch and a total length of 43.5 inches with a 10-inch cold section at the top. They were manufactured to produce 1500 W at 240 V. Figure 4.7 shows the top view of the RPV containment building with the top lid uncap showing one outlet and some of the electric heaters.

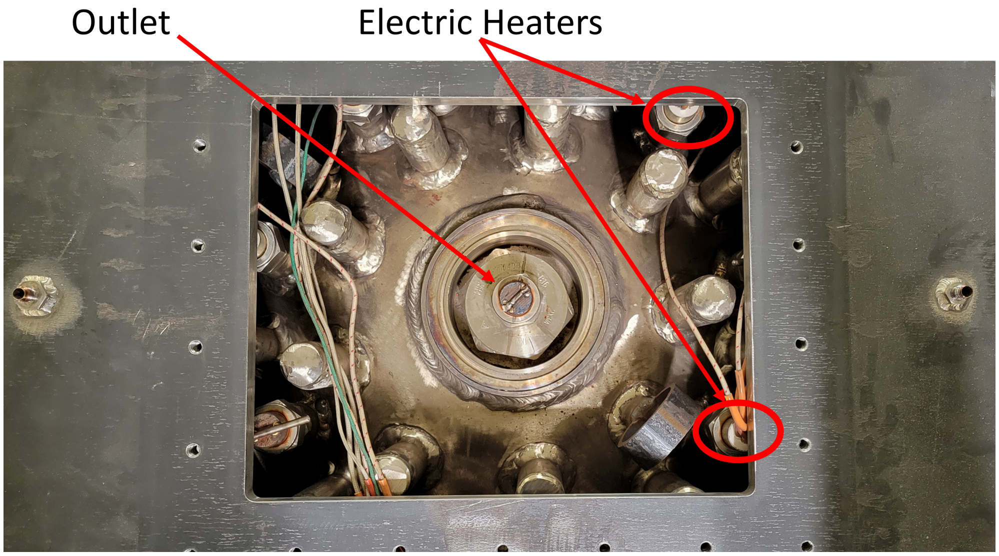

FIGURE 4.7: Top view of the RB with top lid open showing the five electric heaters installed.

The scaled-down facility had only five electric heaters installed, from which only four were used. These four electric heaters were connected in parallel. To adjust the power level of the heaters, a variable transformer was connected to them. The manually-operated VEVOR 220V AC variable transformer has a graduated dial that can be used to adjust the output voltage from $0 - 300V$. During the heating stage of the experiments, the variac is powered up. The dial of the variac is adjusted accordingly via a guess-and-check method. In the beginning, a low voltage is applied to the heaters. The voltage is increased/decreased based on the average helium temperature within the pressure vessel. Due to the large amount of helium and heat losses that occur during the heating process, a significant portion of time is spent adjusting the voltage of the heaters to reach the desired pressure and temperature at a steady state. Figure 4.8 shows the variable transformer used for the depressurization experiments.

Figure 4.8: VEVOR 220V AC variable transformer with dial for output voltage adjustment.

In addition to the RPV, a dummy vessel was added to the system's design to mimic the PCV. In contrast to the pressure vessel mentioned above, this vessel is not an ASME stamped vessel. For purposes of this study, the dummy vessel is not pressured. Its primary function is to mimic the PCV to account for the volume occupied by it. Additionally, its presence allows recreating to a certain degree the flow path that the gases may have to take around the vessel during an accident scenario. This schedule 40 dummy vessel is made of SS-316 with an outer diameter of 16 inches and a height of 69.38 inches.

The two vessels, as mentioned earlier, are enclosed by a containment structure. This structure consists of two rectangular structures made of carbon steel. The containment building of the pressure vessel has a total height of 50 inches with side lengths of 20.5 inches. This section of the containment building has seven window ports, as illustrated in Figure 4.9. The containment building of the PCV has a rectangular prism shape made of carbon steel with a 20.5-inch side length and a total height of 73.875 inches.

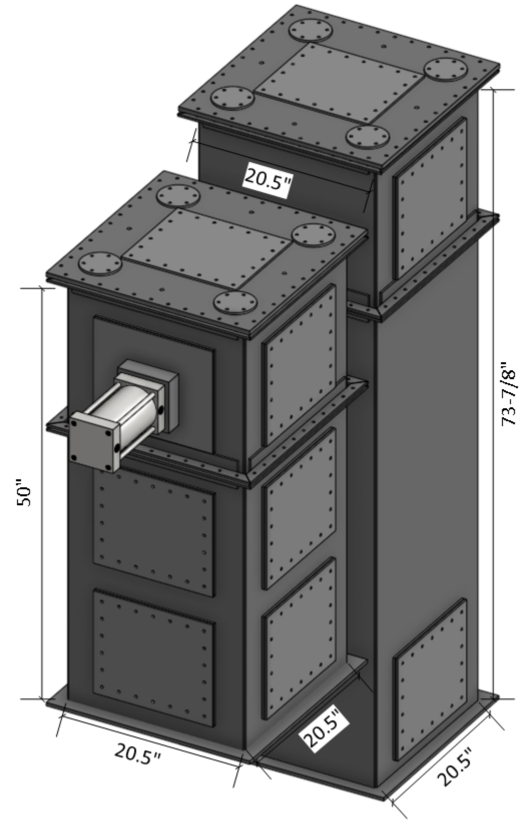

Figure 4.9: Schematic of the containment building of the UI-IF scaled-down HTGR.

The cavity of the containment building is vented using a square duct as shown in Figure 4.10. This ventilation system consists of a 10 by 4 inches square duct with a total length of 4 inches. It was welded to the lower half of a carbon steel plate to allow its easy installation in one of the window ports of the containment building. To mimic the closure of the ventilation system, a hinged gate was added to the design that remains open during the ventilation process. It is closed upon completing the ventilation process to prevent air ingress from the environment.

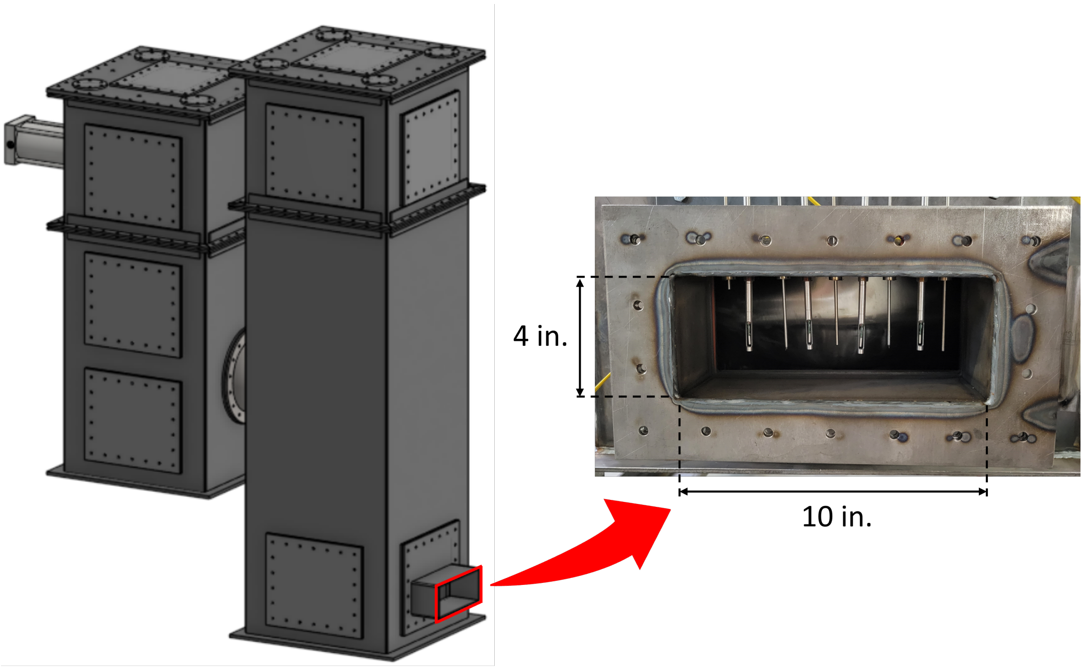

Figure 4.10: Square duct ventilation system of the UI-IF scaled-down HTGR.

Table 4.2 provides a summary of the key parameters of the UI-IF $1/20^{th}$ scaled-down HTGR. Some of these parameters include the height, diameter, and volume of the RPV along with key geometric characteristics of the PCV such as the vessel diameter and height. The same key geometric characteristics of the GT-MHR prototype are included for comparison purposes.

Table 4.2: Comparison of the GT-MHR prototype and the UI-IF $1/20^{th}$ scaled-down HTGR model.

Parameters	**Prototype (GT-MHR)**	**Model ($1/20^{th}$)**
RPV height, m (in.)	23.70 (933.1)	1.207 (47.50)
RPV inner diameter, m (in.)	7.226 (284.5)	0.3969 (15.63)
RPV outer diameter, m (in.)	7.658 (301.5)	0.4064 (16.00)
PCV height, m (in.)	35.22 (1387)	1.762 (69.38)
PCV inner diameter, m (in.)	7.468 (294.0)	0.3937 (15.50)
PCV outer diameter, m (in.)	8.509 (335.0)	0.4064 (16.00)
Cross-vessel inner diameter, m (in.)	2.286 (90.00)	0.2286 (9.000)
Cross-vessel outer diameter, m (in.)	2.438 (96.00)	0.2381 (9.375)
Cross-vessel length, m (in.)	3.048 (120.0)	0.1461 (5.750)

To ensure experimental similarity, the ratio of the model over the prototype's dimensionless numbers was computed at different temperatures. While the model's pressure vessel was verified up to 3 MPa and 810.9 K, instrumentation used in the facility can operate up to certain temperatures. Thus, Table 4.3 summarizes the results obtained for different temperatures at a pressure of 150 psi.

Table 4.3: Ratio of dimensionless numbers using air and helium's thermophysical properties.

	100^{o}C	**125^{o}C**	**150^{o}C**	**175^{o}C**	**200^{o}C**
$\mathbf{Pr}_R$	1.0110	1.0100	1.0100	1.0090	1.0090
$\mathbf{Re}_R$	1.0000	1.0000	1.0000	1.0000	1.0000
$\mathbf{Fr}_R$	0.2235	0.2307	0.2376	0.2444	0.2510
$\mathbf{Sc}_R$	0.9559	0.9585	0.9608	0.9628	0.9647
$\mathbf{Gr}_R$	$1.2627x10^{-3}$	$1.0195x10^{-3}$	$8.3361x10^{-4}$	$6.8930x10^{-4}$	$5.7573x10^{-4}$
$\mathbf{Ra}_R$	$1.2765x10^{-3}$	$1.0300x10^{-3}$	$8.4167x10^{-4}$	$6.9557x10^{-4}$	$5.8065x10^{-4}$
$\mathbf{Ri}_R$	6.1218	5.5972	5.1441	4.7496	4.4036

It is important to note that the surface and bulk fluid temperatures used for these calculations were obtained from past experiments. Some of these temperatures were interpolated based on experimental measurements. As it can be seen in Table 4.3, the Prandtl, Reynolds, and Schmidt numbers are close to unity, which indicates that some of the phenomenologies are preserved very well. The Grashof and Rayleigh numbers of the model and prototype are noticeable different because characteristic length and temperatures differ significantly from each other. The Rayleigh number for the prototype is in the order of 10^{10} while the Rayleigh number for the scaled-down model for the temperatures and pressures considered is about 10^7. A Rayleigh number of magnitude equal to or greater than 10^9 determines if the buoyancy-driven flow is turbulent. A value lower indicates that the flow regime is laminar. In this case, the phenomenology could not be preserved as the Rayleigh number of the model is well within the laminar flow regime, while the prototype is in the turbulent regime.

4.3 INSTRUMENTATION

An experiment uses the $1/20^{th}$ scaled-down facility to measure four parameters. These parameters include the pressure in the vessel, oxygen concentration within the cavity of the VLPC building, temperature, and velocity of the helium-air gas mixture in the cavity section and ventilation duct.

For temperature measurement purposes, multiple thermocouples were mounted in the experimental facility. The helium gas temperature in the pressure vessel is measured using three T-type thermocouples with a 6 inch probe length and limits of error of 0.5^{o}C or 0.4%, whichever is greater. These thermocouples were installed on three of the six lateral outlets of the pressure vessel; refer to Figure 4.11. The thermocouples are mounted in an axial configuration at the three different heights of the pressure vessel. This means that the thermocouples are always at a 90 degree distance from the tested outlet. During an experiment, one of the six lateral outlets of the pressure vessel remains uncapped, three are used for thermocouple placement, and the remaining two are capped using a plug.

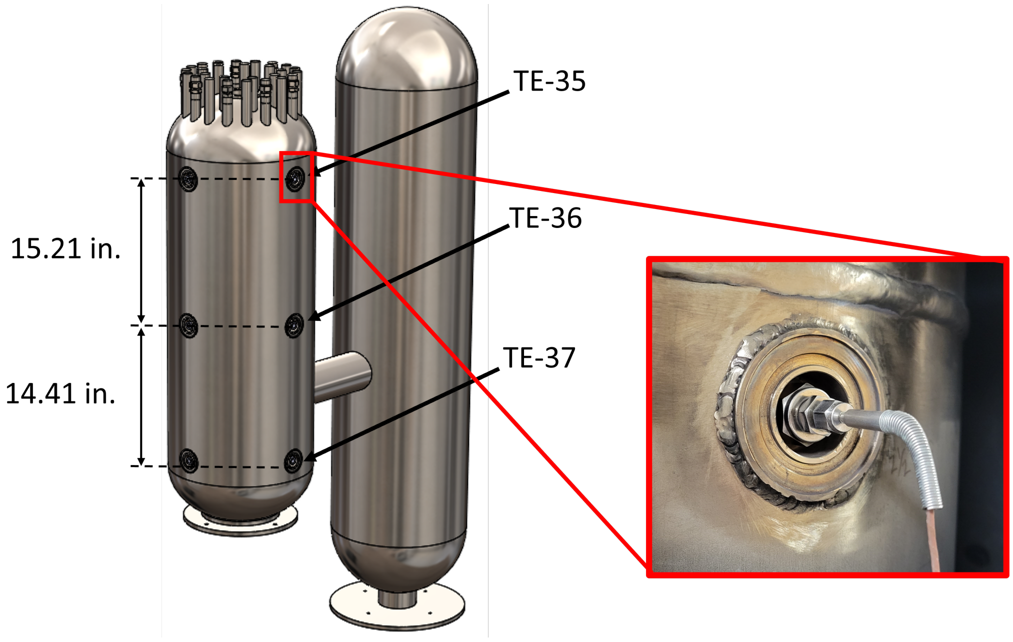

Figure 4.11: Position of pressure vessel T-type thermocouples.

The temperature measurement of the gases within the cavity section is measured using high-temperature low drift K-type thermocouple probes with an exposed junction. These are suitable for air temperature measurements up to 1150°C. The RB is one of the most heavily instrumented sections of the scaled-down experimental facility. The front side of the RPV containment building section has six thermocouples, as shown in the left-hand side of Figure 4.12. These K-type thermocouples were positioned at three different heights, from which three are in the left side corner while the other three are in the right side corner. The back side of the RPV containment building has twelve thermocouples, eight placed near the corners and four in the middle of the containment building wall, as shown in the right-hand side of Figure 4.12. At the top of the same, three thermocouples were mounted for temperature measurement. Similarly, the containment building of the PCV has one thermocouple at the top of the cavity section. Its position is indicated in Figure 4.13.

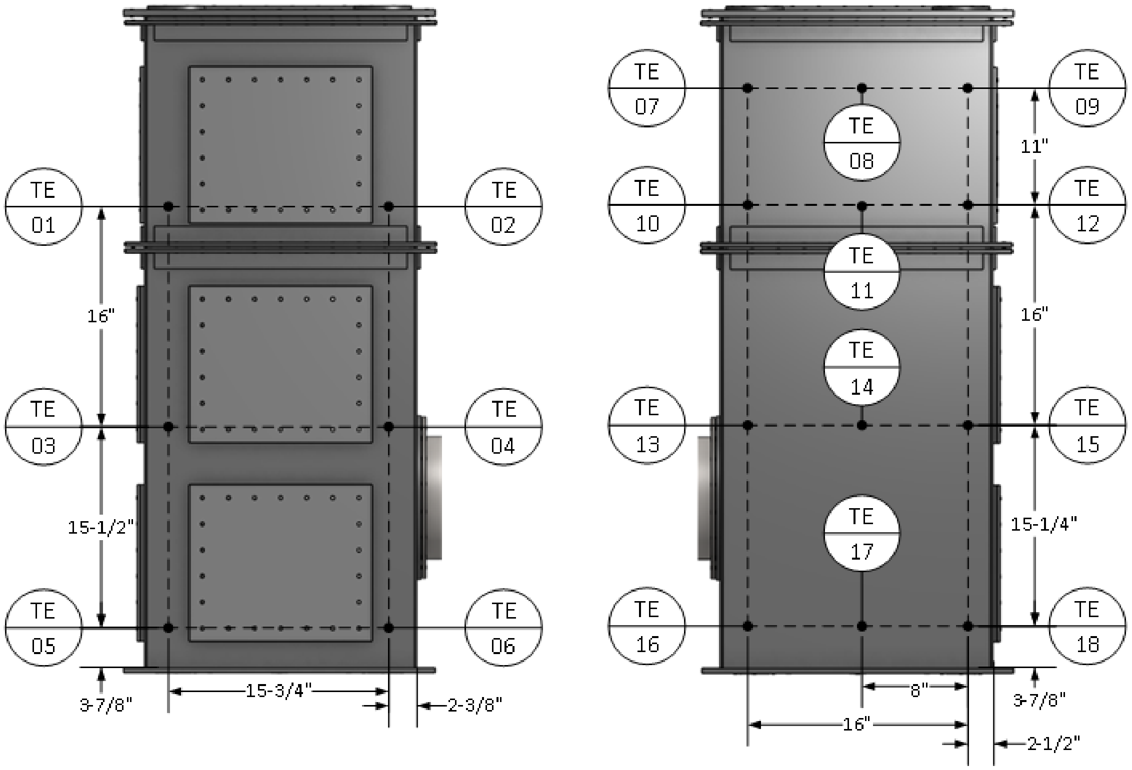

Figure 4.12: Front (left) and back (right) view of the RPV containment building indicating the position of the thermocouples.

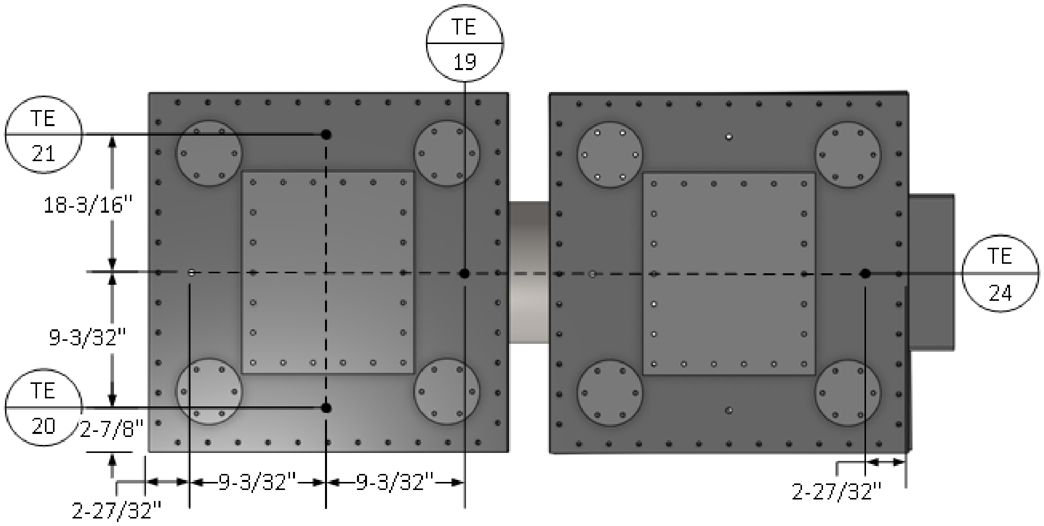

Figure 4.13: Top view of the RPV (left) and PCV (right) scaled-down containment building indicating the position of the thermocouples.

The cavity section of the PCV has two thermocouples on the frontal side. In addition, the axial cross-vessel has two thermocouples installed, one at the upper section of the duct and the other at the bottom. Their placement is shown in Figure 4.14.

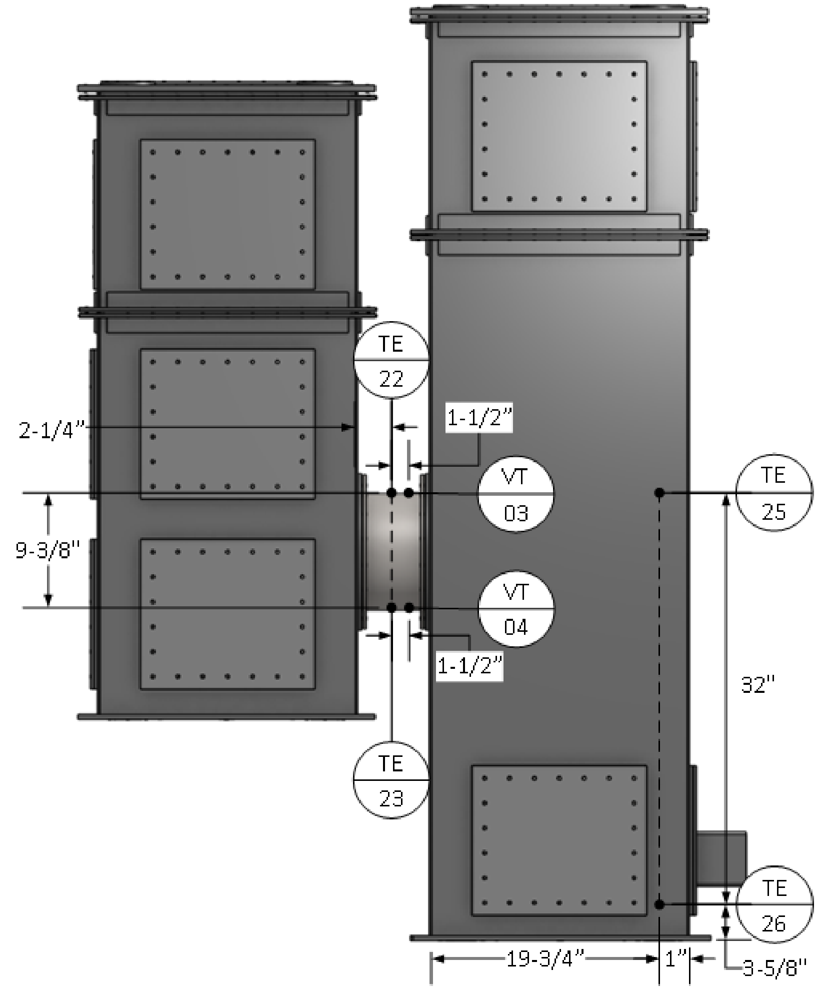

Figure 4.14: Frontal view of the scaled-down containment building indicating some of the thermocouples and velocity sensors placement.

For oxygen measurement, ten zirconium dioxide oxygen sensors from SST Sensing LTD were installed on the walls of the containment building of the experimental facility. While this study uses the concept of O_2 concentration quite frequently, these sensors do not necessarily measure oxygen concentration. Instead, they measure the partial pressure of oxygen in a gas mixture. These zirconium dioxide sensors count with a measurement cell suspended in the middle of a heater coil. When stabilized zirconium dioxide is at high temperatures, its behavior is similar to an electrolyte. A Nernst voltage is generated across the piece of zirconium dioxide when two different

O_2 pressures exist on either side of the same. The voltage generated is proportional to the natural logarithm of the ion concentration of one over the other (SST Sensing Ltd, 2018). A schematic of this sensor type is depicted in Figure 4.15.

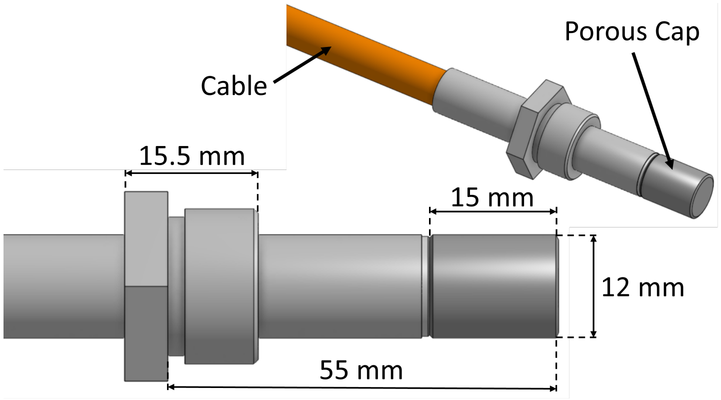

FIGURE 4.15: Schematic of zirconium dioxide oxygen sensor.

These sensors have an oxygen measurement range from 0.1 to 25% with an accuracy of 0.5% following their calibration. These have a fast response time of 4 seconds with a standard response time of 5 seconds (SST Sensing Ltd., 2017). Eight of the ten oxygen sensors were installed on the walls of the RB at different heights, as shown in the left side of Figure 4.16. The remaining oxygen sensors were mounted on the walls of the PCV containment building, as illustrated in the right side of Figure 4.16. Their placement was based on preliminary CFD simulations. CFD models indicated that the corners of the containment building are low-flow areas, making these sections suitable for placing oxygen sensors. These sensors can potentially drift if exposed to high flow velocities.

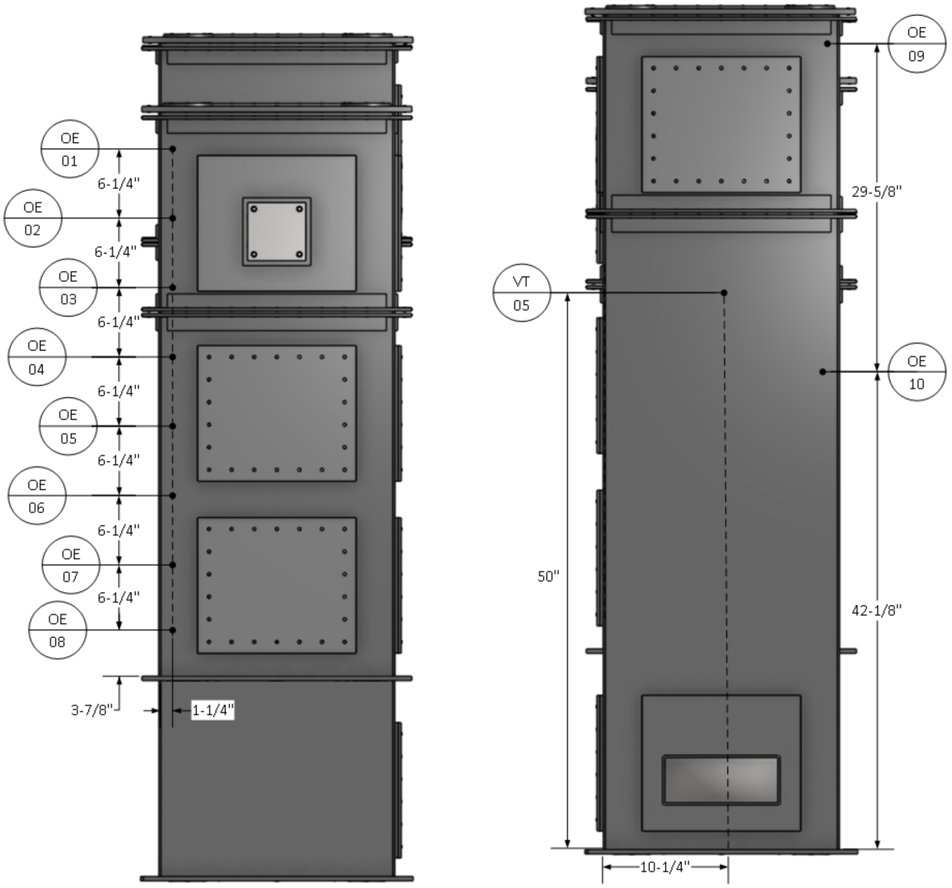

(A) Lateral view of the RB indicating the position of the O_2 sensors.

(B) Lateral view of the containment building of the PCV indicating the position of two O_2 sensors and one velocity sensor.

FIGURE 4.16: Zirconium dioxide oxygen sensors installed on the walls of the scaled-down VLPC.

The velocity of the gas mixture is measured in three sections: the cavity section of the RB, the axial cross-vessel, and the ventilation duct. The velocity is measured using an Omega FMA905A velocity transmitter that can measure velocities up to 10 000 FPM ($50.8\,\mathrm{m\,s^{-1}}$). The probes of the sensors are 12 and 3.25 inches long with an outer diameter of 0.25 inches. Although the probe is made of stainless steel, it can only be exposed to temperatures no greater than 93^{o}C (Omega Engineering, Inc., 2018). Multiple ports were made available to install multiple velocity sensors in the RB walls to measure the velocity of the gases due to natural circulation; however, some of these sensors drift due to their exposure to high temperatures. Thus, it was deemed to limit the number of velocity sensors in the cavity section of the RB. Two velocity sensors were installed on the RB where temperatures are expected to be sufficiently low to prevent them from drifting. They were installed at different heights but aligned vertically; refer to Figure 4.17.

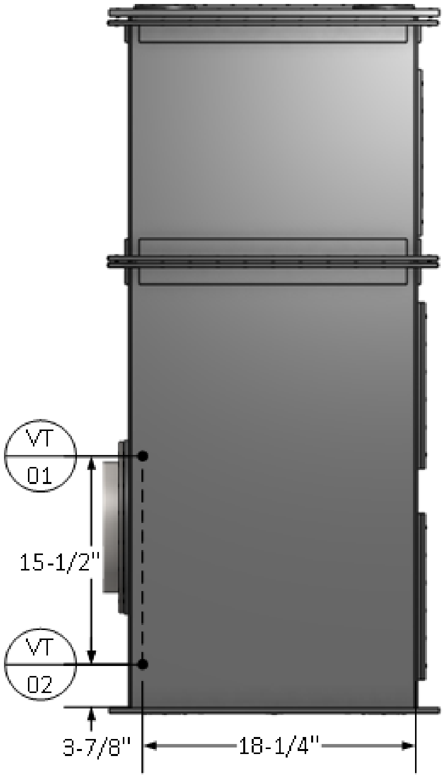

Figure 4.17: Placement of velocity sensors on the RB wall (back view).

On the axial cross-vessel, one velocity sensor was placed at the top of the duct and one at the bottom. The placement of these velocity sensors on the axial cross-vessel was based on preliminary CFD models that indicated that under natural circulation, the hot gases flow from the cavity section of the RB to the cavity of the PCV containment building. The cold gases flow through the lower section of the axial cross-vessel. In an attempt to measure their velocities and temperatures, two velocity sensors and two thermocouples were installed on the axial cross-vessel duct as illustrated in Figures 4.14 and 4.18. On the containment building of the PCV, one velocity sensor was placed on the lateral wall of the containment building as illustrated in Figure 4.16. Four-velocity sensors were installed on the ventilation duct to measure the velocity of the gases venting out through the ventilation system, as shown in Figure 4.19. These sensors, VT-06, VT-07, VT-08, and VT-09, are placed at 2 inches apart from one another. Their main objective is to provide information about the velocity of the gases vent out. It is important to note that their measuring tip is positioned at an equal distance from the upper and lower parts of the ventilation duct.

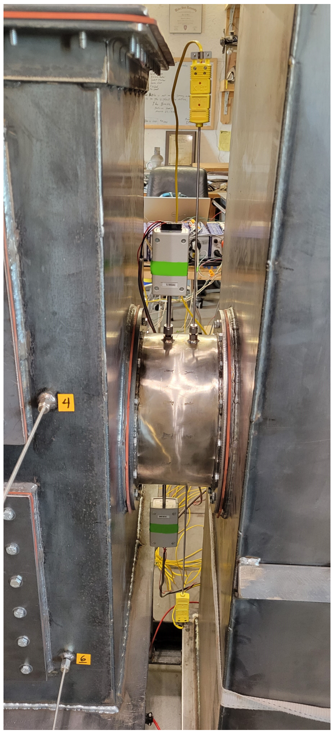

FIGURE 4.18: Placement of thermocouples and velocity sensors on the upper and lower section of the axial cross-vessel duct.

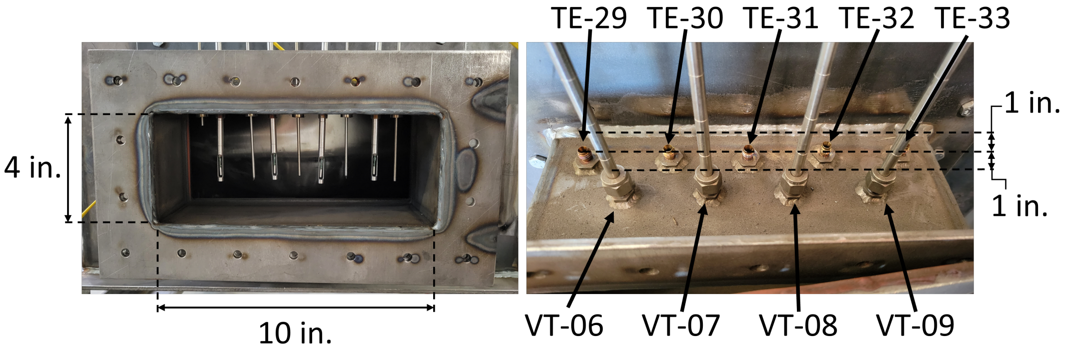

FIGURE 4.19: Front view (left) of the ventilation duct showing the thermocouples and velocity sensors probes protruding from the top. Label and position of thermocouples and velocity sensors (right) installed on the ventilation duct.

The pressure in the vessel is measured using an Omega PX32B1-300GV high-temperature, hermetically sealed pressure transducer capable of measuring pressures from 0 to 300 psig. The pressure transducer, PT-01, can operate within a -40 to 168^{o}C (-40 to 335^{o}F) temperature range, and it has an accuracy of $\pm 0.25\%$. Figure 4.6 displays where the pressure transducer is connected.

4.3.1 *Instrumentation Calibration*

To ensure accuracy, standardization, and repeatability of the experimental measurements, it is paramount to calibrate sensors to prevent inaccurate measurements that can detriment the safety, quality, and equipment longevity.

A total of 37 thermocouples are used for temperature measurements. These sensors were calibrated using two temperature calibrators. Thermocouples are inserted into the Fluke 9171 thermocouple furnace, shown on the right-hand-side of Figure 4.20, to calibrate them to a temperature range of -30 to 155^{o}C. Fluke 9173 can calibrate the thermocouples at higher temperatures since its temperature range is from 50 to 700^{o}C.

FIGURE 4.20: Fluke 9173 (left) and 9171 (right) thermocouple furnaces.

The furnaces shown in 4.20 can maintain stable temperatures. Fluke 9171 can provide stable temperatures of ±0.005^{o}C over its full range, and Fluke 9173 can achieve stability of ±0.03^{o}C over its full range. To minimize axial gradient and loading effects, it is recommended to insert the thermocouples into the bottom of the well. The well of both thermocouple furnaces has a depth of 203 mm. At the bottom of the same has a 60 mm. homogeneous zone, where the vertical gradient in this zone ranges from ±0.02^{o}C at 0^{o}C to ±0.4^{o}C at 700^{o}C. For this reason, the K-type thermocouples were purchased to have a probe length of 12 inches so they can reach the bottom of the furnace well. The T-type and surface temperature sensors have a shorter probe length because these sensors were light sensors found in one of the UI-IF laboratories.

For calibration of the thermocouples, five of them are inserted into the Fluke 9171 furnace until the tip of the probe reaches the bottom of the well. The furnace is then turned on, and the temperature is adjusted. The first calibration point is -25^oC. When the temperature of the furnace is stable, the temperature measurements of the thermocouples and furnace are recorded using LabVIEW 2021 (32-bit). The data acquisition cards NI-9213 are used to deliver the measurements to the computer, from which these measurements are recorded with a sampling rate of 5 Hz and a sampling size of 5. The average measured temperature is plotted against the reference temperature provided by the furnace, refer to Figure 4.21, at which a linear correlation is expected. A polynomial fit is generated for each thermocouple based on the measured and reference temperatures. This calibration curve is incorporated into LabVIEW to collect calibrated temperature values. This procedure is repeated for multiple reference temperatures.

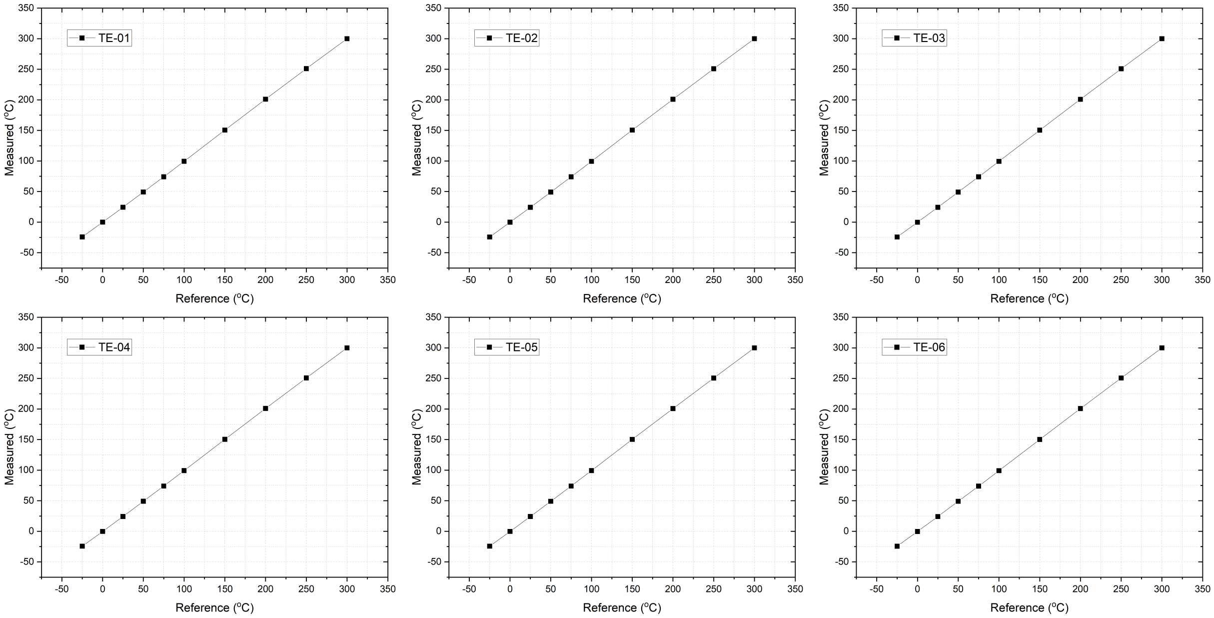

Figure 4.21: Calibration plots of thermocouples TE-01 through TE-06.

The velocity sensors were calibrated using a Testo 405*i* anemometer wireless smart probe. This anemometer can measure velocities up to $30\,\mathrm{m\,s^{-1}}$ with an uncertainty of $\pm 0.7\,\mathrm{m\,s^{-1}}$. As indicated in Figure 4.22, a pipe was connected to the laboratory air supply. Downstream from the air source, a tee was incorporated into the pipe to allow the insertion of the velocity sensor probe to be calibrated. Further downstream, another tee was added to insert the Testo anemometer probe. The available air supply from the laboratory could only provide consistent velocities up to about $9\,\mathrm{m\,s^{-1}}$.

Consequently, it was deemed to calibrate the velocity sensors only up to about $9\,\mathrm{m\,s^{-1}}$. A linear correlation is developed and extrapolated from the calibration points to account for higher velocities. To adjust the air velocity in the manifold, a tee was connected near the air source inlet from which a ball valve was installed. The ball valve is opened either fully or partially to reduce the air velocity. To further reduce the velocity, a valve was connected near the outlet of this manifold. This valve is closed partially to achieve even lower velocities.

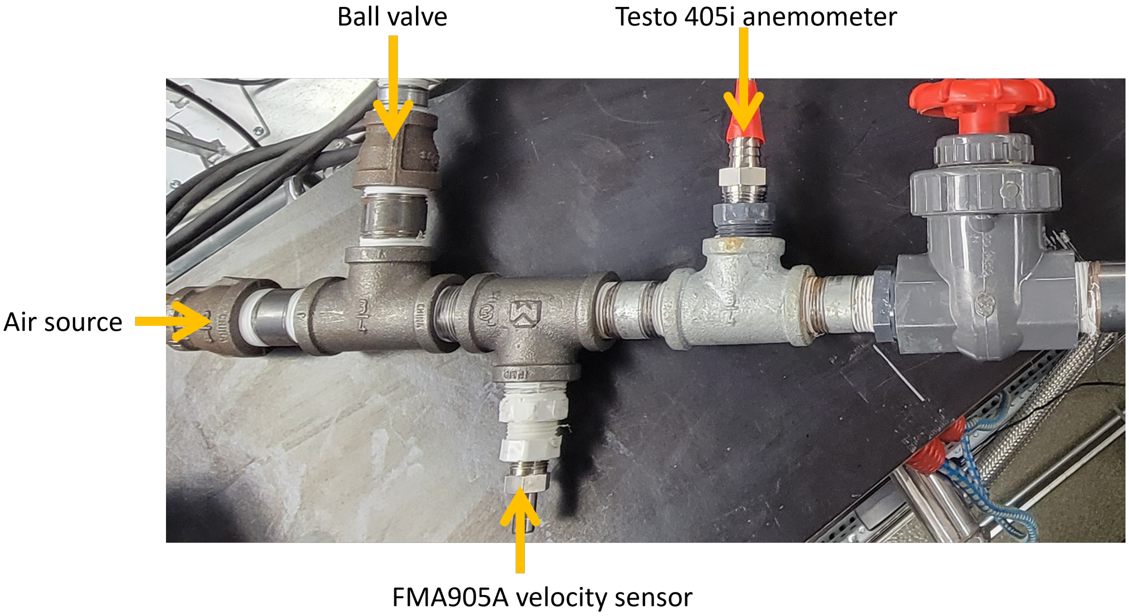

Figure 4.22: Manifold used for calibration of velocity sensors.

The calibration procedure consisted of mounting the velocity sensor to calibrate in the port illustrated in Figure 4.22. Similarly, the Testo anemometer was turned on and mounted in its respective port. The sensors were fully inserted into the manifold to ensure the exposure of the probe tip to the air channel. It also ensured the air flow was perpendicular to the sensor window. Once the sensors are correctly installed, the velocity sensor to be calibrated is powered up by a power supply and connected to a NI-9203 current input module used to deliver the measurements to the computer. Prior to the initialization of the calibration procedure, the manifold is connected to the air supply using a plastic hose. The calibration is initiated by partially opening the air supply. At this point, the ball valve is fully opened. The air velocity is measured using the Testo anemometer, and the current signal of the sensor to be calibrated is recorded using LabVIEW. The air velocity is increased by adjusting the air supply and the two valves in the manifold. The data obtained from the sensor calibration is then processed to obtain a linear correlation of the current signal output of the sensor and the air velocity. Figure 4.23 shows the measured values and the curve fitting developed from the same data for velocity sensor VT-01.

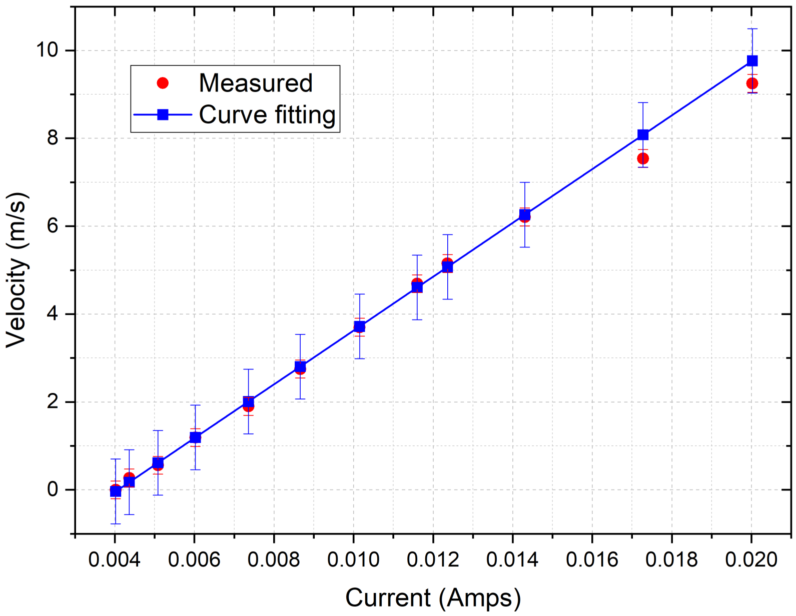

Figure 4.23: Calibration data of velocity sensor VT-01 plotted along the curve fitting developed for this sensor.

The calibration of the oxygen sensors did not require a reference gas. The sensors were calibrated per manufacturer specifications. The oxygen sensors have a measuring rate from 0.1 to 25%, whose accuracy is 0.5% post calibration. The sensor does not directly measure the oxygen concentration. Instead, the sensor measures the partial pressure of oxygen. This means that the sensor requires a reference value, and the recommended gas (and used for calibration of these sensors) is fresh air. Fresh air is known to have an O_2 concentration of 20.7%. Thus, the calibration procedure is as follows: the sensor is connected to a power supply and the NI-9203 current input module. Once the sensor is powered up, it is allowed to stabilize for 10 min. At this point, the sensor is exposed to fresh air. Following the 10 min waiting period, the sensors should output a relatively constant value. The calibration is executed by short-circuiting the calibration input of the board to the 0 V of the power supply for a minimum of one second. Thereafter, the sensor's output signal should be about 17.25mA, equivalent to a 20.7% O_2 concentration. Table 4.4 provides a summary of the analog output signal values with their respective oxygen concentration.

The high temperature, hermetically sealed pressure transducer was calibrated using an air compressor. This air compressor was connected to a small manifold

Table 4.4: Analogue Output Values of Oxygen Sensors.

O_2%	4 – 20 **mA output**
0.1%	4.06 mA
5%	7.2 mA
20.7%	17.25 mA
25%	20 mA

that had multiple pressure gauges that had a resolution of 0.5 psi. The calibration was conducted by pressurizing the manifold at multiple pressures using the air compressor. The calibration started from 0 psig., then the pressure was increased slowly until about 150 psig. Figure 4.24 shows the linear correlation between the current and pressure. From this data, a linear correlation was developed and used in LabVIEW.

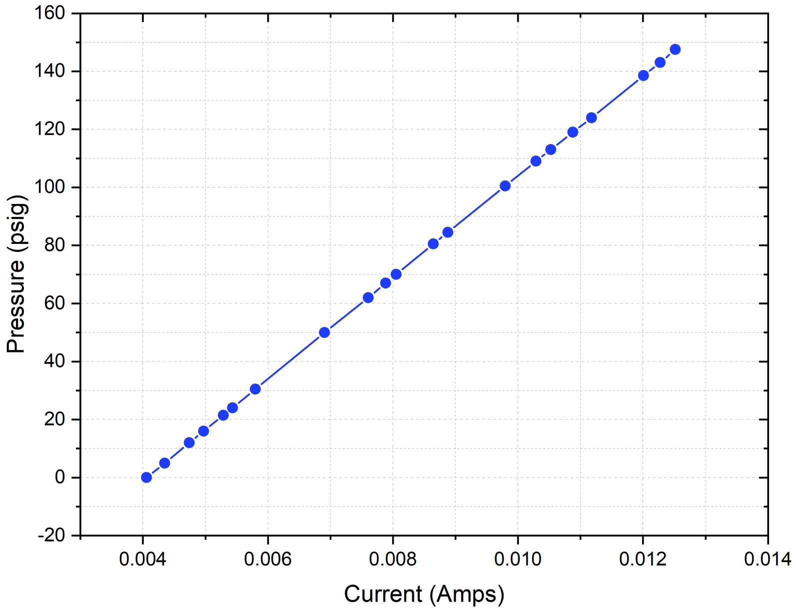

Figure 4.24: Calibration data of pressure transducer PT-01.

CHAPTER 5

EXPERIMENTAL PROCEDURE

Several configurations for the $1/20^{th}$ scaled-down facility were tested to meet the goals outlined in Section 1.3. The chosen setups were based on a sensitivity study that looks into the gas mixture for different break sizes, the break location, the ventilation duct placement, total time of active ventilation, and without heaters on.

The repeatability and reproduction of the efforts are crucial to expanding this study's scope further. Thus, it was deemed to create a chapter dedicated to describing the procedure followed in conducting the experiments and summarizing the test matrix for the sensitivity analysis. The following sections describe how the facility was prepared for the experiments and what parameters were singled out for further testing.

5.1 PROCEDURE TO PREPARE SCALED-DOWN FACILITY TO INITIATE EXPERIMENTATION

For each experiment, the scaled-down facility must be prepared for an experiment. A rigid procedure was followed to ensure repeatability and gather reliable measurements. This procedure is outlined below:

1. Visual inspection of the experimental facility is carried out before each experiment to evaluate the facility's status. During this inspection, an assessment is conducted to determine what needs to be changed to the experimental facility to test the configuration of interest. These changes may involve the placement of a different outlet size, changing the placement of the pneumatic piston, determining if a new helium tank is needed, and identifying sections that need to be fastened.

2. Mount the pneumatic piston to the designated window port if needed. Once the pneumatic piston is secure, connect the air line to the pneumatic piston.

3. The air compressor, refer to Figure 5.1, is turned on until the air line reaches a pressure of at least 100 psi. to enable the pneumatic piston to plug the vessel properly.

Figure 5.1: CRAFTSMAN Portable Electric Air Compressor.

4. Adjust the pneumatic piston to allow it to push and retract the metallic plug at a slow rate, allowing the researcher to properly align the arm of the pneumatic to the vessel outlet.

5. Position high-temperature gasket on the plug and actuate pneumatic piston to plug vessel.

6. Turn on the computer and open the LabView program created for the gas mixing experiments.

7. Turn on the 24V power supply that powers the oxygen, pressure, and velocity sensors. After that, energize them. Allow five minutes for the oxygen sensors to generate stable readings. Oxygen readings should be around 20.7%. Once the oxygen readings are stable, calibrate oxygen sensors as indicated in the User's Guide (SST Sensing Ltd., 2017).

8. Connect the vacuum pump (Figure 5.2) to the vacuum line of the experimental facility.

FIGURE 5.2: Fisherbrand Maxima C Plus Vacuum Pump.

9. Close valves BV-01, BV-02, and BV-03 when using the vacuum pump. Open valve BV-04 (refer to Figure 4.6) to measure vacuum pressure.
10. Turn on the vacuum pump, followed by opening the vacuum line (BV-06). This valve is shut when the vacuum pressure reaches −25 in. Hg.
11. Vent instrumentation and helium lines to avoid any accumulation of air in the pressure vessel.
12. Turn on the vacuum pump, then open the valve (BV-06) again. This valve is closed when the vacuum pressure reaches −25 in. Hg.
13. Ensure the line of the pressure relief valve remains open prior to initializing pre-pressurization.
14. Pre-pressurize vessel slowly with helium by opening the valve (BV-02). Once the pressure gauge indicator reads a pressure higher than 0 psig., the valves BV-01 and BV-03 are opened. After that, shut the valve BV-04.
15. Stop the pre-pressurization process when the desired pressure is reached. The system is inspected for helium leakage by monitoring the vessel pressure. It is recommended that the vessel reach a steady state as the temperature can vary during the pressurization process, influencing pressure measurements.

16. Connect Variac to 208V power line. Turn on Variac by turning the Variac's knob to adjust for the desired voltage. It is recommended to apply a low voltage to the heaters initially. Thereafter, the voltage is increased by 30V steps. Adjust Variac's voltage until the pressure vessel reaches the desired pressure and temperature.
17. Allow the system to stabilize prior to initializing the depressurization process.
18. Check that the ventilation gate is open. Then, adjust the pneumatic piston so it can unplug the vessel at a fast rate.
19. Retract pneumatic piston arm to initialize depressurization process. From the beginning of the depressurization process, the researcher will count down from 50 seconds (or as indicated by the test matrix) using a timer to time the moment the ventilation gate should be shut.
20. Once experimental data is recorded, the Variac is turned off and disconnected from the voltage supply.
21. The data acquisition from LabView is stopped. This action is followed by shutting down the instrumentation powered by the 24V power supply.
22. When the system has cooled down enough, the upper ports of the containment building of the RPV and PCV are unbolted to vent helium from the upper sections of the system. Figure 5.3 shows an example of one of the bolts unfastened to vent the helium trapped in the upper sections of the scaled-down RB.

Figure 5.3: Bolt unfasten from the upper section of the RB of the scaled-down experimental facility.

Each experiment must follow the steps mentioned above to ensure repeatability of the experimental results. The experiments performed in this study are summarized in Section 5.2.

5.2 TEST MATRIX

After the description of the experimental procedure outlined in Section 5.1, a section has been dedicated to describing the initial conditions and setup of the experiments conducted at the UI-IF $1/20^{th}$ scaled-down HTGR. To ensure the varying gas mixture phenomenology conditions during an accident scenario are captured, five different parameters are evaluated: timing of active ventilation, heating of the pressure vessel during the depressurization process, location and size of the break, and location of the ventilation duct.

5.2.1 *Time of active ventilation*

The total time of the ventilation of the cavity section is an influential parameter as flow reversal can occur at the ventilation duct, resulting in fresh air ingress to the cavity section. Additionally, closing the ventilation gate too early can prevent the cavity from further venting more air out of the system. Thus, a series of experiments are conducted where the timing of the active ventilation is varied. In some instances, the ventilation duct gate was never shut, while in other experiments, the gate was shut a few seconds past the beginning of the depressurization.

5.2.2 *Ventilation Location*

Preliminary CFD results have indicated that the ventilation system's location significantly impacts the amount of air vented out of the containment building cavity. The VLPC building can be designed slightly differently. For instance, the ventilation system can be placed in an upper section of the PCV containment building, whereas other designs may consider placing it in a lower section. Thus, to assess the different configurations, the window ports V11 and V12 are used to mount the ventilation system. Comparing both configurations will provide further insight into the ventilation system's performance.

5.2.3 *Break Size*

The break size is one of the most imperative parameters to be tested because the size of the break dictates the time that takes to depressurize the pressure vessel. The rate at which helium migrates towards the cavity section of the VLPC building can influence the amount of air vented out of the system. Thus, evaluating the system's behavior with different break sizes was deemed essential.

5.2.4 *Break Location*

Multiple studies have considered the probability of having a break on the axial cross-vessel duct. However, information from studies considering breaks in other locations is minimal. While the probability of a break on the pressure vessel is very low, the intended purpose of the outlets on the pressure vessel is to study the gas dynamics of the system when the break is at different heights and angles. Therefore, the break sizes B01, B03, B04, and B06 are tested to show the system's behavior when a break occurs at different angles and heights.

To summarize the experiments conducted in this study, a table was generated to indicate the setup used for each experiment (Table 5.1). It is important to point out that the heaters for these experiments were left turned on during and after the depressurization process. Table 5.2 classifies the different experiments based on the focus of the study.

TABLE 5.1: Test matrix of helium-air mixture experiments.

Experiment #	**Test ID**	**Break size (in.)**	**Break location**	**Ventilation location**	**Ventilation time**
1	B01-V11-0.410	0.410	B01	V11	50 sec.
2	B01-V11-0.250	0.250	B01	V11	50 sec.
3	B01-V11-0.188	0.188	B01	V11	50 sec.
4	B01-V11-0.125	0.125	B01	V11	50 sec.
5	B03-V11-0.410	0.410	B03	V11	50 sec.
6	B04-V11-0.410	0.410	B04	V11	50 sec.
7	B06-V11-0.410	0.410	B06	V11	50 sec.
8	B01-V12-0.410	0.410	B01	V12	50 sec.
9	B01-V11-0.410	0.410	B01	V11	Indefinitely
10	B01-V11-0.410	0.410	B01	V11	65 sec.
11	B01-V11-0.410	0.410	B01	V11	22 sec.
12	B01-V11-0.410	0.410	B01	V11	12 sec.

Table 5.2: Classification of experiments based on the focus of study.

Focus of study	Experiment no.	Test ID #	Variable tested
Venting time	1, 9, 10, 11, 12	B01-V11-0.410	12, 22, 50, 65 sec., indefinitely
Break size	1, 2, 3, 4	B01-V11-0.410, B01-V11-0.250, B01-V11-0.188, B01-V11-0.125	0.410 in., 0.250 in., 0.188 in., 0.125 in.
Break location	1, 5, 6, 7	B01-V11-0.410, B03-V11-0.410, B04-V11-0.410, B06-V11-0.410	B01, B03, B04, B06
Ventilation location	1, 8	B01-V11-0.410, B01-V12-0.410	V11, V12

CHAPTER 6

RESULTS

The results covered in this section are divided into five different sections. Section 6.1 compares the results of different experiments with the same initial conditions and configuration for repeatability purposes. Section 6.2 summarizes the experimental results obtained when the ventilation gate is closed at different times. Section 6.3 looks into the experimental results of four experiments with different break sizes. The location of the break size is studied in detail in Section 6.4, and Section 6.5 provides insight into the gas dynamics of the cavity section when the ventilation duct is placed in two different locations. The last section is solely dedicated to analyzing the RPV cavity's oxygen concentration, temperature stratification, and the lock-exchange flow phenomena in the axial cross-vessel duct to determine the flow area of the hot and cold gas mixtures flowing under natural circulation.

The experiments are conducted with similar initial conditions, where the pressure vessel is pressurized and heated in accordance with the procedure outlined in Section 5. Experimental results include oxygen concentration, pressure, temperature, and velocity measurements.

6.1 REPEATABILITY OF EXPERIMENTAL RESULTS

For experimental purposes, it is paramount to ensure the repeatability of the results and quantify the standard deviation (σ) of such experiments. Ideally, the execution of multiple experiments with the same initial conditions and system configuration should yield the same experimental results. However, some factors can contribute to differences between measurements, such as environmental factors (changes in temperature, electronic noise, drafts, and vibrations), lag time and hysteresis, instrumentation resolution, and physical variations. The repeatability and quantification of the standard deviation are demonstrated by testing the configuration B01-V11-0.410 multiple times, where the initial temperature of helium is about 130^oC, and the initial pressure is 140 psig. Experiments 1, 9, and 10 have the same initial conditions and configuration, but the time of active ventilation is different. To prevent duplicate efforts, these experiments were compared against each other for the first 50 seconds following the beginning of the depressurization. During this time scale, the results are expected to be the same since the initial conditions and experimental facility configuration is the same, including leaving the ventilation gate open during this time frame.

Theory indicates that random error for many trials will result in a distribution such as the one displayed in Figure 6.1. The peak represents the average result ($\bar{x}$).

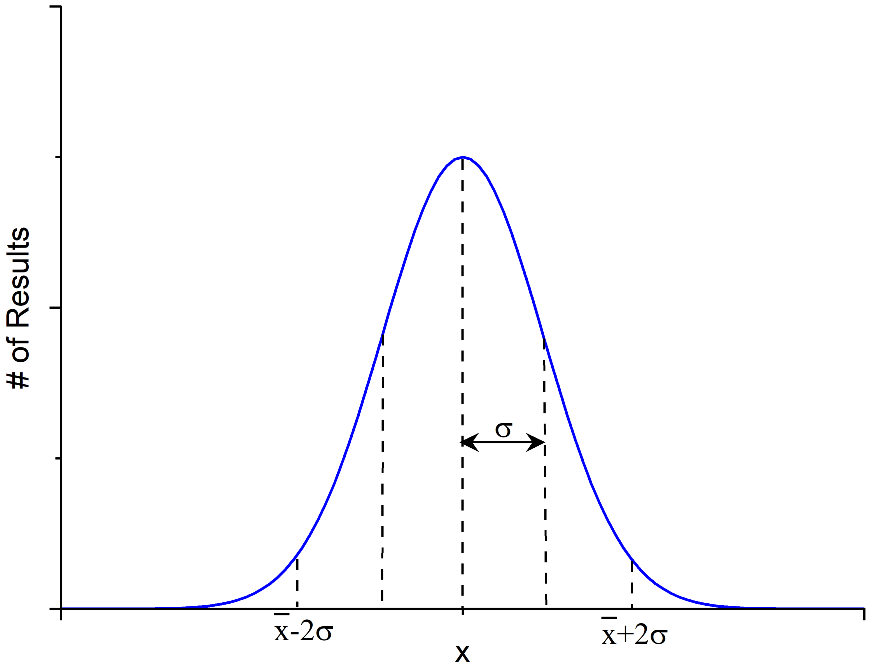

Figure 6.1: Random error distribution.

The standard deviation is calculated using Equation 6.1. 68.3% of all results fall between $\bar{x} - \sigma$ and $\bar{x} + \sigma$, and 95.5% fall between $\bar{x} - 2\sigma$ and $\bar{x} + 2\sigma$. The standard deviations presented in this section use a standard deviation of σ.

$$\sigma = \sqrt{\frac{1}{N-1} \sum_{i=1}^{N} (x(i) - \bar{x})^2} \tag{6.1}$$

The depressurization of the RPV for experiments 1, 9, and 10 is compared against each other and shown on the left-hand side of Figure 6.2. The difference between these experiments is minimal when plotted together. The average pressure and the standard deviation are calculated and shown on the right-hand side of Figure 6.2. The average standard deviation for the pressure evolution within the first fifteen seconds following the beginning of the depressurization is $\sigma_{ave} = 0.5541$, where the minimum recorded value is $\sigma_{min} = 0.0151$ and the maximum is $\sigma_{max} = 4.2005$.

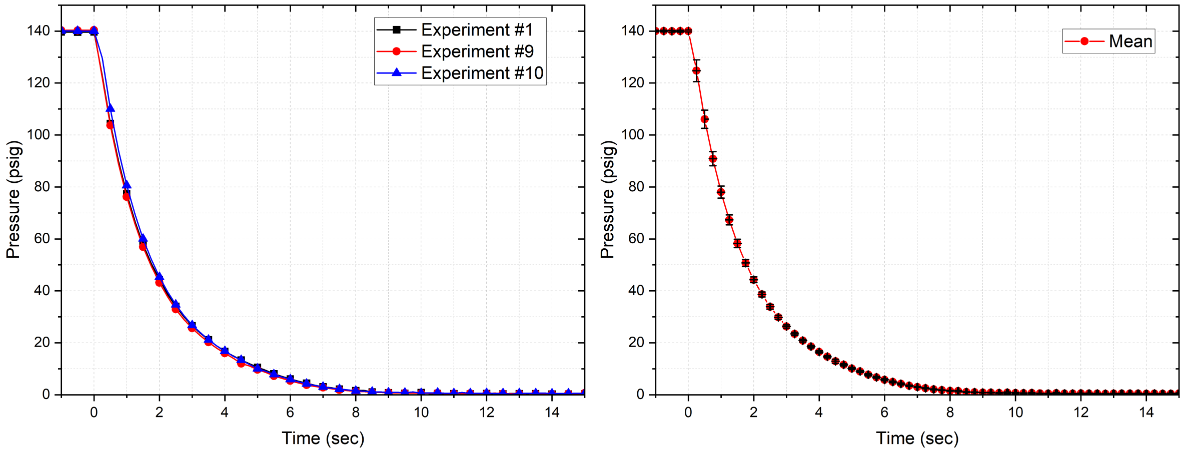

FIGURE 6.2: Pressure evolution within the vessel for three different experiments (left), and the average pressure with its respective standard deviation (right).

As indicated in Section 4, multiple thermocouples are used for temperature measurements of the cavity section. Comparing all thermocouples used in the experiment could result in an extensive analysis. Thus, the thermocouples on the frontal view of the RB of the scaled-down facility are only analyzed in this section. As shown in Figure 6.3, the temperature evolution of the cavity section for the three experiments followed a similar trend, with minor variations.

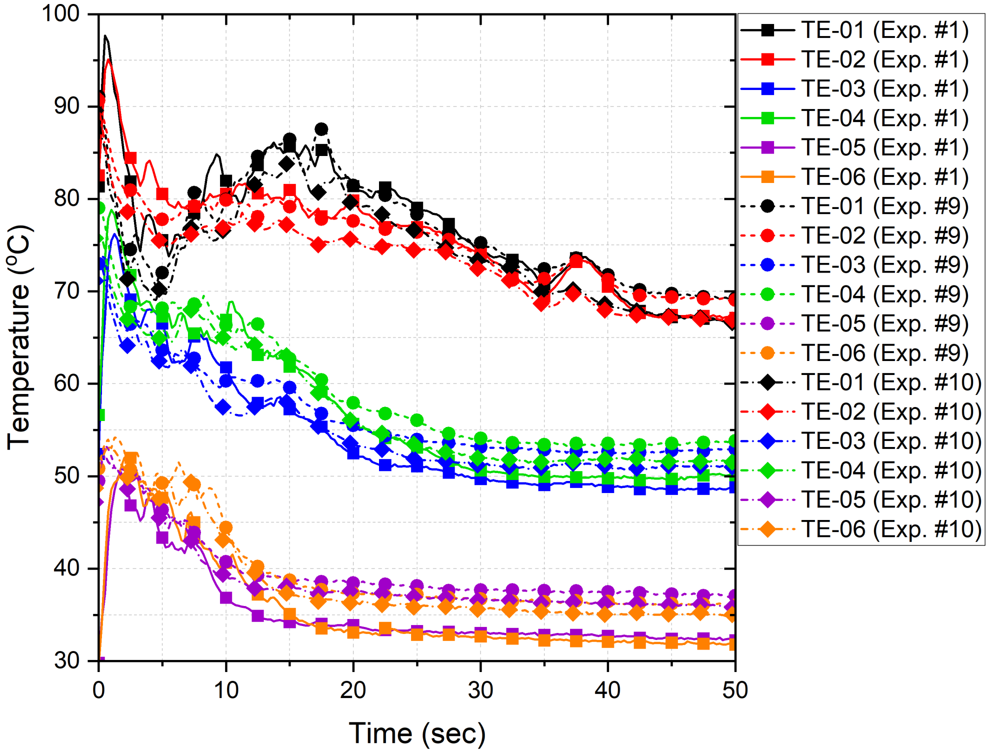

FIGURE 6.3: Temperature evolution within the frontal section of the RB.

Generally, the thermocouples measured very similar results with minimal variations. The temperature measurements from the thermocouple TE-01 vary more than the others in the first 5 seconds. A possible explanation for this behavior is that this thermocouple is the closest to the outlet of the vessel. The temperatures at which the thermocouples TE-01 and TE-02 have been exposed are higher than the other thermocouples. While the experiments are conducted with almost identical initial conditions, the turbulence generated by the helium jet outlet will not always be the same. These variations caused by the turbulence can result in a more significant discrepancy in the temperature measurements as there is a probability of cold air mixing with the hot gases in the upper sections.

Another factor that may influence these temperature variations is the initial temperature of the helium. While the pressure vessel is heated using the same approach, there are minor variations in the temperature stratification. These temperature variations were computed to be no greater than 5%, which can explain these temperature variations.

The average temperature for each sensor was calculated along with the standard deviation. Figure 6.4 shows the average temperature along with the standard deviation for each thermocouple, and Table 6.1 reports the same minimum, maximum, and average standard deviation.

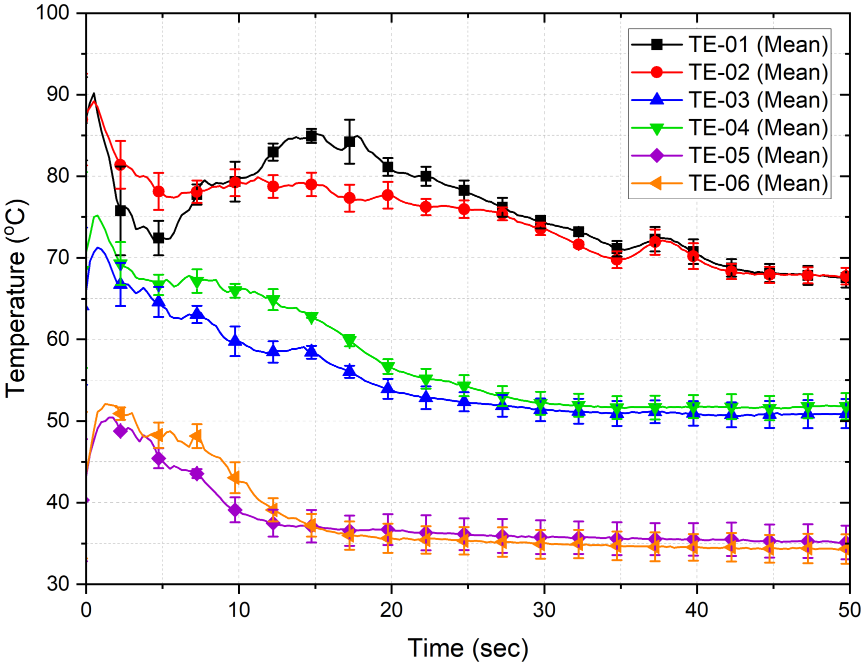

Figure 6.4: Average temperature of thermocouples TE-01 through TE-06 for experiments 1, 9, and 10.

Table 6.1: Standard deviation of temperature measurements of the scaled-down RPV cavity section.

Thermocouple	SD_{min}	SD_{max}	SD_{ave}
TE-01	0.0224	6.6794	1.5048
TE-02	0.3425	5.2682	1.3565
TE-03	0.1196	9.5682	1.5149
TE-04	0.1812	9.9963	1.3736
TE-05	0.1265	9.4848	1.9455
TE-06	0.2213	9.9941	1.7808

Based on the information presented in Table 6.1, the average standard deviation of the thermocouples is no greater than 2. Similarly, the temperature measured by the thermocouples at the ventilation duct were compared against each other and displayed in Figure 6.5.

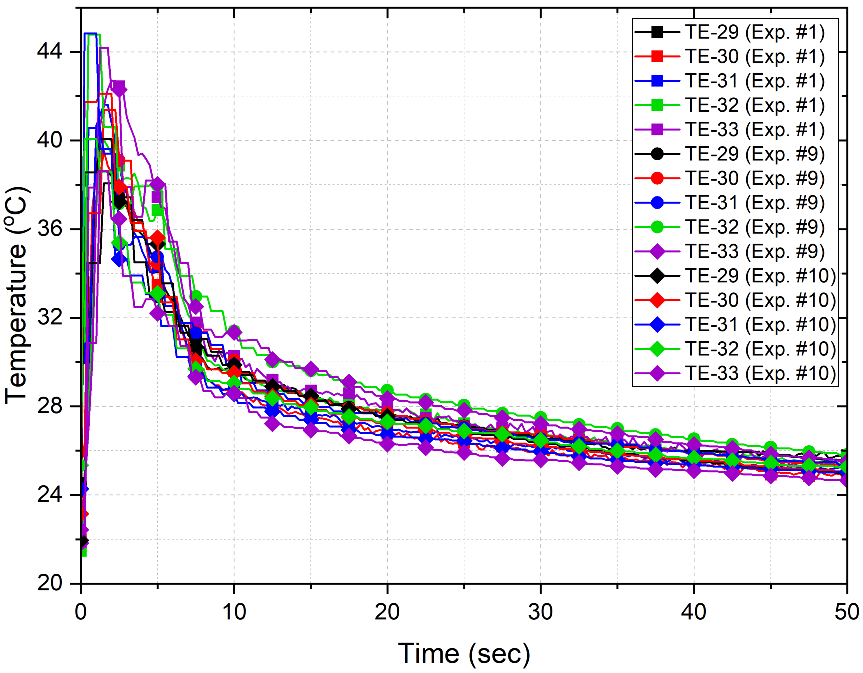

FIGURE 6.5: Temperature evolution within the ventilation duct for experiments 1, 9, and 10.

The thermocouples follow similar trends with some minor variations. The average temperature was calculated and plotted along with the standard deviation to account for these variations, as seen in Figure 6.6. The most significant temperature variations are near the peak temperature. Table 6.2 provides a summary of the calculated standard deviations of these thermocouples. This table indicates that the most significant standard deviation is no greater than 1, which is better than the standard deviation reported for the thermocouples mounted in the RPV containment building.

TABLE 6.2: Standard deviation of temperature measurements of the ventilation duct.

Thermocouple	**SD**$_{min}$	**SD**$_{max}$	**SD**$_{ave}$
TE-29	0.0131	6.6852	0.2943
TE-30	0.1142	7.7341	0.4501
TE-31	0.1313	8.5935	0.5082
TE-32	0.2254	7.1459	0.7896
TE-33	0.2763	4.5092	1.0120

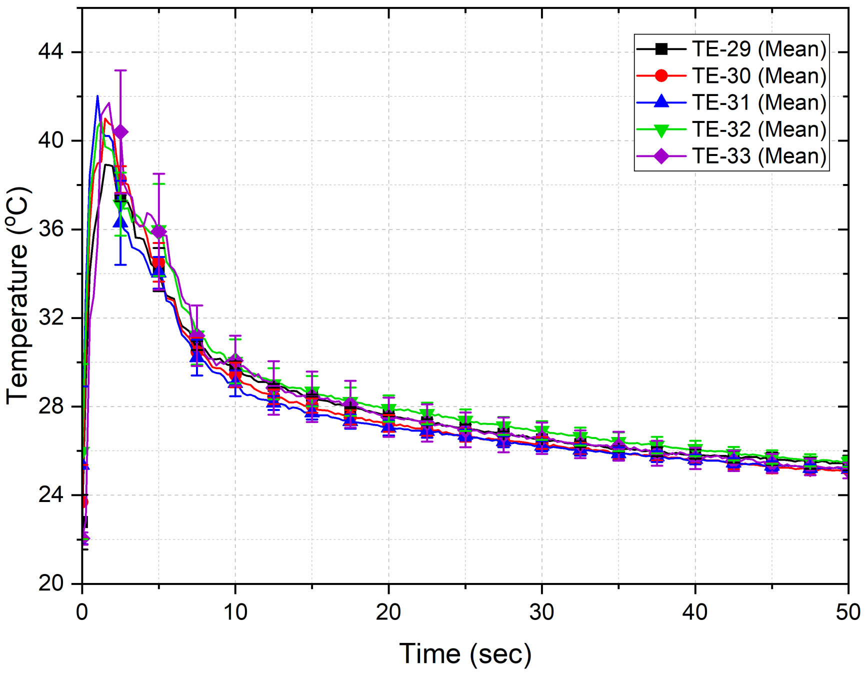

FIGURE 6.6: Mean temperature evolution within the ventilation duct for three experiments.

Oxygen measurements play a vital role in this study as they evaluate the system's performance to vent air. Thus, it is paramount to reproduce the results experimentally with little to no variations. The oxygen measurements for the three experiments are plotted and compared against each other in Figure 6.7. Additionally, the average O_2 measurements are showcased in Figure 6.8.

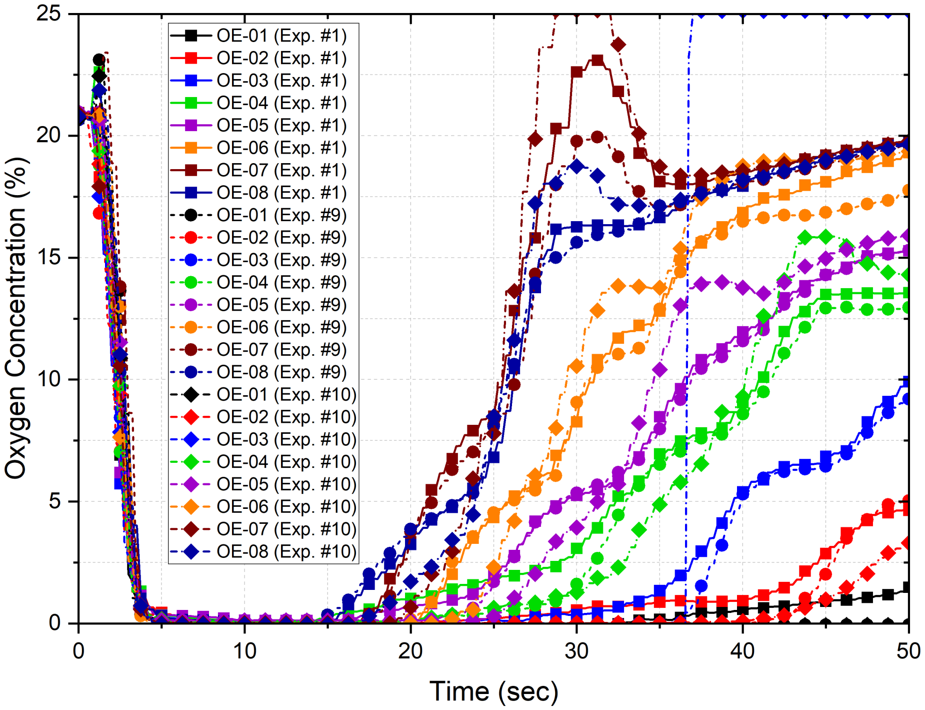

FIGURE 6.7: O_2 measurements of the RB cavity for experiments 1, 9, and 10.

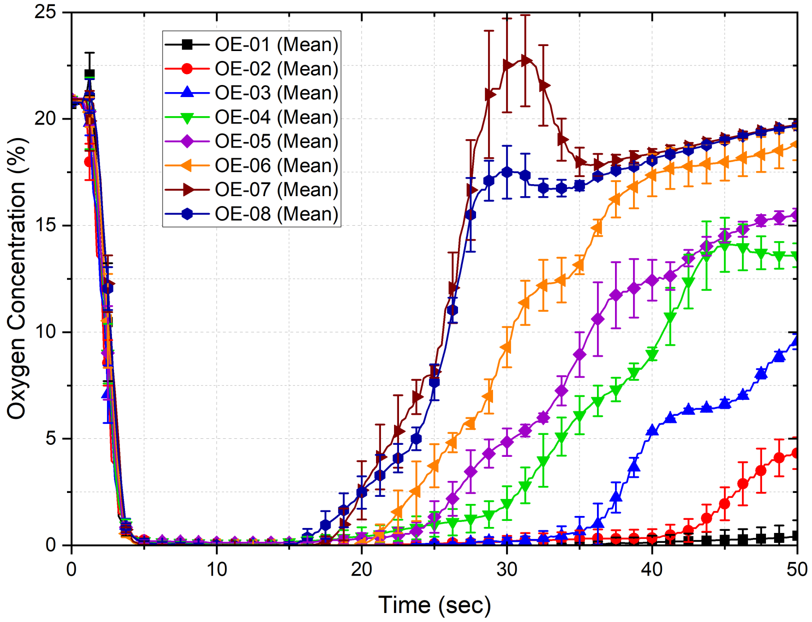

FIGURE 6.8: Average O_2 measurements and their respective standard deviation of the RB cavity for experiments 1, 9, and 10.

The oxygen concentration for the first twenty seconds is quite similar from experiment to experiment as the O_2 levels drop to about 0% at the same time and rate. Minor discrepancies were noted after twenty seconds following the depressurization process. These slight differences can be attributed to the turbulence caused by the helium jet. Once the depressurization is complete, the system is trying to reach equilibrium as buoyancy forces predominate the gas dynamics of the system. Additionally, in this time frame, the motion of the gases slowly switches from being predominantly driven by forced convection to natural convection. During this transition, the gases are expected to exhibit turbulent behavior, which can justify the difference in O_2 measurements. Table 6.3 summarizes the standard deviations computed from the oxygen concentrations. It is important to note that the oxygen sensor OE-03 failed at about $t = 36$ seconds. Thus, the standard deviation for this sensor was measured using the data collected from the experiments 1 and 9 only. The average standard deviation for the oxygen sensors did not exceed a 0.75 threshold. Most standard deviations fall below 0.6, except for OE-07 and OE-10, whose standard deviations are 0.7323 and 0.6852, respectively.

TABLE 6.3: Standard deviation of the O_2 measurements within cavity section.

O_2 sensor	**SD_{min}**	**SD_{max}**	**SD_{ave}**
OE-01	$1.1981x10^{-4}$	2.8284	0.2071
OE-02	$2.5501x10^{-4}$	1.0669	0.2969
OE-03	$3.4832x10^{-5}$	1.4161	0.1944
OE-04	$2.6098x10^{-3}$	2.5708	0.5871
OE-05	$1.7231x10^{-3}$	2.1969	0.4884
OE-06	$1.7425x10^{-4}$	2.3171	0.5807
OE-07	$8.3526x10^{-4}$	3.8402	0.7323
OE-08	$2.6021x10^{-4}$	1.7770	0.3807
OE-09	$5.7135x10^{-2}$	2.0078	0.3788
OE-10	$5.2375x10^{-3}$	4.6424	0.6852

Another parameter of interest measured in these experiments is the velocity of the gases, particularly the velocity of the air vented through the ventilation system. The ability to reproduce the velocities at the ventilation duct is imperative because these velocities are used to estimate the amount of air vented out of the cavity section. Thus, the velocities of the gases vented through the ventilation system for these three experiments are compared against each other in the left-hand side of Figure 6.9. The average velocity for each velocity sensor is calculated and displayed on the right-hand side of Figure 6.9. The standard deviations for all velocity sensors were computed and summarized in Table 6.4.

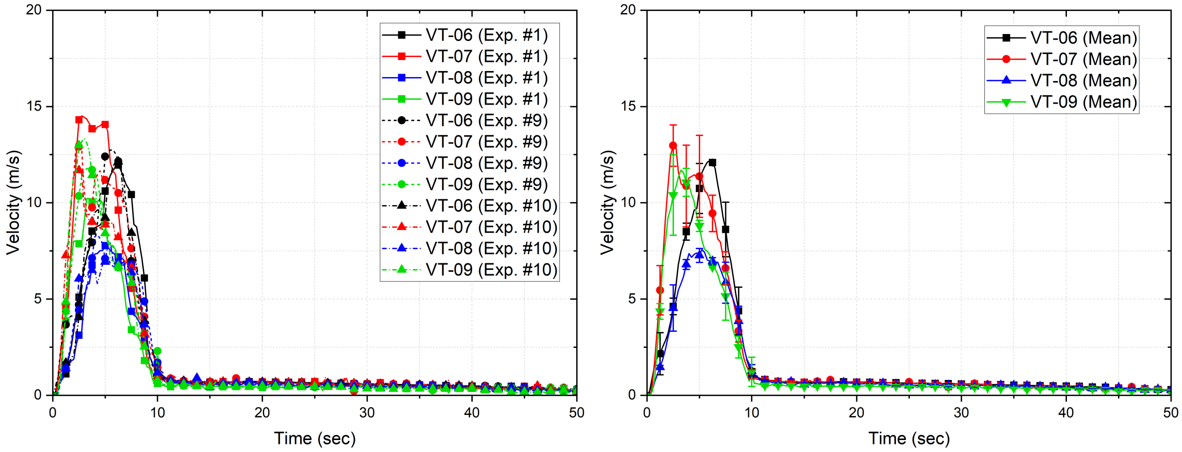

FIGURE 6.9: Measured velocities at the ventilation duct for experiments 1, 9, and 10 (left). Calculated average velocities and their respective standard deviation (right).

TABLE 6.4: Standard deviation of velocity sensors.

Velocity sensor	**SD**$_{min}$	**SD**$_{max}$	**SD**$_{ave}$
VT-01	$1.1444x10^{-04}$	0.7034	0.12581
VT-02	$8.9686x10^{-05}$	1.3043	0.17137
VT-03	$6.8759x10^{-04}$	0.7970	0.11834
VT-04	$3.3122x10^{-04}$	0.3559	0.05513
VT-05	$1.6400x10^{-03}$	0.6992	0.1257
VT-06	$5.7391x10^{-04}$	1.4139	0.14073
VT-07	$4.7200x10^{-03}$	2.3702	0.26703
VT-08	$2.7600x10^{-03}$	1.2007	0.13761
VT-09	$6.3400x10^{-03}$	2.1867	0.17765

6.2 TIME OF ACTIVE VENTILATION

During the depressurization of the pressure vessel in the scaled-down model, the ventilation duct gate is opened to allow the system to vent air out of the cavity section. The timing at which the gate of the ventilation duct is closed plays a crucial role in the amount of air that is vented and the amount of air that can re-ingress if any. Ideally, the ventilation duct should be left open only when air is vented and closed as soon as the system is no longer venting to prevent air re-ingress. Hence, it was deemed necessary to perform a sensitivity analysis where the timing of active ventilation was varied. This section tested five-time scales, where the ventilation gate was closed after 12, 22, 50, 65 seconds, and indefinitely. The configuration adopted for this sensitivity study is B01-V11-0.410.

The pressure evolution within the vessel for these experiments is compared against each other in Figure 6.10. This plot is presented to indicate the similarity in which the experiments were conducted and the overall depressurization rate of the vessel.

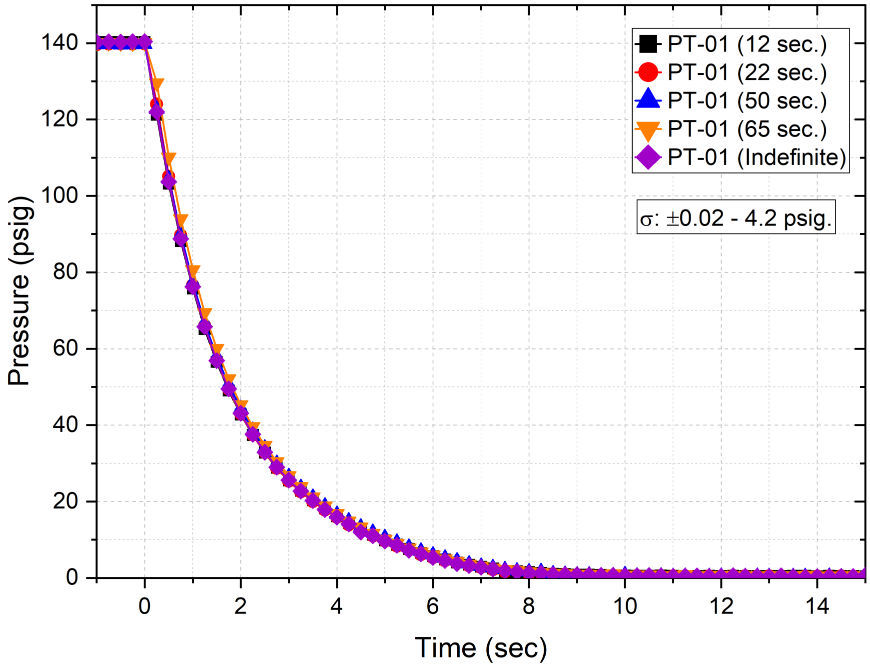

FIGURE 6.10: Measured pressure evolution within the vessel for experiments with varying active ventilation times.

The temperature evolution in the RB cavity region was monitored for the five experiments, then plotted together to look into the similarities and differences. Figures 6.11, 6.12, 6.13 compares the temperature measurements obtained from the sensors TE-01 through TE-06. The temperature measurements for sensors TE-01 and TE-02 show large temperature fluctuations within the first 200 seconds, followed by a slow increase in temperature. This increase in temperature eventually levels off, resulting in almost constant temperature measurement. An important feature to note in Figure 6.11 is that the experiment with a total activate ventilation time of 12 seconds has the highest temperature measurements, while the experiment with an indefinite active ventilation time has the lowest temperature measurements. Likely, leaving the ventilation gate open for an extended time allows the cavity section to cool down faster in the upper sections.

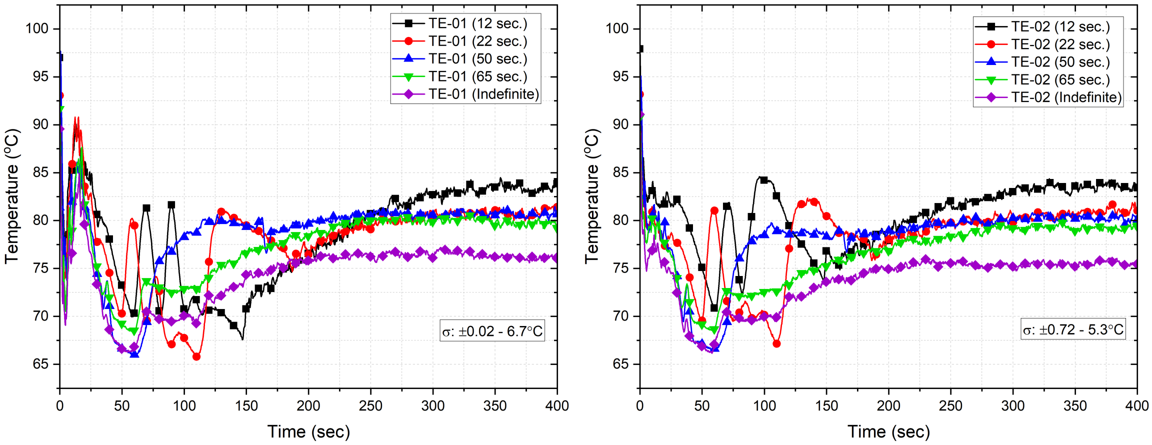

FIGURE 6.11: Measured temperatures from sensors TE-01 and TE-02 in the RB cavity section for experiments with varying active ventilation time.

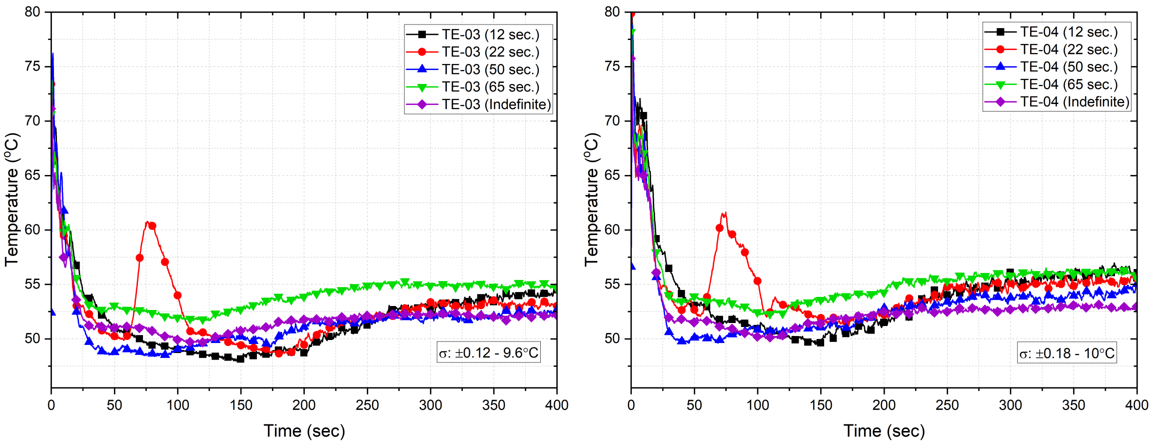

FIGURE 6.12: Measured temperatures from sensors TE-03 and TE-04 in the RB cavity section for experiments with varying active ventilation time.

Figure 6.12 shows that it takes longer for experiment #9 to show lower temperature measurements than the other experiments. Initially, it is unclear which experiment has the highest or lowest temperature. However, after about 250 seconds, the experiment with the ventilation gate open throughout the entire experiment shows lower temperature measurements over time.

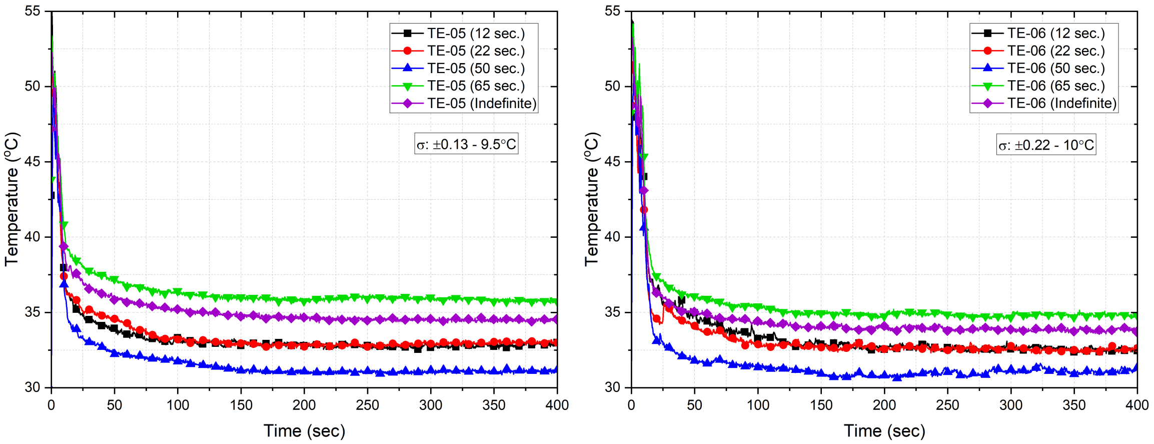

FIGURE 6.13: Measured temperatures from sensors TE-05 and TE-06 in the RB cavity section for experiments with varying active ventilation time.

The two plots in Figure 6.13 show that the thermocouples TE-05 and TE-06 of experiment #9 measured higher temperature values than most experiments. In this case, the highest temperature is reported from experiment #10, whose active ventilation time is 65 seconds, while experiment #1 shows one of the lowest temperatures. Interestingly, experiments #11 and #12 have very similar temperature evolution throughout the experiment. To look into the time-scale required to reach stable temperatures in the RB cavity section of the five experiments, the axial temperatures measured from sensors TE-07 through TE-18 are plotted and shown in Figures 6.14, 6.15, 6.16, 6.17, and 6.18.

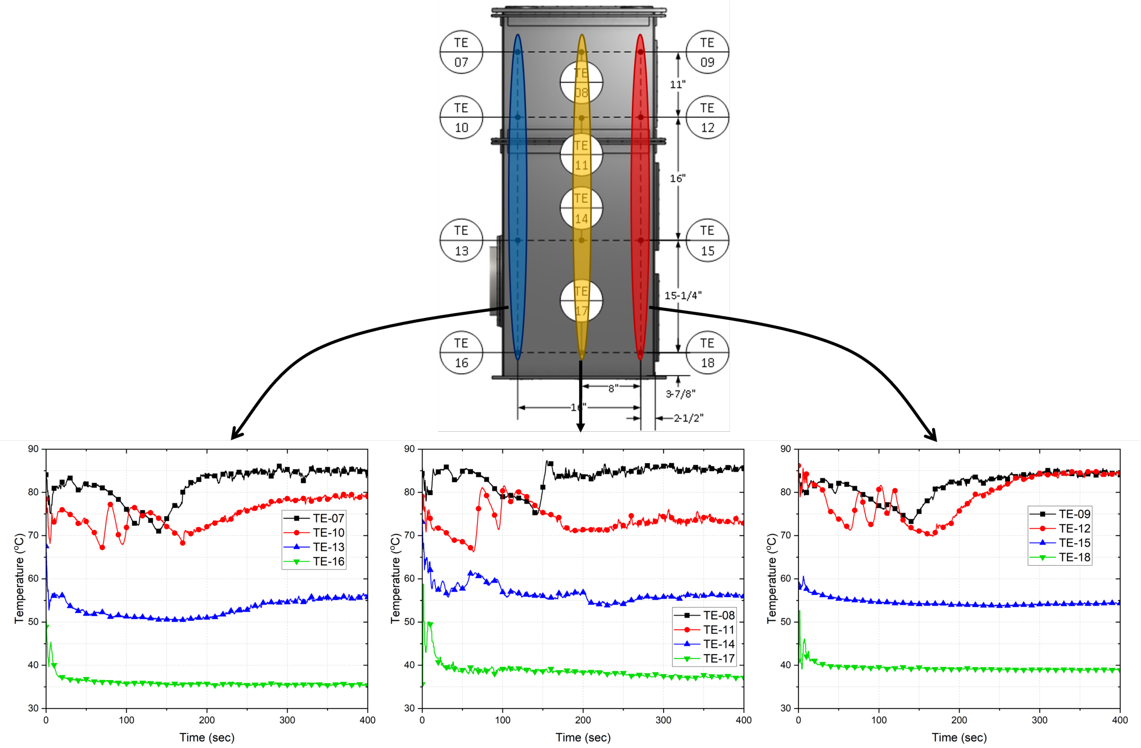

Figure 6.14: Axial temperature measurements of the cavity section of the RPV for experiment #12.

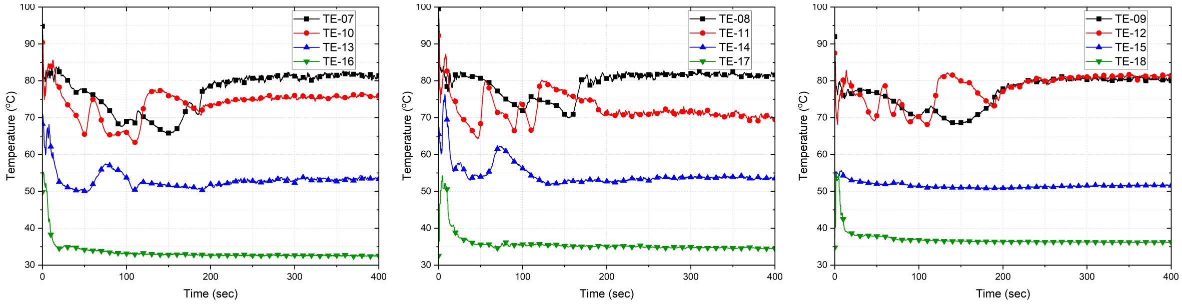

Figure 6.15: Axial temperature measurements of the cavity section of the RPV for experiment #11.

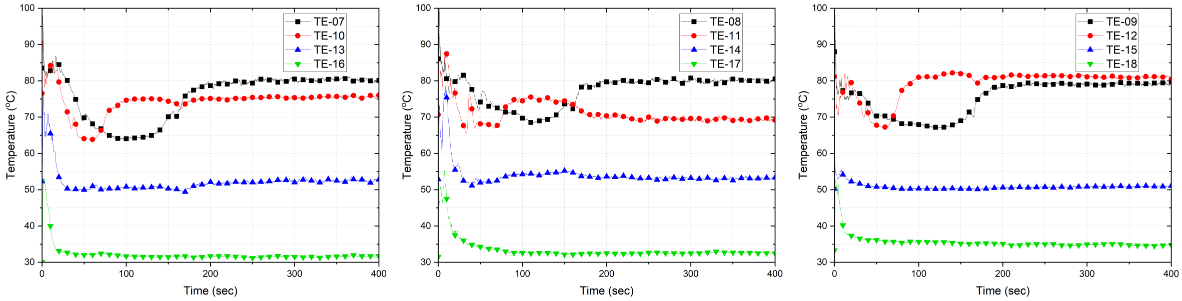

Figure 6.16: Axial temperature measurements of the cavity section of the RPV for experiment #1.

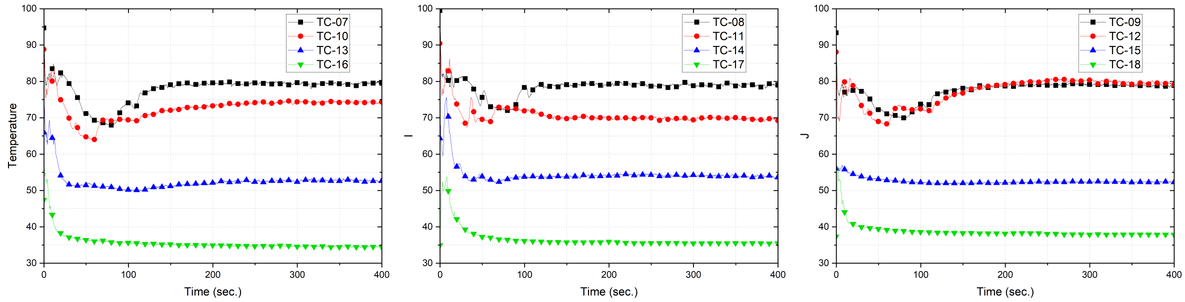

Figure 6.17: Axial temperature measurements of the cavity section of the RPV for experiment #10.

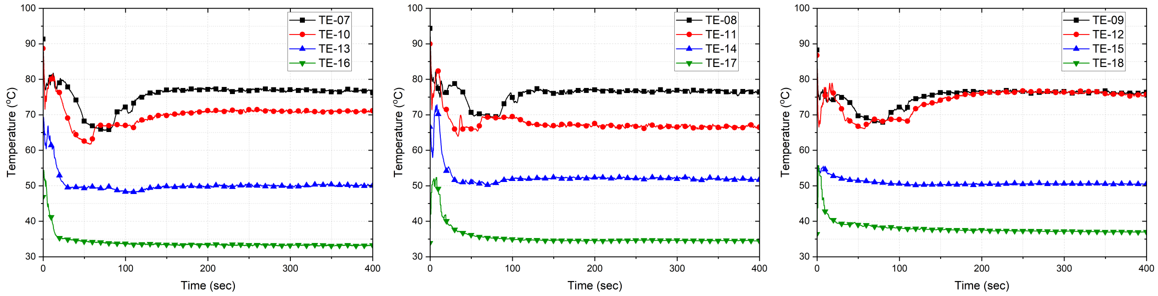

Figure 6.18: Axial temperature measurements of the cavity section of the RPV for experiment #9.

Generally, a little bit after 200 seconds, the temperatures level off. At this point, natural circulation under steady-state conditions is likely fully established. Forced convection predominates in the first couple of seconds, followed by a transition from forced to natural convection. Since the heaters continue to heat the inner section of the pressure vessel, the walls of the same increase due to radiative and convective heat transfer. Hence, natural circulation can occur within the cavity section as the walls of the pressure vessel act as a heat source due to the heat added by the electric heater rods.

In contrast, the walls of the containment building can act as a heat sink since its heat can be dissipated to the environment. To corroborate this idea, velocity measurements were taken in two different points. Two velocity sensors were mounted on the top and bottom of the axial cross-vessel duct, and their measurements are depicted in Figure 6.19. As it can be seen, the velocity in the cross-vessel section is high at the beginning of the experiment, and the velocity slowly decreases until it reaches a plateau. One important feature than can be seen in Figure 6.19 is that the velocities measured at the bottom of the axial cross-vessel are noticeably higher than at the top for all experiments.

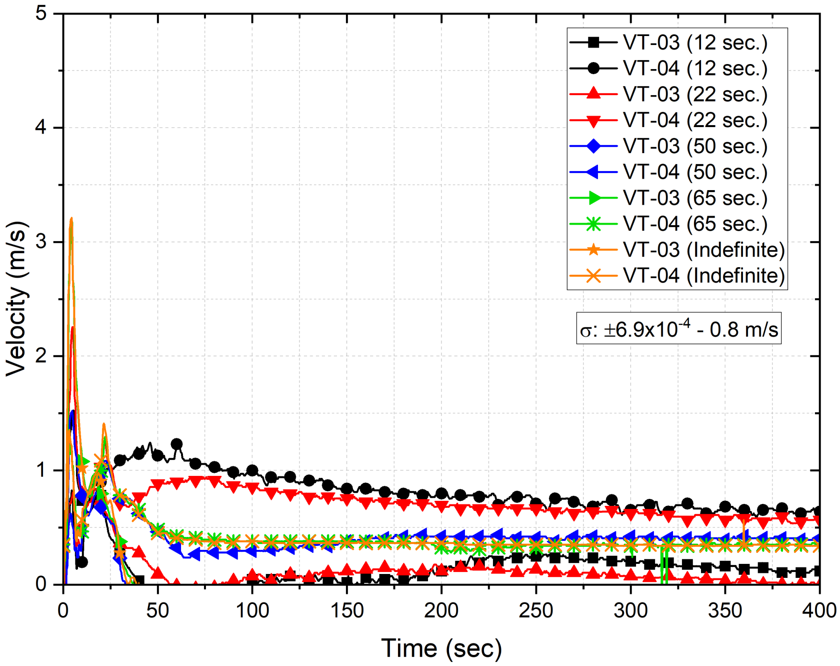

FIGURE 6.19: Velocity measurement in the cavity section of the cross-vessel duct with their respective error band for experiments with varying active ventilation time.

The driving factor for the timing of active ventilation for the experiments was determined based on oxygen measurements. Therefore, the measurement of the oxygen sensors on the RB for the different experiments was compared against each other to evaluate the different active venting times. Figures 6.20 through 6.23 show the different oxygen measurements at different heights within the RB cavity region.

The oxygen sensors for experiment #12, which had an active ventilation time of 12 seconds, seemed to have failed after 100 seconds following the beginning of the depressurization event. According to SST Sensing Ltd. (2017), certain conditions can affect the operation of the sensors. The possible reason for their failure is due to the long time exposure of the sensors in environments with little free oxygen. The sensors' exposure in an atmosphere with little free oxygen is denoted as "*reducing atmosphere*". The oxygen sensors at the moment of their failure measured a concentration of about 5% or lower. Their exposure to low oxygen concentrations lasted for over 100 seconds which could have affected the sensors.

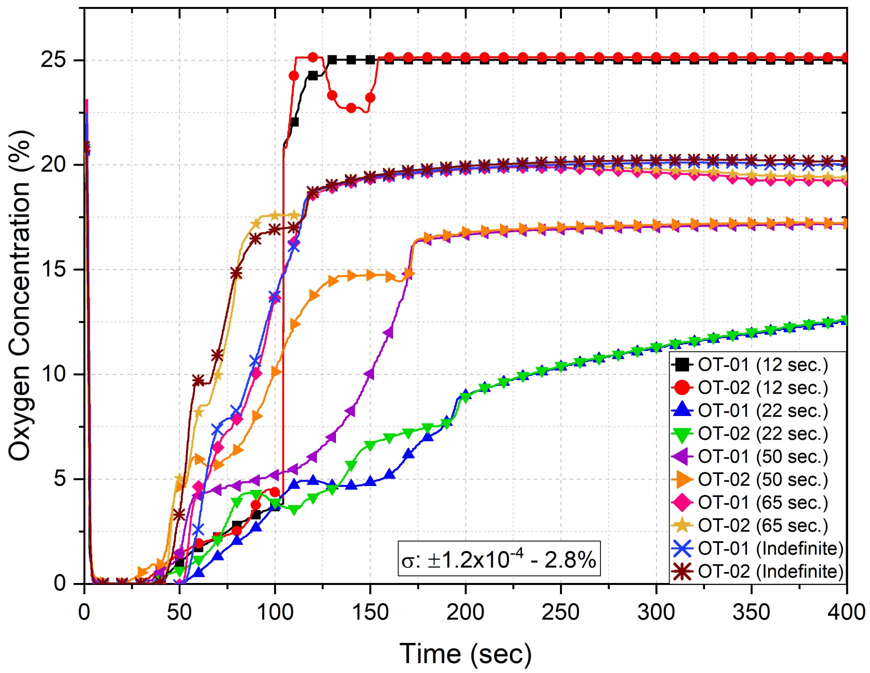

FIGURE 6.20: Oxygen measurement of sensors OT-01 and OT-02 of the RB cavity section for experiments with varying active ventilation time.

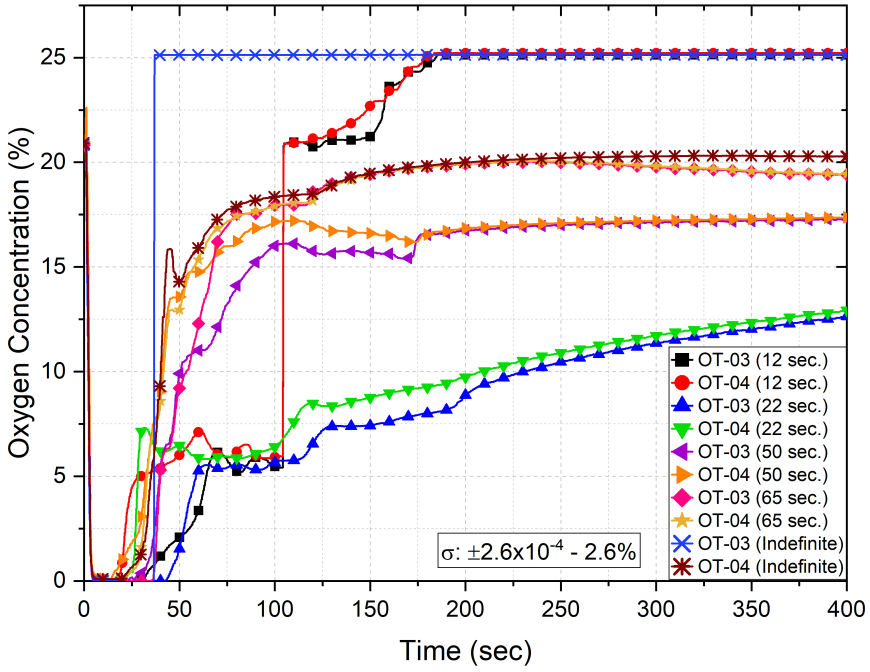

FIGURE 6.21: Oxygen measurement of sensors OT-03 and OT-04 of the RB cavity section for experiments with varying active ventilation time.

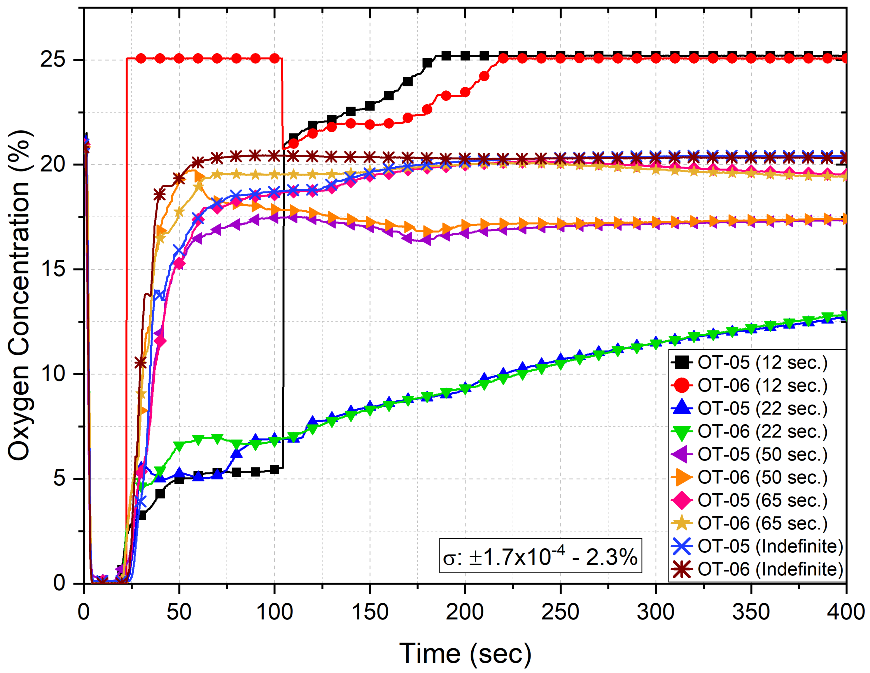

FIGURE 6.22: Oxygen measurement of sensors OT-05 and OT-06 of the RB cavity section for experiments with varying active ventilation time.

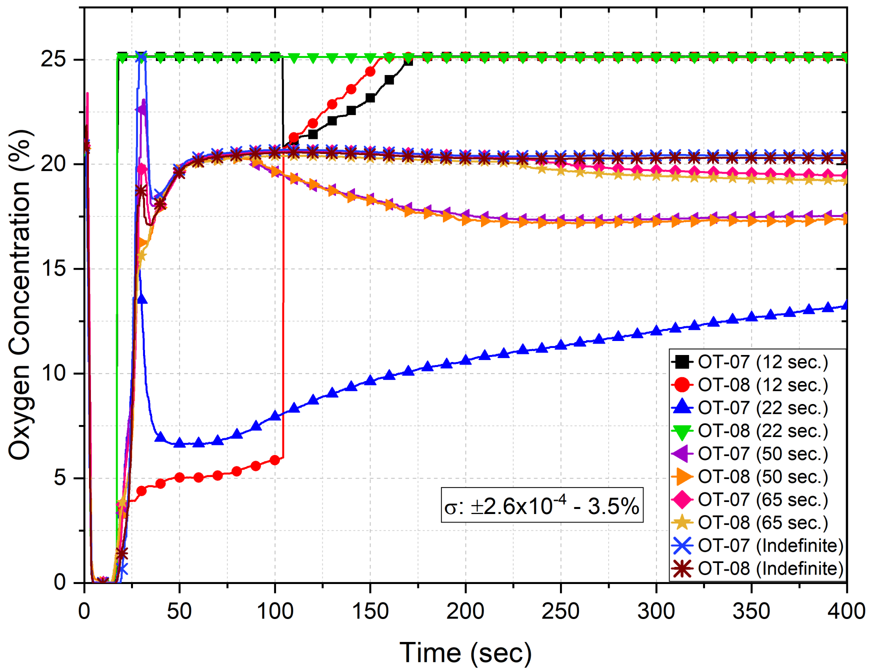

FIGURE 6.23: Oxygen measurement of sensors OT-07 and OT-08 of the RB cavity section for experiments with varying active ventilation time.

The experiment with an active ventilation time of 22 seconds yielded positive results as the oxygen concentration was significantly reduced. Only one out of the ten oxygen sensors failed in this experimental configuration. A feature worth noting is that the oxygen concentration for this experiment seems to increase at a prolonged but constant rate in the cavity section of the RB. This behavior is also observed in the cavity section of the PCV (refer to Figure 6.25). A possible explanation for this behavior is that the containment building of the scaled-down experimental facility has small leaks. Ideally, this scaled-down containment building should be air-tight, meaning helium and air cannot escape from the cavity region of the containment building. The containment building of the scaled-down HTGR contains small leaks that could not be identified. Some leaks were identified and treated. For instance, in the past, helium was leaking through small openings located on the multiple penetrations used to allow the electric heater wires to protrude out of the experimental facility, refer to Figure 6.24.

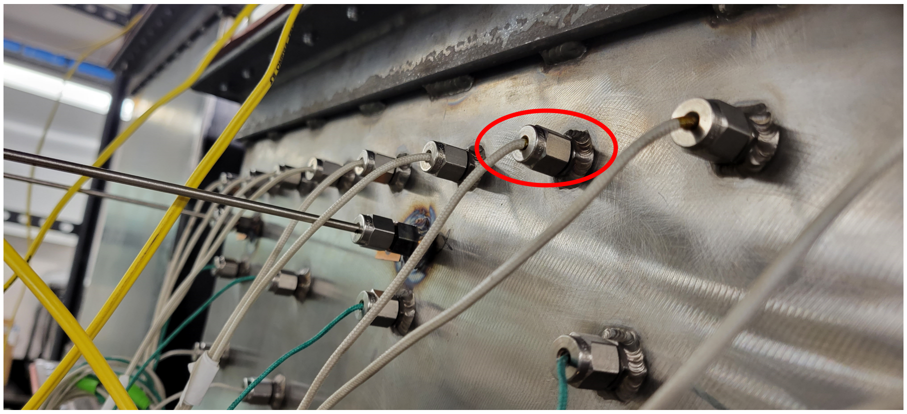

Figure 6.24: Electric heater wires protruding out of the scaled-down containment building.

The porous nature of these wires does not allow for a perfect isolation of the gases within the cavity section of the scaled-down facility from the environment. Consequently, when the atmosphere of the cavity section is deficient in air, helium will tend to escape through such leaks, and air will re-enter the cavity through other leaks. In an attempt to reduce the leaking rate, Polyimide film tape was applied to the electric heaters' wires.

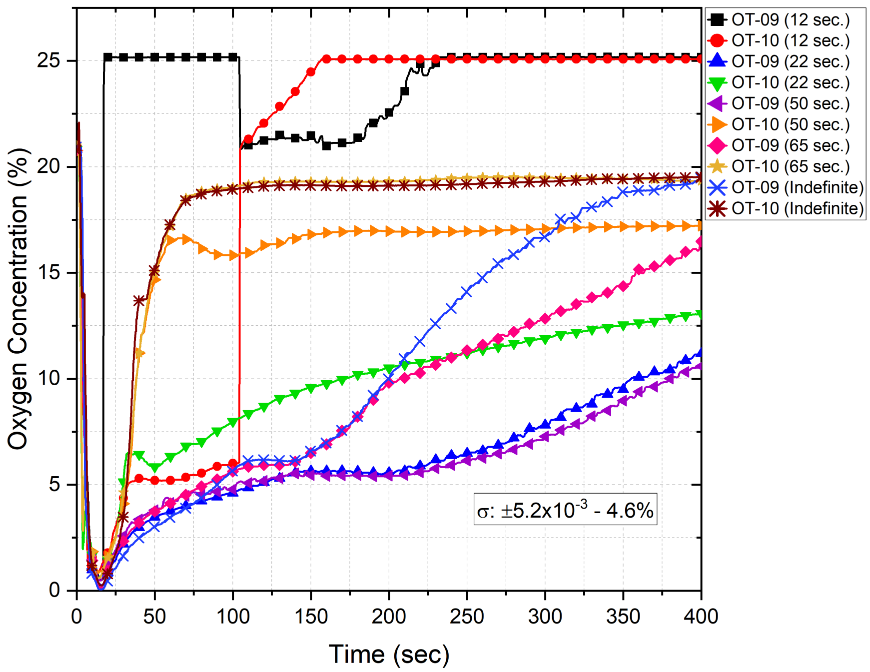

Figure 6.25: Oxygen measurement of sensors OT-09 and OT-08 of the cavity section of the PCV for experiments with varying active ventilation time.

While the experiment with active ventilation of 22 seconds yielded better results than the experiment with 12 seconds, similar issues with the oxygen sensors were encountered when a smaller break size was tested. Thus, a new experiment was executed where the timing of active ventilation was increased to 50 seconds. Figures 6.20 through 6.23 show that the oxygen sensors did not fail. The oxygen sensors did not experience any difficulties—nonetheless, a significant amount of air re-ingress from the ventilation duct. While helium is expected to continue escaping through the penetrations for the electric heaters wires, the leakage rate is significantly slower to the point that it seems that the oxygen concentration within the cavity section has reached a plateau. Another experiment with the same configuration and initial conditions was executed, but the timing of active ventilation was different. In this case, the ventilation duct gate was never closed. This means that the cavity section was utterly exposed to the environment throughout the entire experiment. This experiment is meant to provide a comparison between a 50 second and indefinite active ventilation time. The oxygen concentration plots illustrate that the RB cavity was replenished with fresh air in about 150 seconds when the ventilation duct gate was left open. This indicates the importance of studying the active ventilation time-scale to prevent air ingress.

6.3 BREAK SIZE

Part of the sensitivity analysis is to determine the influence of the break size on the oxygen concentration within the RB and how the gas dynamics change within the same. For this analysis, four break sizes were tested, where the diameters of the brakes are 0.410, 0.250, 0.188, and 0.125 inches. The rate of helium discharge into the cavity section heavily depends upon the break size. This difference can be better visualized by looking into the pressure evolution of the vessel as shown in Figure 6.26.

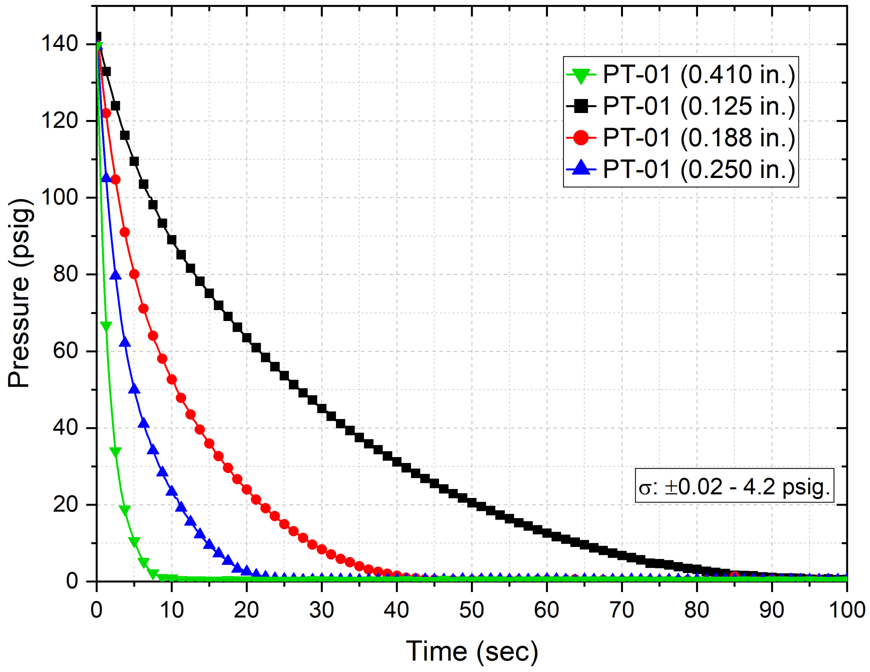

FIGURE 6.26: Measured pressure evolution within vessel for varying break sizes.

The pressure plot shows that the smaller the break size, the slower the vessel depressurizes. For a break size diameter of 0.410 inches, the vessel depressurizes within 15 seconds. The break diameter of 0.250 inches depressurizes slower as it completes its depressurization process within 30 seconds. For the other two cases, 0.188 and 0.125 inches, the depressurization is complete within 45 and 100 seconds, respectively. In addition to the pressure measurements, the temperature in the cavity section was compared for the different experiments. Figures 6.27, 6.28, and 6.29 provide a visual representation of the temperature magnitude for the four different experiments in the cavity of the RB.

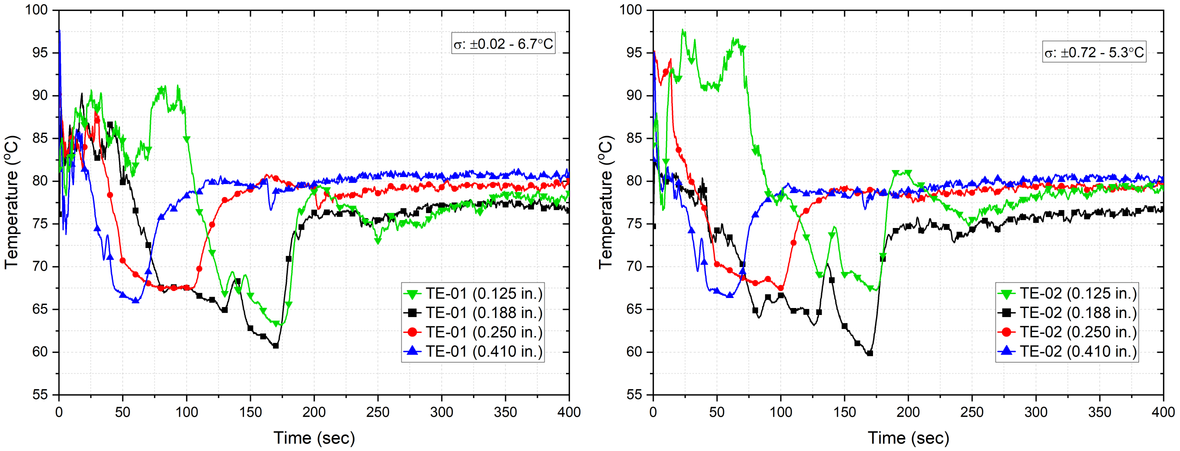

Figure 6.27: Measured pressure evolution within vessel with their respective error band for varying break sizes.

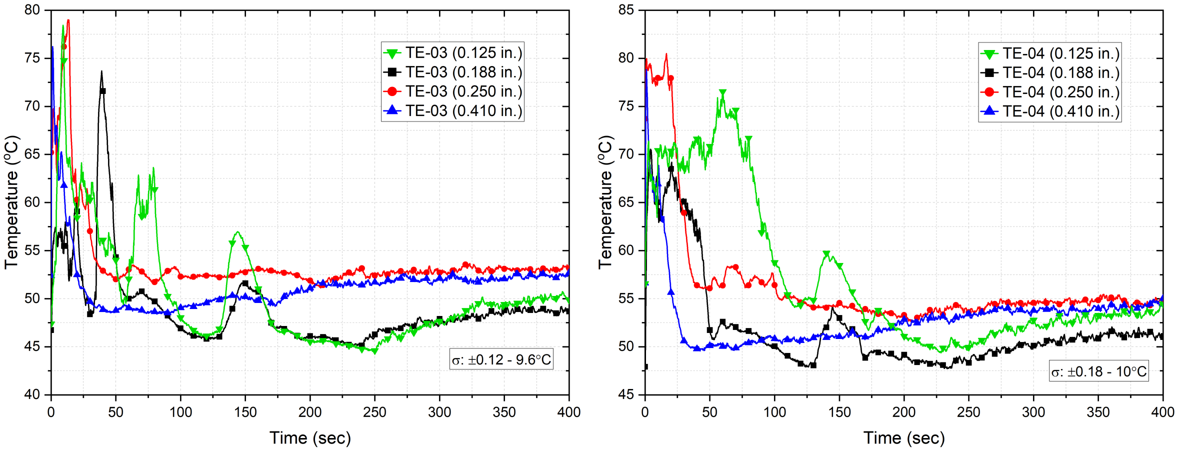

Figure 6.28: Measured pressure evolution within vessel with their respective error band for varying break sizes.

The temperature plots display important features worth noticing. For instance, the gas mixture remains turbulent for longer periods as the depressurization of the vessel is elongated. This feature is highly noticeable in Figure 6.27 as the experiment with a break size diameter of 0.125 inches continues to show large changes in temperature within the first 250 seconds. Although the depressurization process is complete within 100 seconds, the gas mixture is still influenced by the forced convection

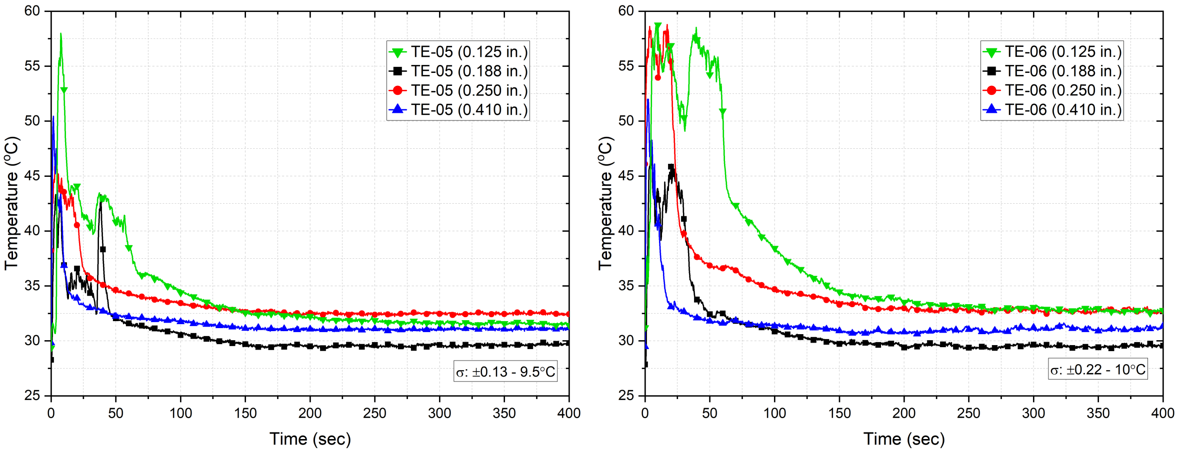

Figure 6.29: Measured pressure evolution within vessel with their respective error band for varying break sizes.

resulting from the helium jet outlet. Another feature that can be observed in the temperature plots displayed in Figure 6.27 is that the temperature considerably drops once the depressurization is complete. In lower sections (refer to Figures 6.28 and 6.29), the temperature drops prior the depressurization process is complete.

Oxygen measurements were collected during and after the depressurization of the vessel to provide a comparison of the different concentrations for different break sizes. Figure 6.30 though 6.34 show the oxygen concentration plots for this sensitivity study.

Figure 6.30 shows that the experiment's oxygen sensors that use the smallest break size (0.125 inches) fail. Section 6.2 mentions that the oxygen sensors can malfunction if exposed to an atmosphere with little free oxygen for a prolonged time. This behavior was noted in previous experiments as most of the air in the cavity section is pushed out of the scaled-down facility, causing sensors to fail. In this case, the oxygen sensors are likely failing due to their exposure to an atmosphere with little free oxygen. The slow depressurization of the vessel causes a better displacement of air from the RPV cavity to the cavity of the containment building of the PCV to the environment through the ventilation duct as helium is discharged at slower rate helium. This behavior significantly reduces the air concentration, ultimately leading to the oxygen sensors' malfunction.

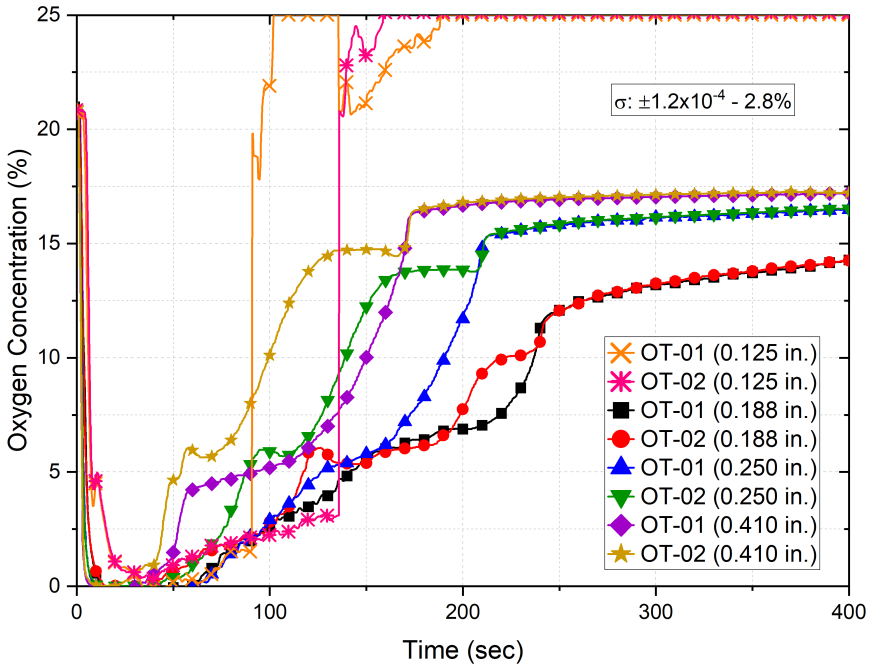

FIGURE 6.30: Oxygen concentration measured from sensors OT-01 and OT-02 at the cavity region of the RB for different break sizes outlets.

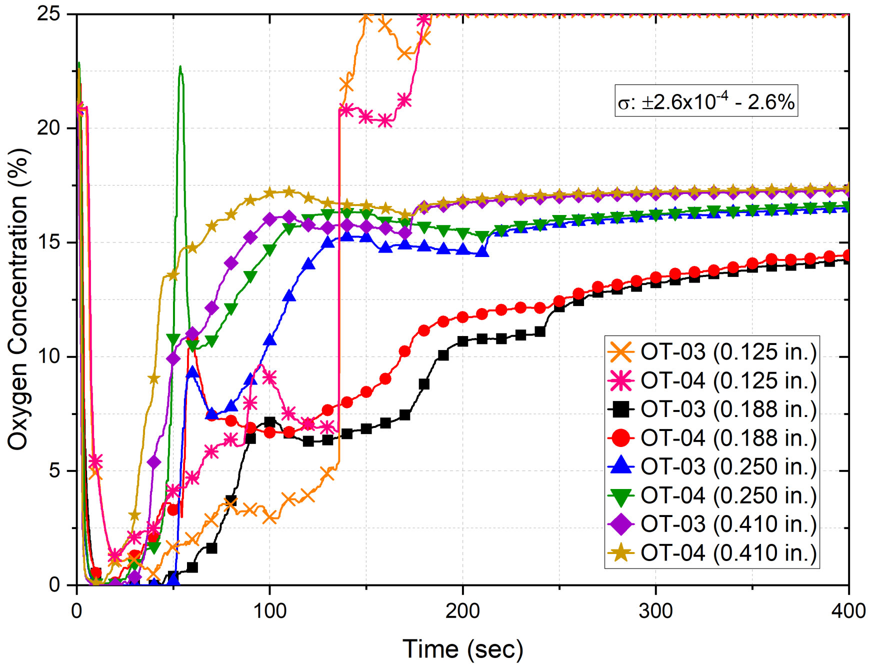

FIGURE 6.31: Oxygen concentration measured from sensors OT-03 and OT-04 at the cavity region of the RB for different break sizes outlets.

These experimental measurements indicate that the smaller the break size, the more vented air. An interesting feature worth noting is that the oxygen concentration

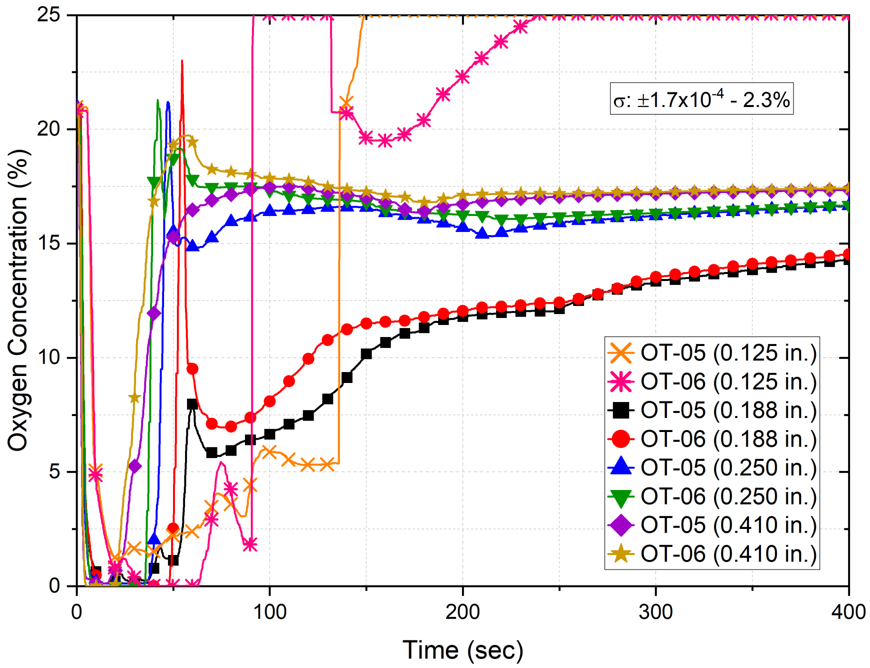

FIGURE 6.32: Oxygen concentration measured from sensors OT-05 and OT-06 at the cavity region of the RB for different break sizes outlets.

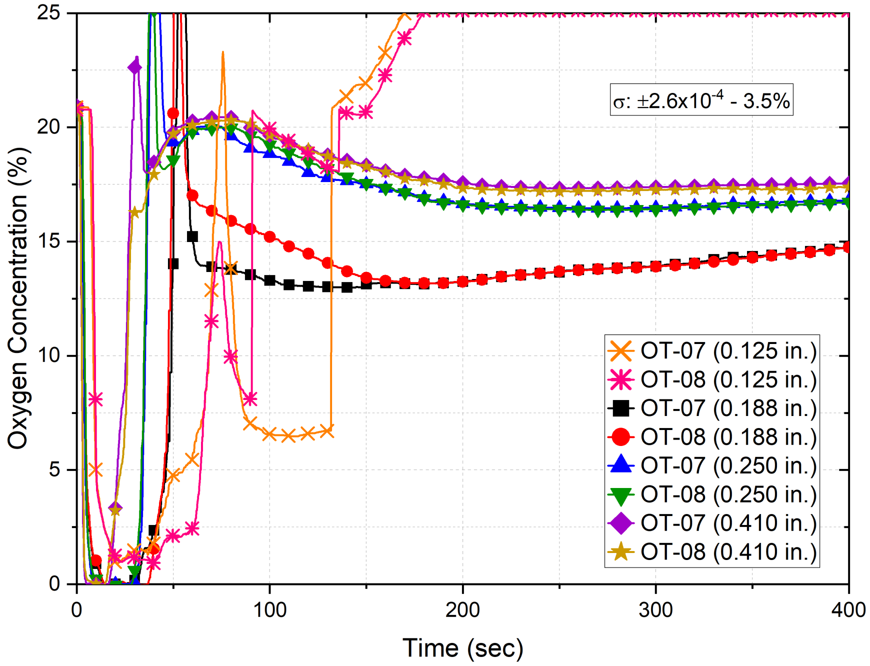

FIGURE 6.33: Oxygen concentration measured from sensors OT-07 and OT-08 at the cavity region of the RB for different break sizes outlets.

is quite different when the gas mixture is very turbulent. However, at a certain

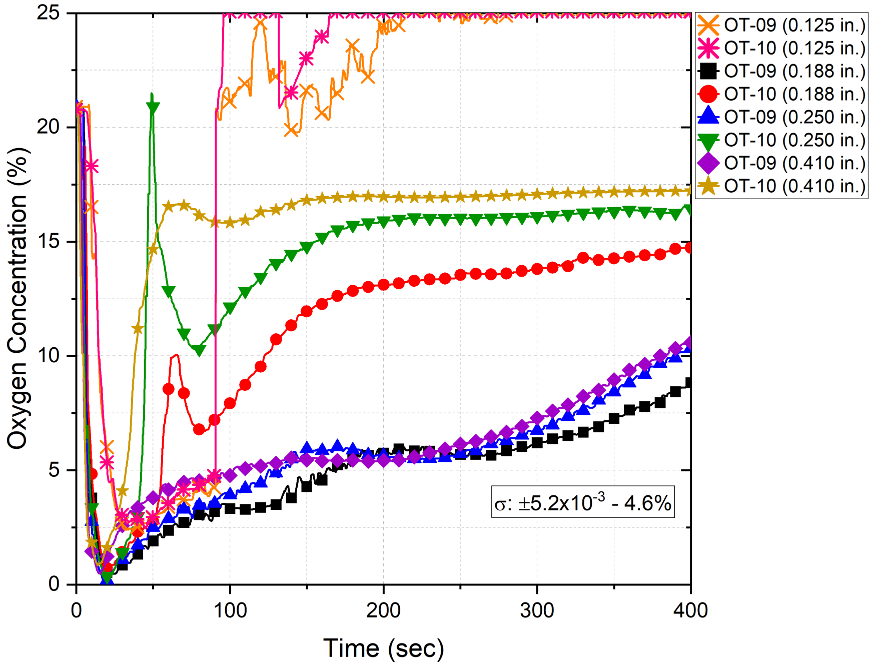

FIGURE 6.34: Oxygen concentration measured from sensors OT-09 and OT-10 at the cavity region of the RB for different break sizes outlets.

point in time, the oxygen concentration seems to be equal throughout the entire cavity region. To corroborate this finding, the oxygen concentration of experiments #1 through #4 were plotted together, and they are shown in Figures 6.35 through 6.37. It is important to note that the oxygen concentration for experiment #2 was not plotted because all the zirconium oxygen sensors failed.

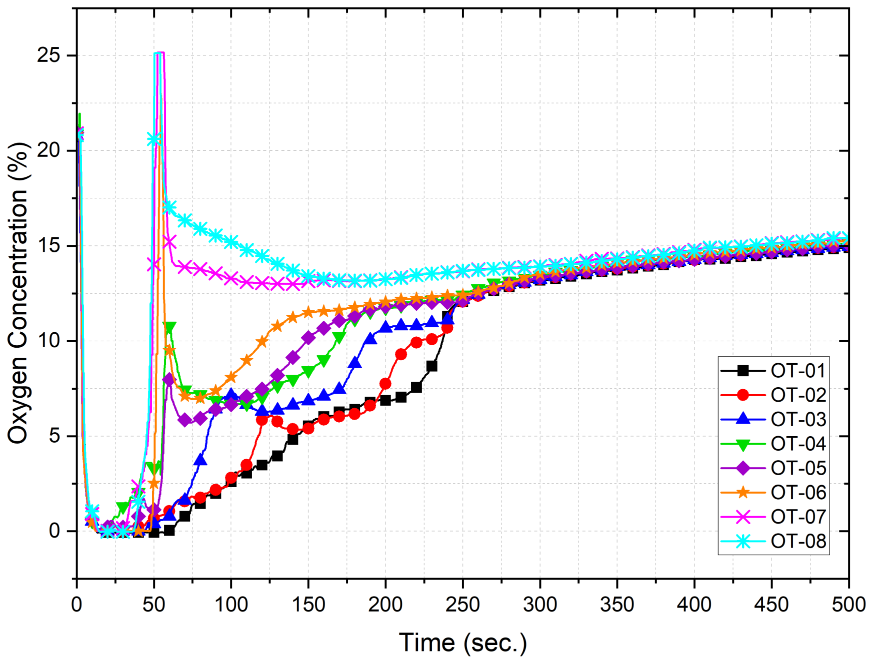

Figure 6.35: Oxygen concentration measured in cavity region of RB from experiment B01-V11-0.188

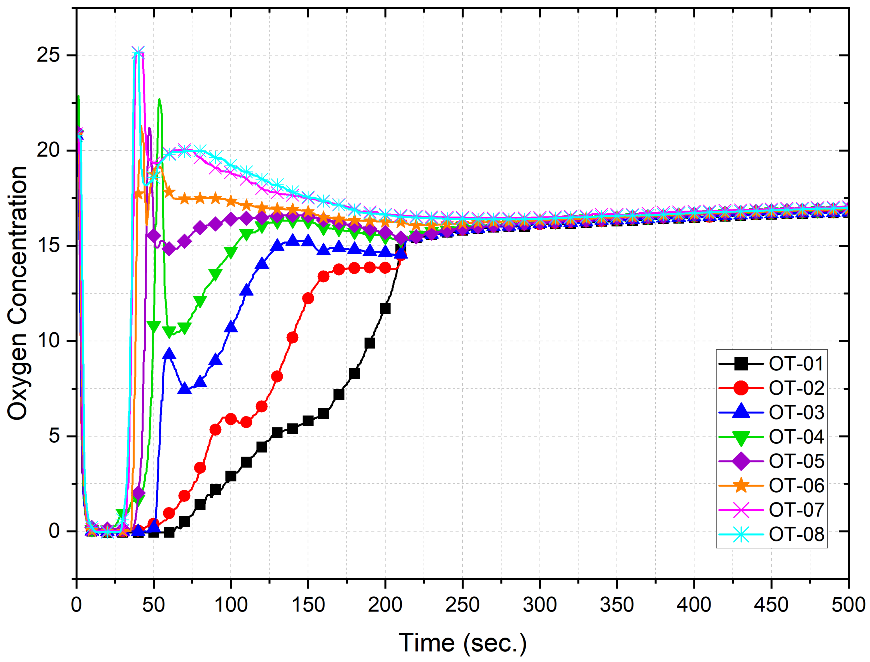

Figure 6.36: Oxygen concentration measured in cavity region of RB from experiment B01-V11-0.250

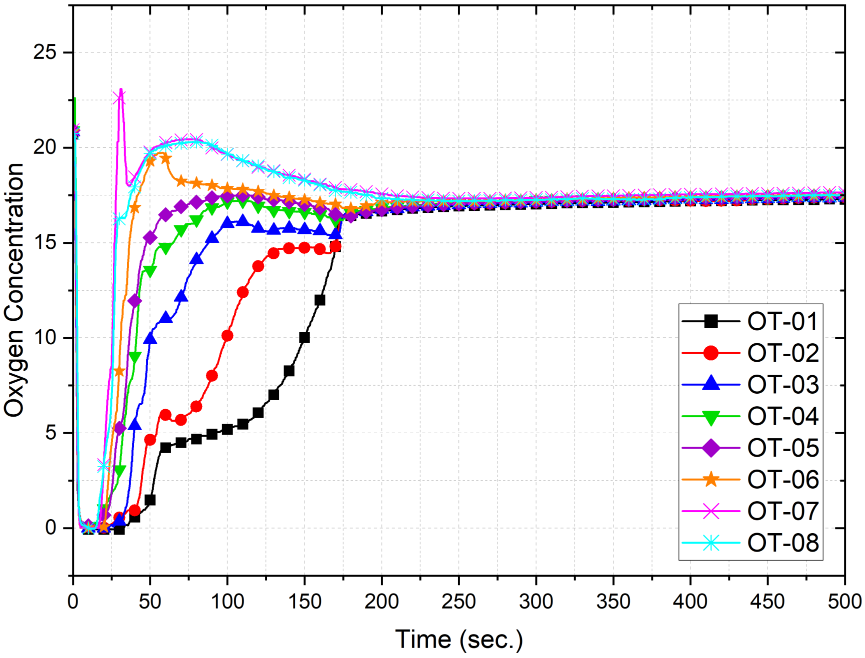

Figure 6.37: Oxygen concentration measured in cavity region of RB from experiment B01-V11-0.410

The velocities measured at the ventilation duct of the scaled-down facility are also compared in this section. Figure 6.38 indicates that the experiment with a large break size vents gases very fast within the first ten seconds. Thereafter, the velocity of the gases moving through the cavity section of the scaled-down facility reaches no greater than $1\,\mathrm{m\,s^{-1}}$. The velocities at the ventilation duct reached near zero a few seconds after closing the gate. The experiment with an outlet diameter of 0.250 inches is the second-highest experiment that vents gases at a high velocity. A noticeable difference between this experiment and the aforementioned is that gases are vented at high velocities for a more extended period. The experiment with an outlet size diameter of 0.410 inches vents gases at high velocities for about 10 seconds, whereas the experiment with an outlet size diameter of 0.250 inches vented gases at relatively high velocities for about 20 seconds. Similar behavior was captured experimentally for the experiment with a break size outlet diameter of 0.1875 inches. However, the magnitude of the velocities is lower than in the two previous experiments, and the duration at which gases are vented at relatively high velocities is longer (about 25 seconds). The smallest break size diameter experiment did not cause gases to be vented at a relatively high velocity. The maximum recorded velocity at the ventilation duct is about $1.4\,\mathrm{m\,s^{-1}}$, followed by an almost constant decrease of the velocity magnitude.

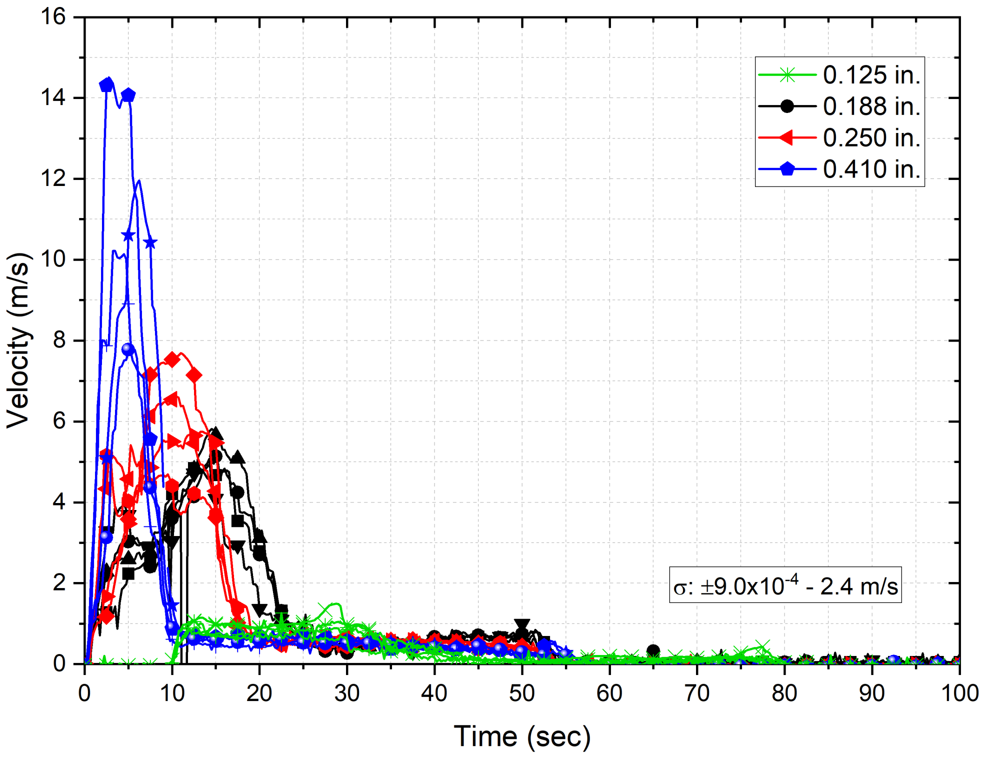

Figure 6.38: Measured velocity at the ventilation duct for varying break sizes.

6.4 BREAK LOCATION

Past reports have indicated how the location and orientation of the break can influence the rate of air ingress into the HPB. This study evaluates the influence of the orientation and location of the break outlet on the oxygen concentration in the cavity section. While the pressure vessel has seven outlet ports, only four of them are evaluated. The configuration tested are B01-V11-0.410, B03-V11-0.410, B04-V11-0.410, and B06-V11-0.410. These break locations are illustrated in Figure 6.39.

These four configurations were conducted at about the same initial conditions, where the scaled-down vessel was pressurized to 140 psig., and the average helium temperature was about 130^{o}C. The depressurization of the vessel for the different experiments was measured and illustrated in Figure 6.40.

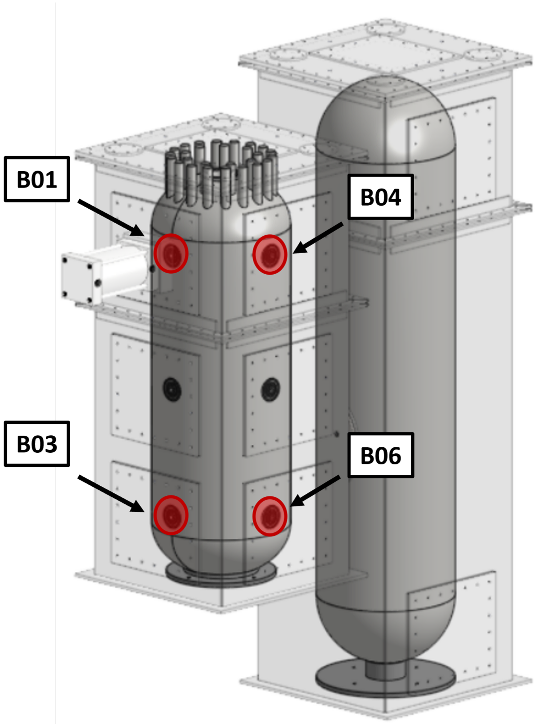

Figure 6.39: Schematic of HTGR indicating the location of the outlets tested.

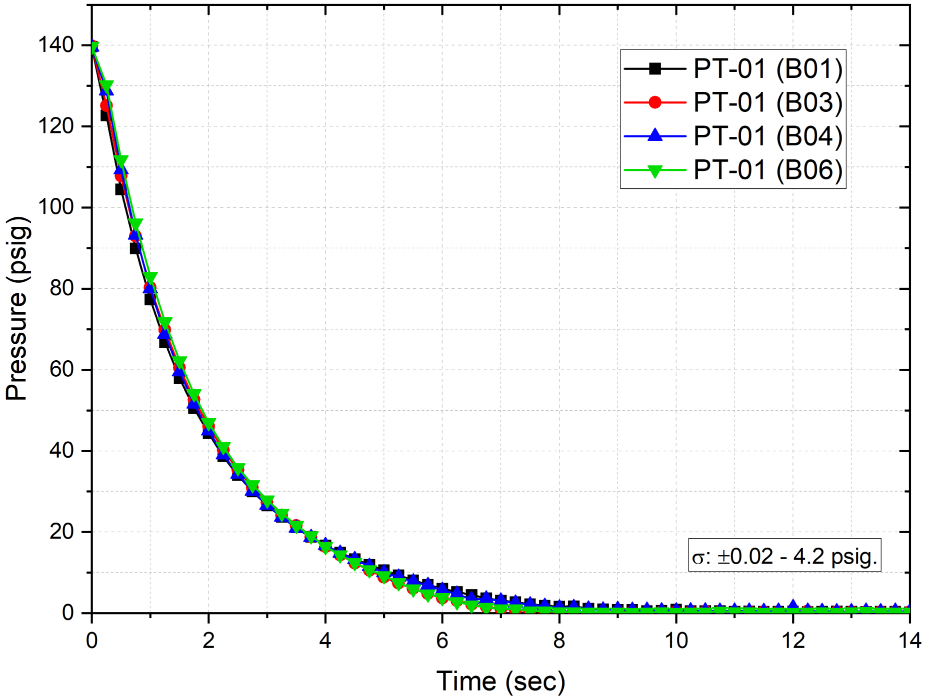

Figure 6.40: Measured pressure evolution within vessel for varying break locations.

The gas mixture temperature within the RB cavity was measured at different points. The temperature measurements collected from the thermocouples mounted on the frontal section of the containment building of the pressure vessel are shown in Figure 6.41. At the mid-upper section of the RB cavity, the gas mixture is noticeably turbulent within the first 100 seconds for all experiments, followed by a stabilization of the temperature that hovers around 77.5^{o}C. Once the depressurization was complete, the temperature dropped significantly until about $t = 50$ seconds, the same time the ventilation gate was closed. Thereafter, the temperature increased until the sensors measured relatively constant temperatures. In the mid-lower section, the temperature plot (Figure 6.41c) shows signs of turbulence within the first 35 seconds, mainly caused by the helium jet outlet. The temperature suddenly drops about the time the vessel completes its depressurization process. At about 25 seconds, the temperature increases at a relatively slow rate until the temperature levels off. The gas mixture is highly turbulent in the first 20 seconds in the lower section. After that, the temperature drops at a very slow rate over the following 180 seconds.

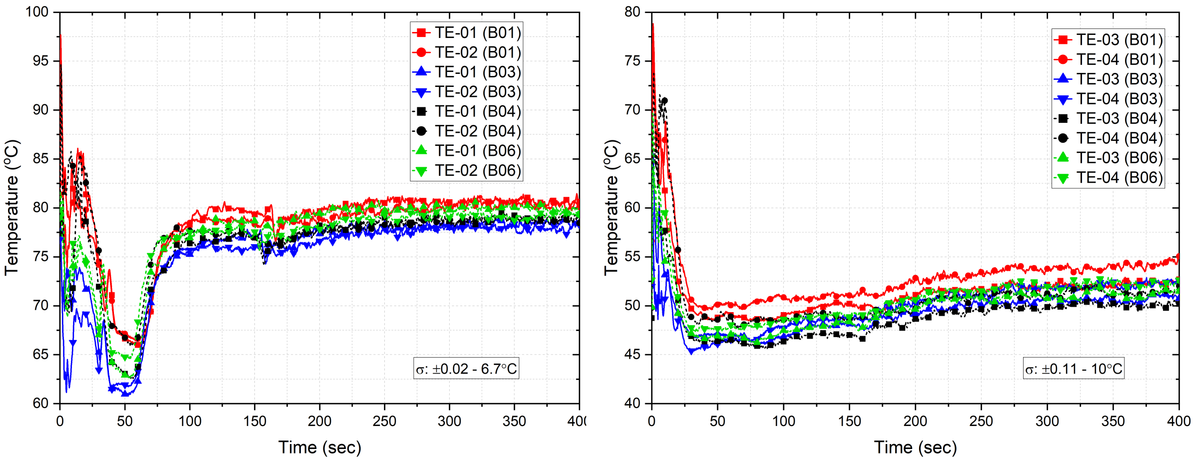

(A) Sensors TE-01 and TE-02.

(B) Sensors TE-03 and TE-04.

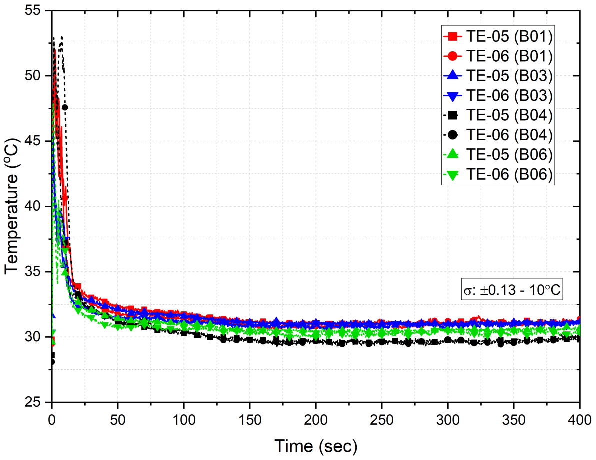

(C) Sensors TE-05 and TE-06.

FIGURE 6.41: Temperature evolution inside of the RB of the scaled-down HTGR for different break locations.

A common feature seen in the three plots displayed in Figure 6.41 is that in the first 55 seconds, the experiments that had the outlet located at the top of the RPV show higher temperature measurements than the experiments that had the outlet located in lower sections. A possible explanation is that the relatively high-temperature measurements are mainly attributed to the hot helium ejected from the pressure vessel. As the helium jet weakens, the hot helium can no longer reach the tip of the probes that are far away from the pressure vessel outlet. Hence, the further away the temperature sensors from the outlet, the sooner the temperature drops.

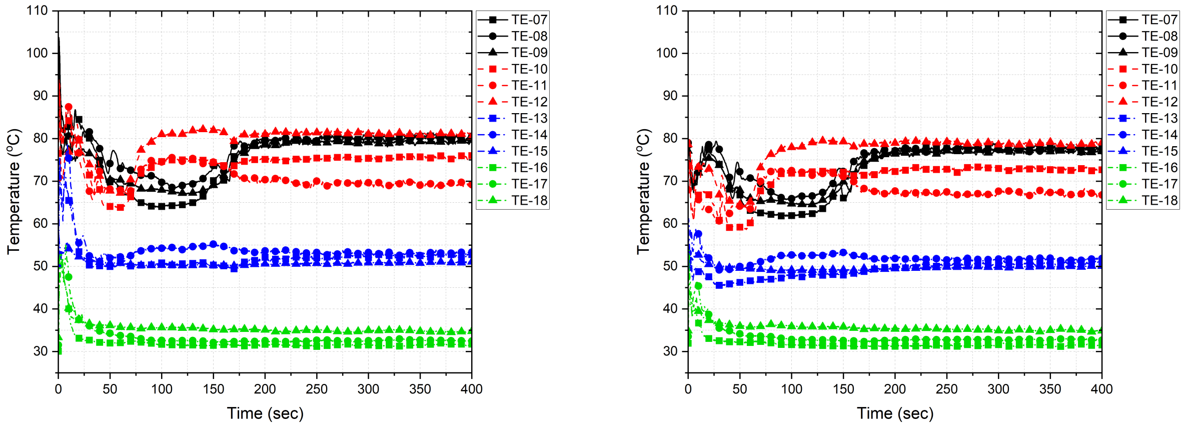

(A) Configuration B01-V11-0.410 (B) Configuration B03-V11-0.410

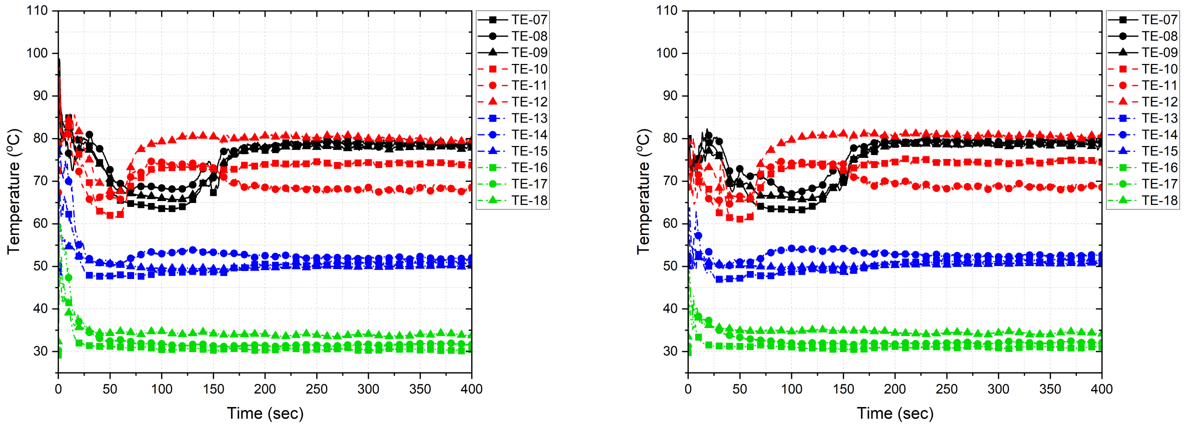

(C) Configuration B04-V11-0.410 (D) Configuration B06-V11-0.410

FIGURE 6.42: Temperature evolution inside of the RB of the scaled-down HTGR for different break locations.

Temperature measurements were also obtained from the back side of the cavity region where the pressure vessel is located. These temperature measurements are displayed in Figure 6.42. These plots show that the gas mixture takes longer to reach steady-state conditions in upper sections compared to lower sections, similar to the plots displayed in Figure 6.41.

Interestingly, the measured oxygen concentration for the different break configurations yields almost identical patterns, except for the experiment with configuration B01-V11-0.410. This configuration has about the same magnitude and features as the other configurations, but the timing is slightly off. For instance, the oxygen concentration measured from sensors OT-01 and OT-02 reaches a concentration of about 16.6% in about 167 seconds, followed by a relatively slow but steady increase of oxygen concentration by most experiments. For configuration B01-V11-0.410, a 16.5% oxygen concentration is reached at 177 seconds, followed by a steady increase in concentration.

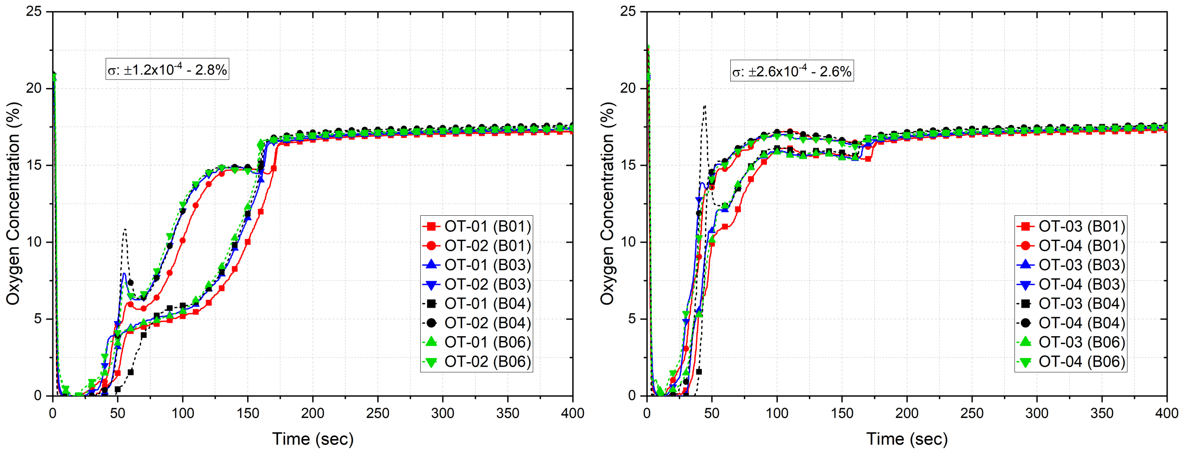

FIGURE 6.43: Oxygen concentration measured from sensors OT-01 through OT-04 at the cavity region of the RB for different break locations.

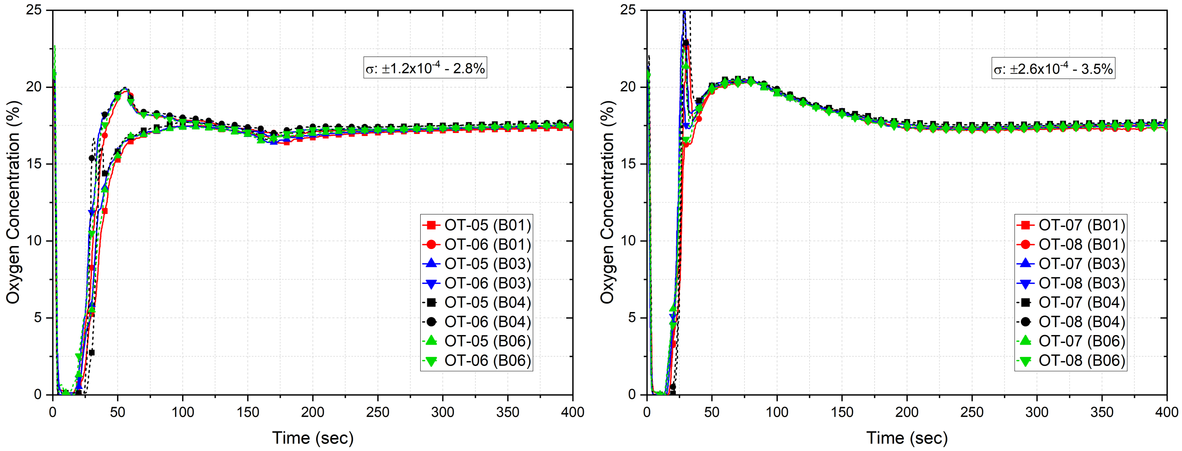

FIGURE 6.44: Oxygen concentration measured from sensors OT-05 through OT-08 at the cavity region of the RB for different break locations.

In contrast to Figures 6.43 and 6.44, the oxygen concentration in the cavity section of the PCV is considerably similar from experiment to experiment with negligible differences. Figure 6.45 shows the measured oxygen concentration in this section.

The velocity measured in the cavity section of the pressure vessel is plotted on the left-hand side of Figure 6.46 with a zoomed section depicted on the right-hand side. The highest peak velocities are reported in the experiments with break outlet B03

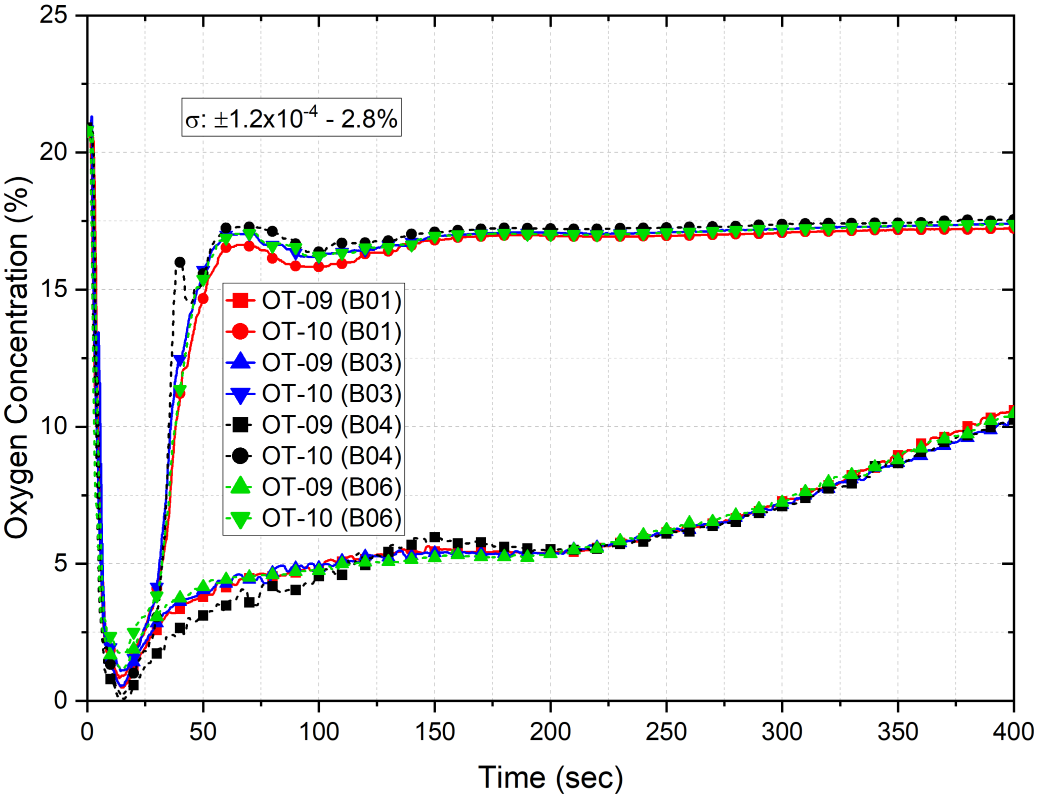

FIGURE 6.45: Oxygen concentration measured from sensors OT-09 and OT-10 at the cavity region of the RB for experiments with different break locations.

and B06 because the pressure vessel outlet is closer to these two velocity sensors in the bottom section. In contrast, experiments with break outlets at B01 and B04 report lower velocity peaks as the outlets are further away from these velocity sensors.

The velocities at the axial cross-vessel duct were measured and plotted in Figure 6.46. The peak velocities measured within the first 25 seconds are higher for experiments #5 and #7 than experiments #1 and #6. The rationale behind this behavior is due to the short flow path and low flow resistance for helium ejected from break locations B03 and B06.

The zoomed section of Figure 6.46 shows signs of natural circulation. The velocity of the gases measured at the bottom of the axial cross-vessel duct (measured from sensor VT-04) substantially drops to near $0.25\,\mathrm{m\,s^{-1}}$ about 60 seconds subsequent to the depressurization. Thereafter, the velocity ramps slightly, reaching a steady-state condition after about 175 seconds from the beginning of the depressurization

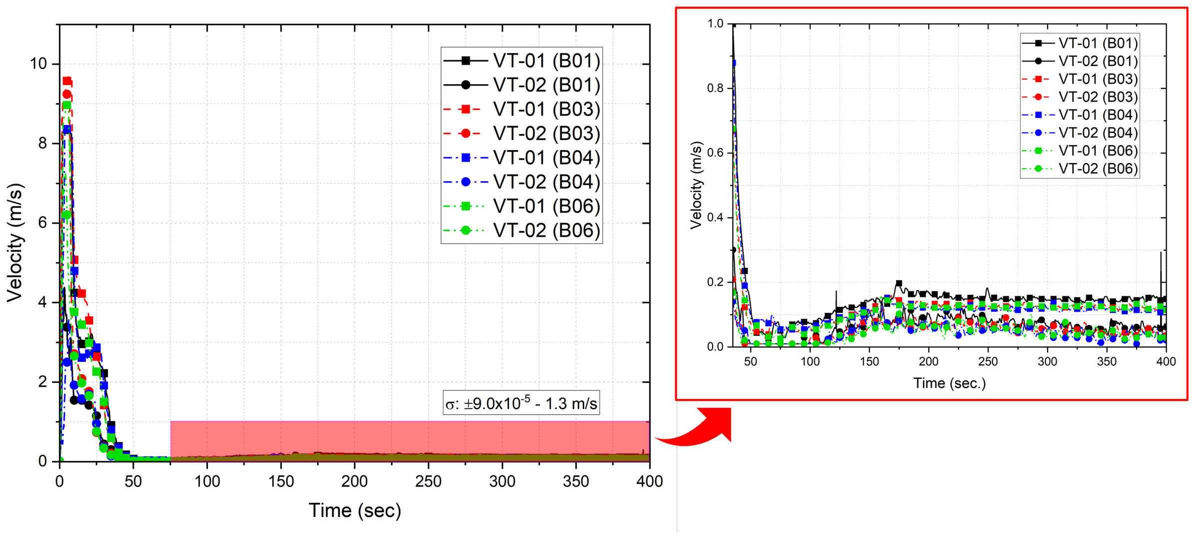

Figure 6.46: Velocity measurements from VT-01 and VT-02 at the cavity region of the RB for experiments with varying break locations.

process. This velocity increase can be attributed to natural circulation effects in the experimental facility as the electric heaters continue to heat the inner walls of the pressure vessel. Due to the temperature difference between the walls of the pressure vessel and containment walls, the gases heated by the pressure vessel are cooled down on the walls of the containment building. Generally, the hot gases move from the pressure vessel cavity section towards the cavity of the PCV because the walls of the latter are significantly colder.

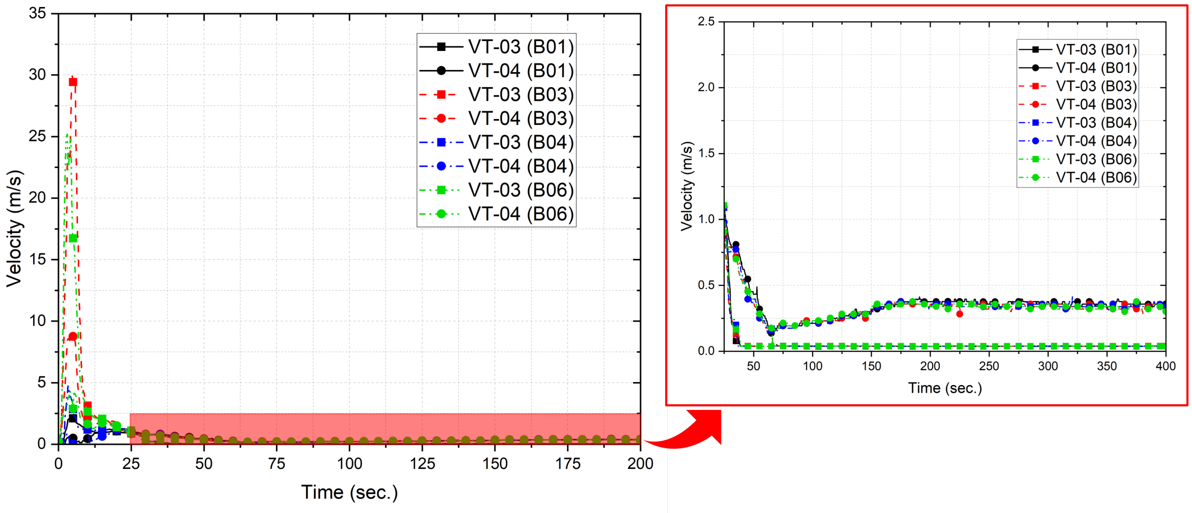

Figure 6.47: Velocity measurements from VT-03 and VT-04 at the cavity region of the RB for experiments with varying break locations.

Finally, the velocity at the ventilation duct was analyzed as well. The velocities measures in this section can estimate how much was vented out of the system. Figure 6.48 shows that the maximum velocity recorded is from the break outlet configuration B06, which has the shortest flow path and fewer flow resistances. The second highest velocities recorded are from the experiment with the break outlet located at B03. It is important to note that after $t = 10$ seconds, the sensors indicate that gases are moving in or out of the system through the ventilation duct until the ventilation gate is closed, at which the velocity drops to about zero after a few seconds. It is unknown whether gases continue to be vented or air is re-entering the cavity section. Based on oxygen measurements, air is likely re-entering the cavity section.

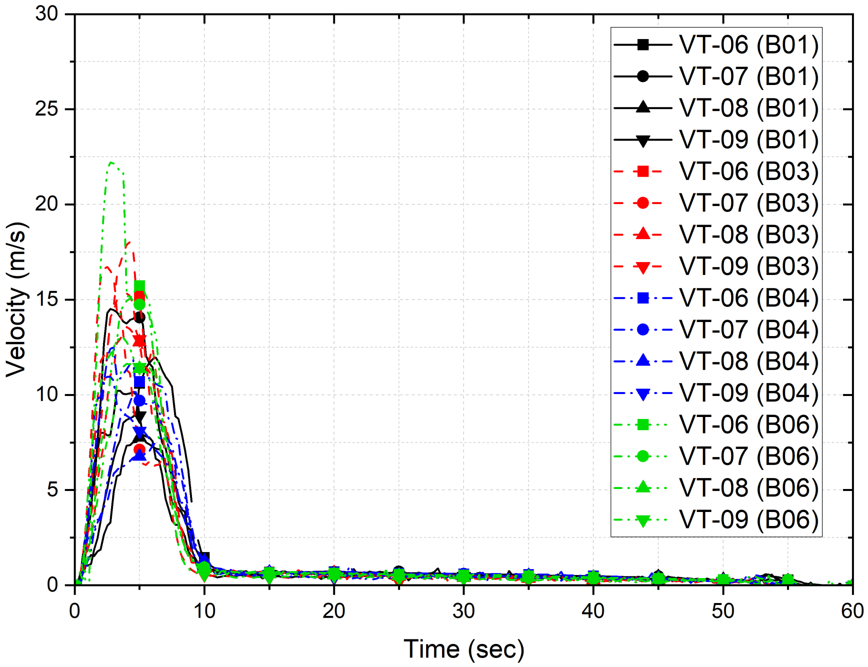

FIGURE 6.48: Velocity measurements at the ventilation duct for experiments with varying break locations.

6.5 POSITION OF VENTILATION SYSTEM

The position of the ventilation system could significantly influence the overall air concentration in the cavity section. Helium has a molecular weight of 4.0026 g/mol, whereas air has a molecular weight of 28.9647 g/mol. If air and helium are released in an enclosed containment, helium will move to the upper section while air will move to the lower section due to gravitational effects. With this concept in mind, the position of the ventilation system could influence the amount of air vented based on the elevation. Two configurations are compared to identify a setup that could vent more air out of the cavity section. Experiment #1 has a configuration B01-V11-0.410, which has the ventilation duct mounted in the lower section of the containment building of the PCV. The second configuration tested is B01-V12-0.410, where the initial conditions and configuration remain relatively the same, except for the ventilation system. This test, experiment #8, has the ventilation duct mounted in the upper section of the containment building of the PCV. Figure 6.49 shows the two positions tested (in red) where the ventilation duct was mounted.

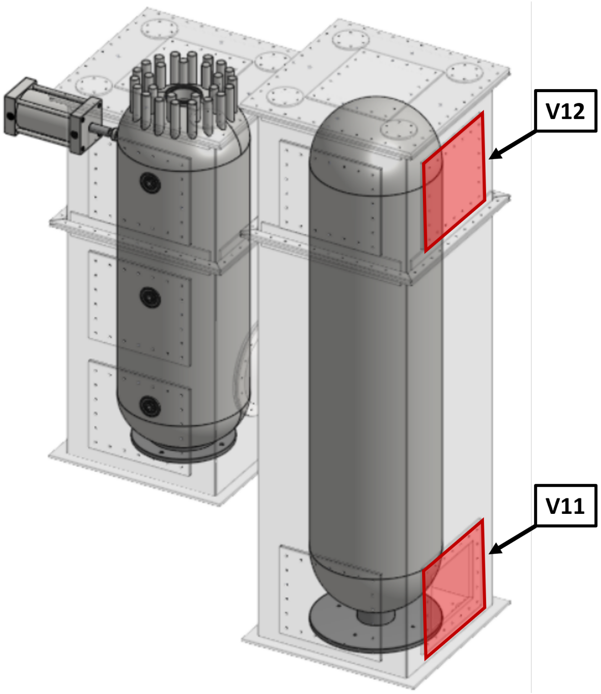

Figure 6.49: Schematic of the scaled-down HTGR indicating in red the sections where the ventilation duct is placed for this sensitivity study.

These experiments were conducted under the same initial conditions, where the average temperature and pressure of the helium were about 130°C and 140 psig. Figure 6.50 shows the pressure evolution of the vessels during the depressurization process for the experiments #1 and #8.

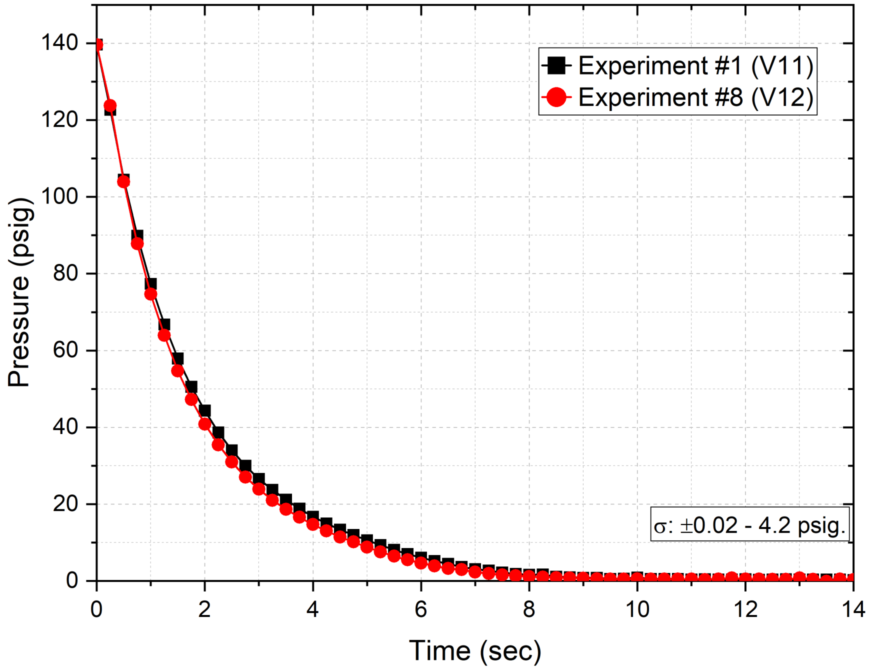

Figure 6.50: Pressure evolution of the scaled-down vessel for experiments #1 and #8.

Interestingly, the pressurization process of experiment #8 required applying a higher voltage to the heaters than in previous experiments. To achieve the desired pressure while maintaining steady-state conditions, the heaters were operated at a 180V compared to the 120V usually applied to previous experiments. Although the vessel was pre-pressurized at about the same pressure as the other experiments, and the heating process was similar to the previous experiments, the vessel had to be heated more than usual. It was later found that the vessel did not seal properly, so helium was leaking at a meager rate. The leakage rate was so small that the pressure sensors did not reflect a pressure drop. This leakage was believed to happen during the heating process when the pressure increased due to the heat input from the electric heaters. Because of the leakage, more heat was needed to achieve the desired pressure.

While the pressure sensors did not show any sign of pressure drop, the oxygen sensors were good indicators of this leakage. In addition, these zirconium dioxide oxygen sensors were critical to evaluating which configuration vents most of the air out of the cavity of the RB. Figure 6.51 shows the oxygen concentration at different elevations within the scaled-down reactor cavity for experiments #1 and #8.

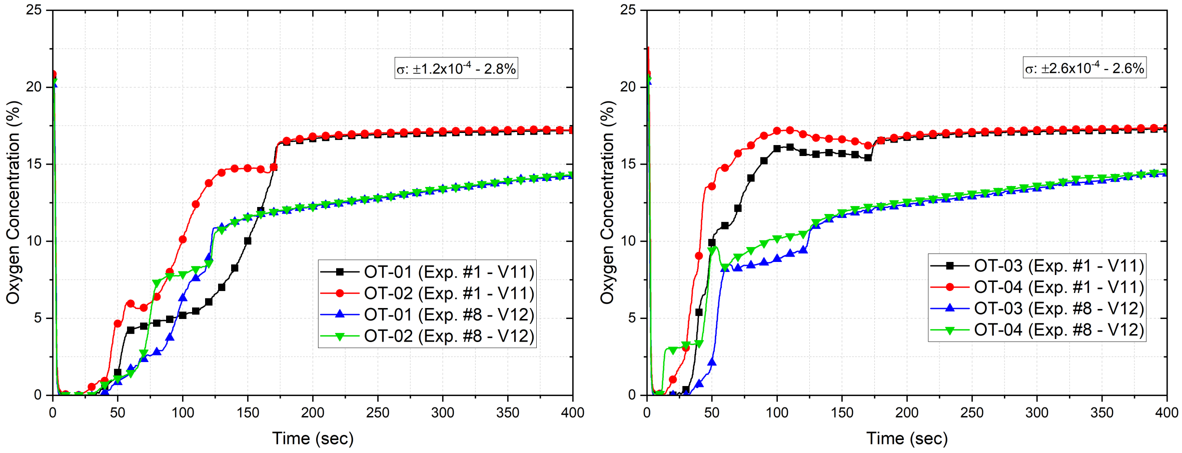

FIGURE 6.51: Oxygen measurements of the scaled-down RPV cavity section for experiments #1 and #8.

OT-01 measured an oxygen concentration of about 20.2%, which is about 0.5 lower than the average concentration in the fresh air prior to the beginning of the depressurization process. OT-02, OT-03, and OT-04 measured an oxygen concentration of about 20.4% right before the depressurization. Despite the leakage, it is believed that most of the leaked helium remained in the cavity section. This means that the air-helium mixture in the cavity section may differ, but the oxygen concentration may not be significantly compromised. From Figure 6.51, it can be seen that the oxygen concentration as a function of time for both experiments has a very similar pattern. However, the magnitude (O_2 concentration) and timing differ from each other. For the case scenario where the ventilation duct is placed in the lower section (V11), the O_2 concentration from sensors OT-01 and OT-02 goes from 0 to about 14.2% in a time-lapse of 120 seconds. In contrast, the case scenario where the ventilation duct is placed on the top, V12, goes from 0 to about 10.6% in the same time-lapse. Similar results can be observed in the right-hand-side of Figure 6.51 and the left-hand-side of Figure 6.52, where the O_2 concentration is lower when the ventilation is placed in the upper section of the PCV containment building compared to the other configuration.

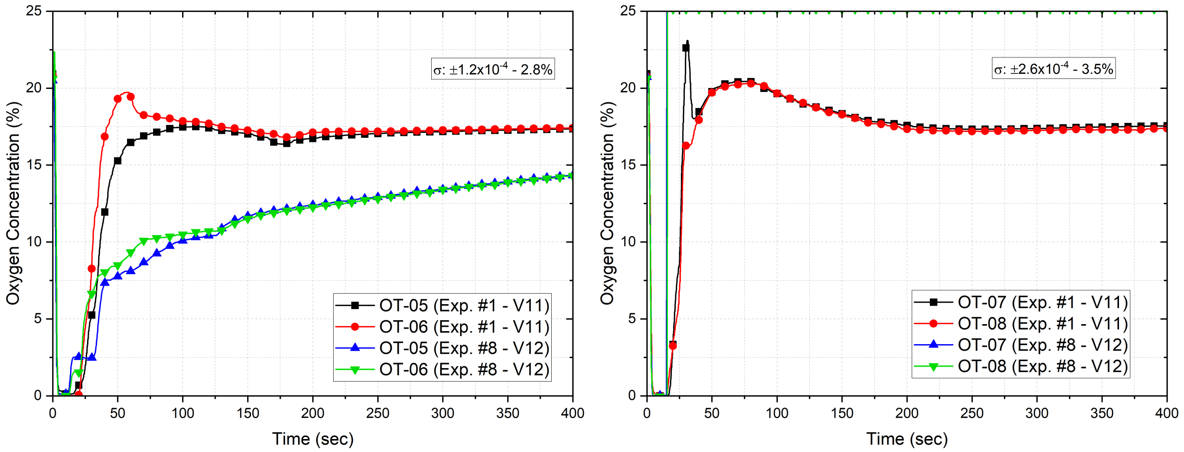

Figure 6.52: Oxygen measurements of the scaled-down RB for experiments #1 and #8.

Two features worth noting from Figure 6.52 is that the oxygen concentration in the reactor cavity for experiment #1 remains considerably high compared to experiment #8, where in some circumstances, the difference in oxygen concentration between both experiments is about 7%, and this difference narrows over time. Additionally, it is essential to note that the oxygen sensors OT-07 and OT-08 for experiment #8 failed in about 15 seconds following the beginning of the depressurization process. The drift of these two sensors prevents us from assessing the O_2 concentration in the lowest section of the cavity section. However, a reasonable assessment can be executed from the other six sensors.

Similarly, the oxygen concentration in the PCV containment building of experiments #1, and #8, was compared. Figure 6.53 shows that there is a large O_2 concentration difference from sensor OT-09 to OT-10 for experiment #1 within the first 400 seconds. On the other hand, experiment #8 shows that the oxygen concentration from $t = 10$ to $t = 220$ differ from sensor OT-09 to OT-10. During this time frame, the O_2 concentration remains below 13% for both sensors. After about $t = 220$, the oxygen concentration for sensors OT-09 and OT-10 is almost the same with a minimal difference. For experiment #1, the oxygen concentration remains below 6% at the top of the PCV containment building for the first 200 seconds. However, at the elevation of sensor OT-10, the concentration overcomes the 15% threshold in about 50 seconds from the beginning of the depressurization of the vessel.

The significant difference between these two experiments depicted in Figure 6.53 can be attributed to the density difference between both gases. The ventilation duct on the top (V12) likely vented not only air but also helium. When the depressurization of the vessel was complete, the gas dynamics in the PCV cavity section were less influenced by the forced convection as a result of the helium jet as time progressed. At some point, the gases switched from forced convection to buoyancy-driven motion, which resulted in helium moving upwards while air moved to lower sections. Since the ventilation gate was left open for 50 seconds, helium had enough time to escape through the ventilation duct. For the configuration where the ventilation duct was mounted at V11, the likelihood of helium escaping through the duct due to gravitational effects is low, which could potentially explain why the oxygen concentration at the top was considerably lower than in the other configuration.

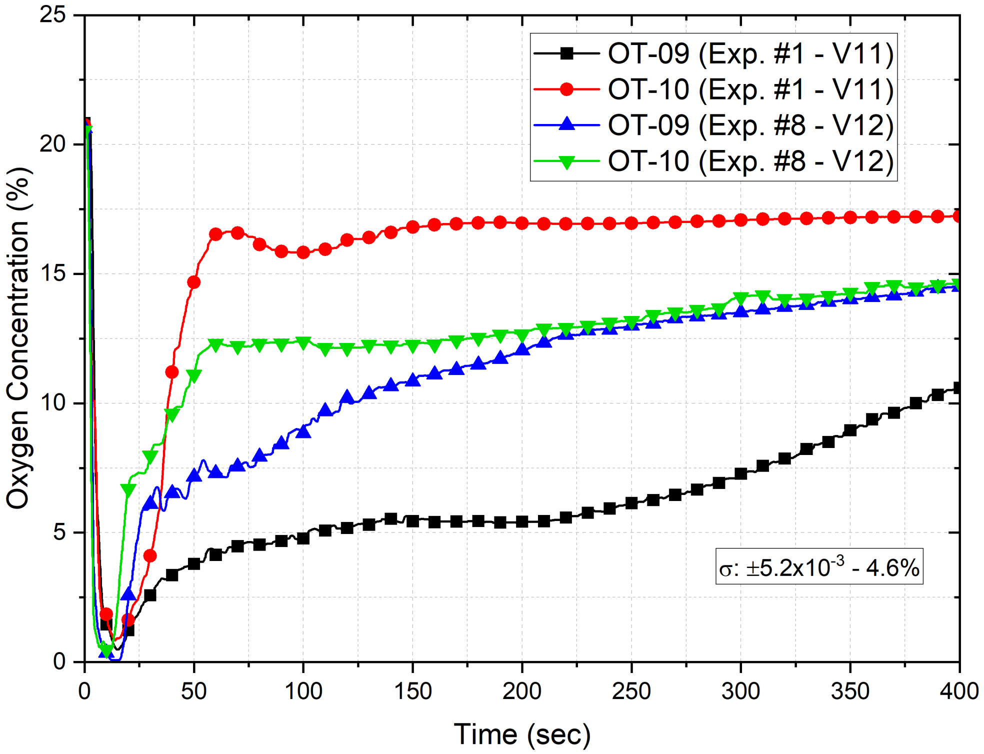

Figure 6.53: Oxygen measurements of the scaled-down PCV containment building for experiments #1 and #8.

Velocity measurements were captured at the ventilation duct for both experiments. Figure 6.54 depicts the comparison between both experiments. Measurements indicate that the velocities are higher when the ventilation duct is placed at a low elevation (V11) compared to the other configuration. The flow path from the vessel outlet to the ventilation duct is shorter with the configuration V11 compared to the configuration V12. While the difference is not significant, the momentum of the helium moving from the RPV to the PCV cavity section may be high enough that some of the helium could be vented during the early stages of the depressurization process. Unfortunately, it is impossible to determine whether air is the only gas vented with the current experimental configuration. However, this could be assessed with computational tools.

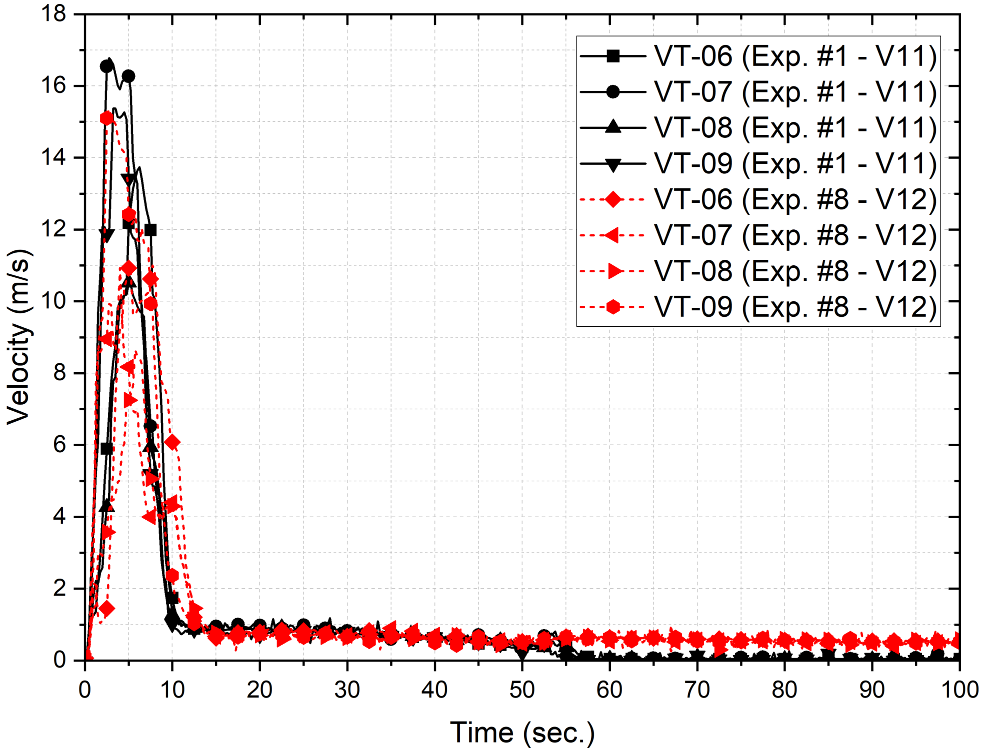

Figure 6.54: Velocity measurements at the ventilation duct of the scaled-down HTGR for experiments #1 and #8.

Another feature captured in Figure 6.54 is that after the ventilation duct was closed, the velocity for experiment #1 dropped to zero in about 5 seconds upon the closing of the ventilation. On the other hand, the velocity at the ventilation duct for experiment #8 did not drop to zero. The velocity dip for a brief moment, but it went back up. Thereafter, the velocity remained relatively constant afterward. Previous experiments addressed in previous subsections have shown that the gases in the upper sections remain turbulent longer than in the lower section. While this could justify why the velocity at the ventilation duct did not reach $0\,\mathrm{m\,s^{-1}}$, it is also essential to keep in mind that these velocities could also be the result of natural convection.

A similar comparison of the velocity in the RPV cavity was executed to look into potential signs of natural circulation. The left-hand side of Figure 6.55 shows an initial velocity peak in the first few seconds followed by a plateau. Interestingly, the velocities in the RPV cavity for experiment #8 did not drop to zero at any time. As shown on the right-hand side of Figure 6.55, the velocities dropped slowly as time progressed. The measurements from experiment #1 indicate that the velocity for sensor VT-02 dropped to zero at about the same time as the closing of the ventilation duct. At the time $t \approx 100$ seconds, the velocity increased again. This increase in velocity can be attributed to natural circulation.

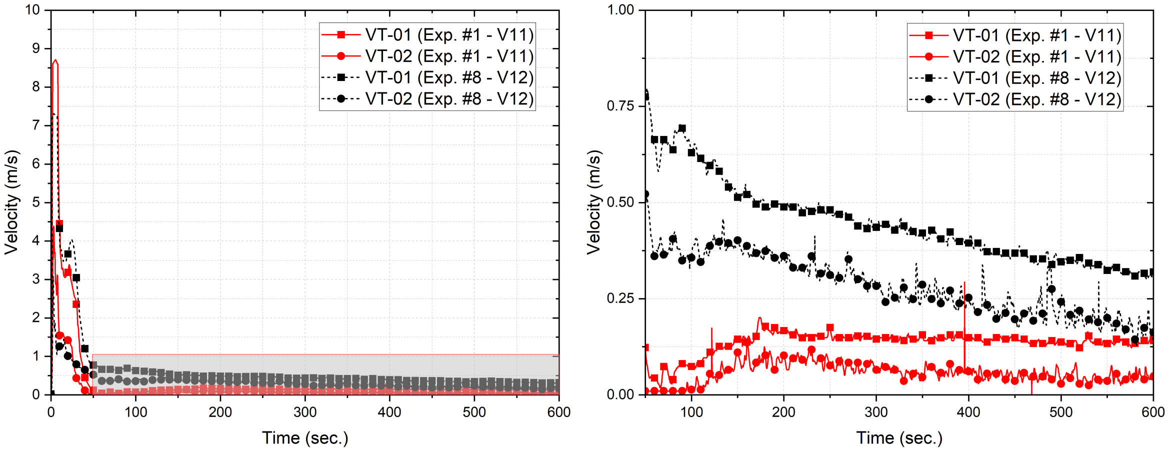

FIGURE 6.55: Velocity measurements in the RPV cavity of the scaled-down HTGR (left) for experiments #1 and #8 with an enlargement (right) of the velocities right after the ventilation duct gate was shut.

Temperature measurements were captured at multiple points in the scaled-down facility. In a similar fashion as the previous experiments, only the temperature measurements at the reactor cavity are plotted and shown in this section. The temperature measurement plots for experiments #1 and #8 are shown in Figures 6.56, 6.57 and 6.58.

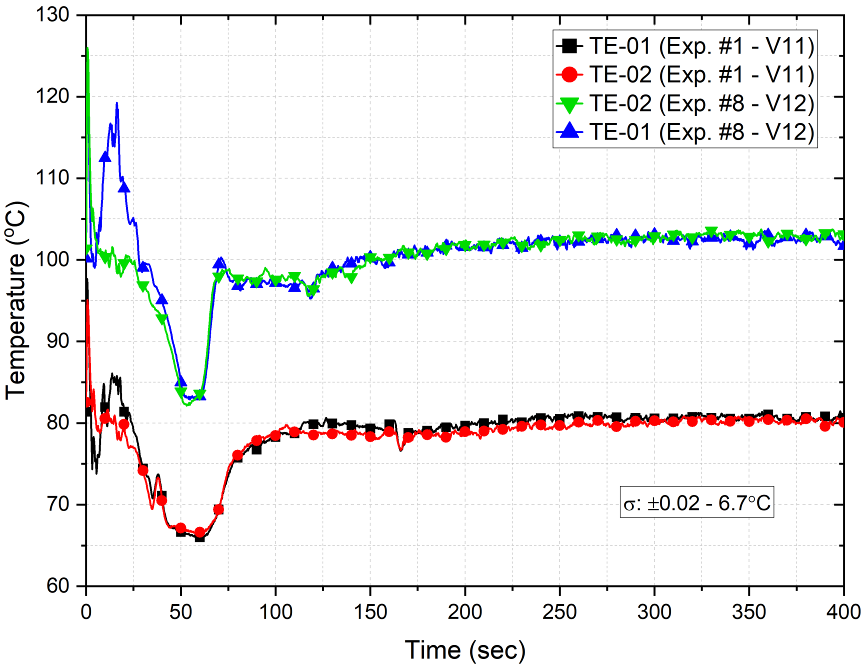

Figure 6.56: Temperature measurements in the RPV cavity from sensors TE-01 and TE-02 of experiments #1 and #8.

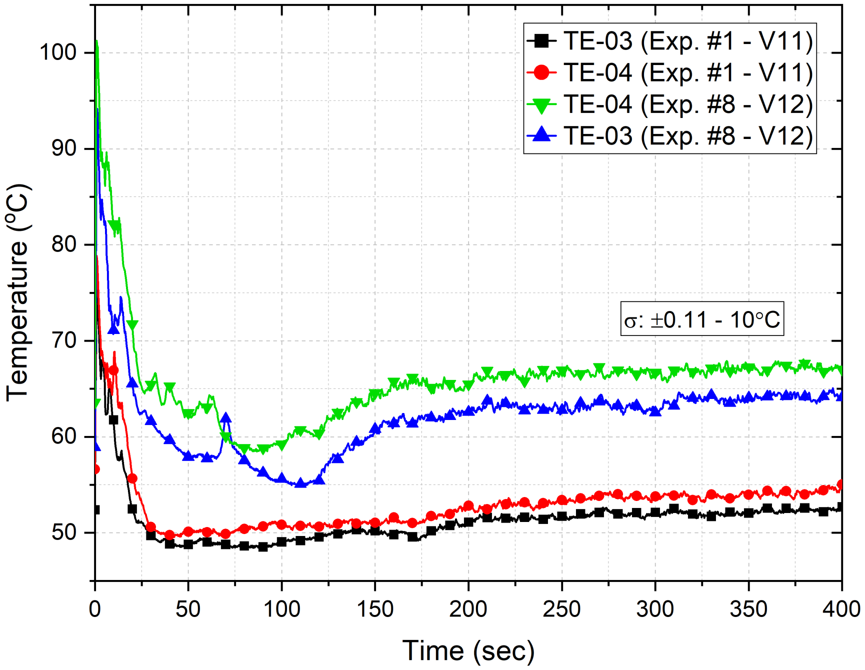

Figure 6.57: Temperature measurements in the RPV cavity from sensors TE-03 and TE-04 of experiments #1 and #8.

The temperature measurements for experiment #8 are relatively higher than experiment #1 for all sensors. These higher temperature measurements are attributed

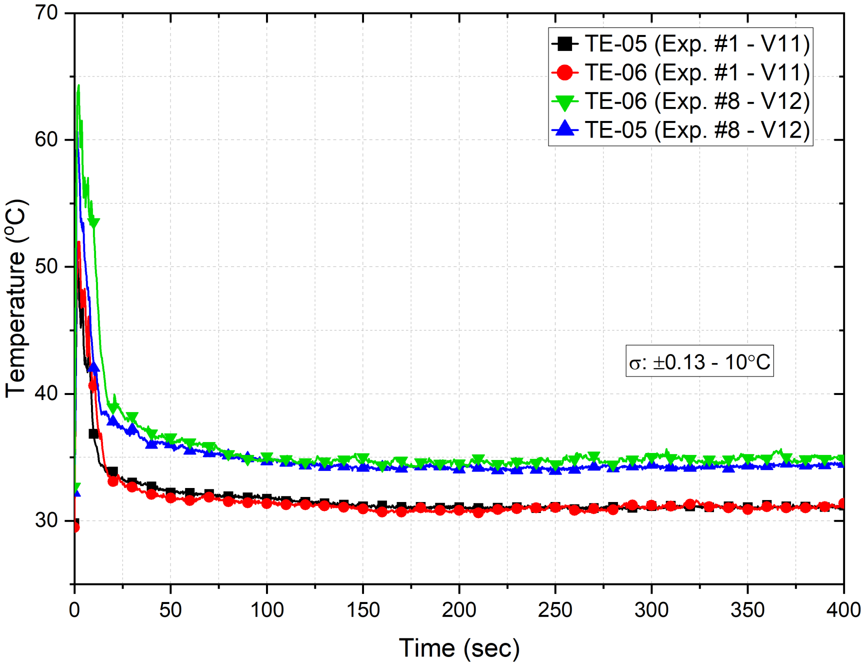

Figure 6.58: Temperature measurements in the RPV cavity from sensors TE-05 and TE-06 of experiments #1 and #8.

to the higher voltage applied to the electric heaters to reach the desired pressure level. This could have led to higher temperature measurements across the entire experimental facility.

6.6 ANALYSIS AND DISCUSSION

6.6.1 *Oxygen Concentration at the Break Location*

The above comparison analyses provided information about the changes in temperature, pressure, velocity, and oxygen concentration over time during and after the depressurization of a scaled-down pressure vessel. The time of active ventilation analysis provided insight into the timing that the ventilation system should be operational to prevent instrumentation failure. Also, it provided insights into the importance of the time of active ventilation. This study evaluates five times where the ventilation duct remains open for 12, 22, 50, 65 seconds, and indefinitely.

Experimental results indicate that closing the ventilation gate after 22 seconds significantly reduces the oxygen concentration. To reiterate, a time-scale of 22 seconds for active ventilation was chosen because the depressurization of the vessel was completed in about 12 seconds. Based on the timing required to complete the depressurization, evaluating the system's behavior was deemed necessary when the ventilation time scale was increased from about 12 seconds to 22 seconds. Unfortunately, the zirconium dioxide oxygen sensors could not operate for a long time in an environment with deficient O_2 concentration. The oxygen sensors of the experiment with a 12-second active ventilation time failed in about 100 seconds, in some instances sooner, from the initial time of the depressurization process. Thus, a comparison between the experiment with a total active ventilation time of 12 and the other times could not be completed in this study properly. While keeping in mind the failure of the O_2 sensors for the 12 seconds of active ventilation time experiment, a comparison analysis was carried out to determine the oxygen concentration near the break location. The comparison of the different oxygen concentrations is shown in Figures 6.59, 6.60, and 6.61. It is important to note that the failed sensors were discarded from the bar plots.

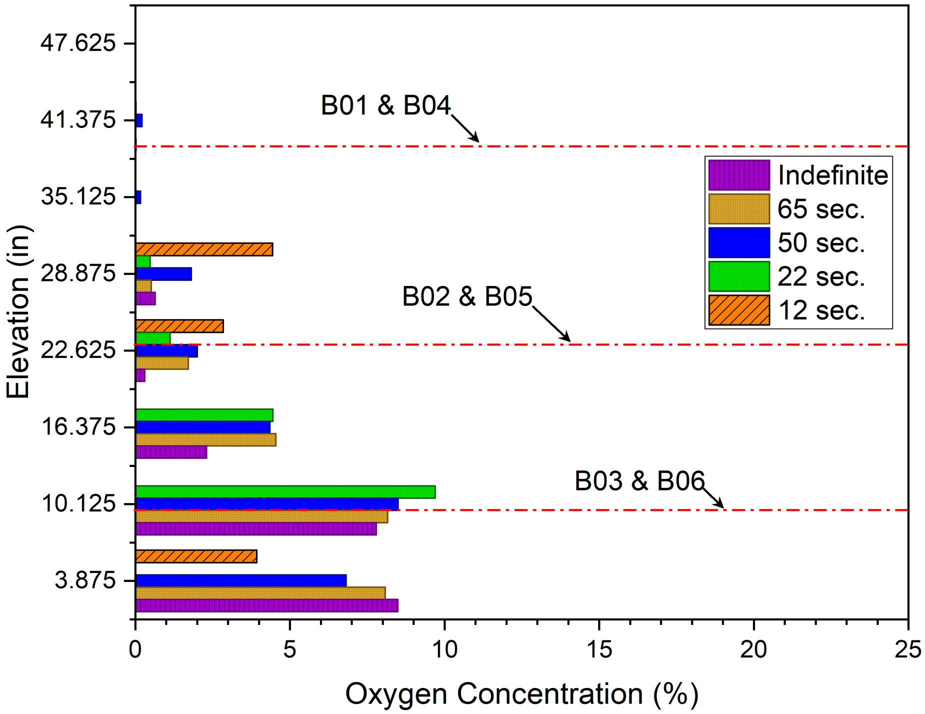

FIGURE 6.59: Oxygen concentration for varying ventilation times at different elevations at $t = 50$ seconds.

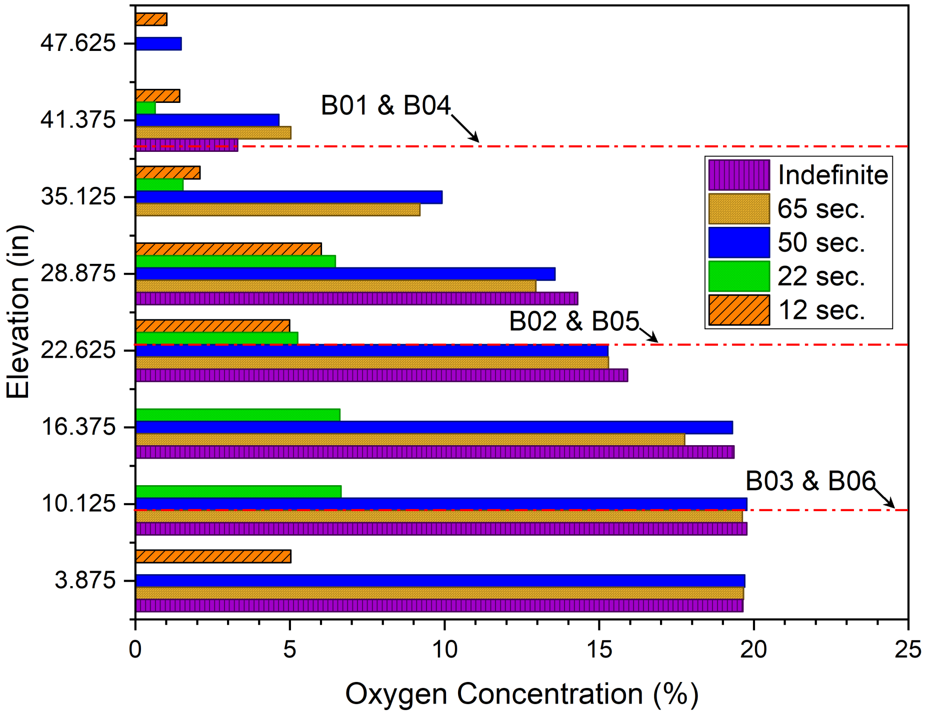

FIGURE 6.60: Oxygen concentration for varying ventilation times at different elevations at $t = 75$ seconds.

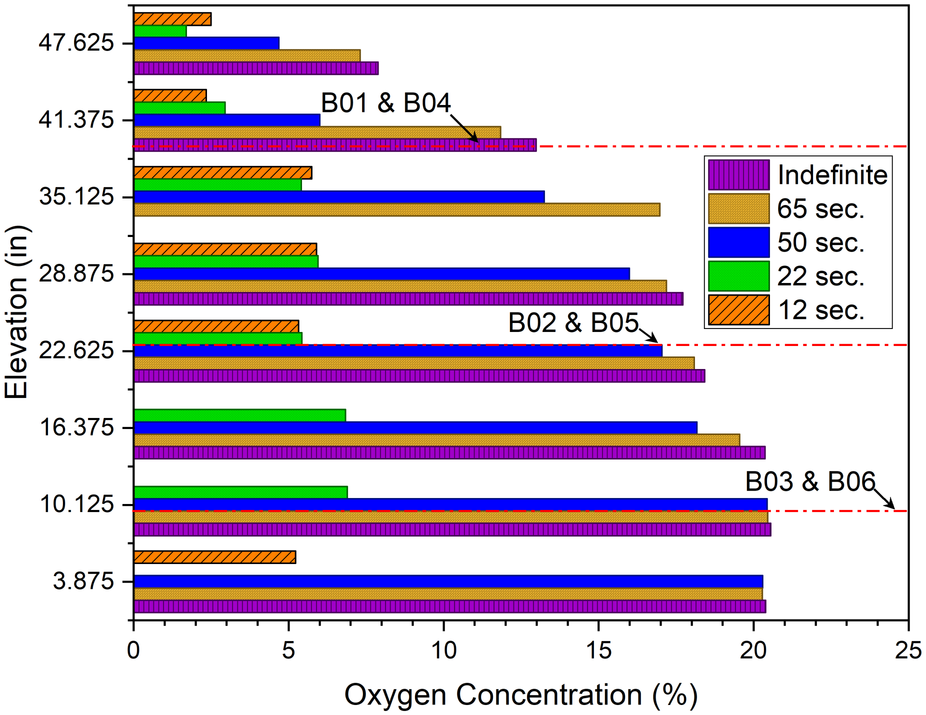

FIGURE 6.61: Oxygen concentration for varying ventilation times at different elevations at $t = 100$ seconds.

The three red lines labeled on the bar plots indicate the elevation of the six breaks on the scaled-down pressure vessel. Experimental data shows that an active ventilation time of 22 seconds yields better results than the other experiments, except for experiment #12, which also yielded positive results. In the early stages of this study, it was decided to run experiments with an active ventilation time of 22 seconds as the baseline. However, the oxygen sensors failed in one of the experiments with a small break size. A small break results in a prolonged helium discharge into the cavity section. As a result of the lengthened depressurization, the air in the reactor cavity was displaced quite well, preventing re-ingress. The extended exposure of the O_2 sensors in a helium environment combined with the closing of the active ventilation gate resulted in the failure of the O_2 sensors. Thus, the timing of active ventilation was re-evaluated, and it was deemed necessary to increase the time from 22 seconds to 50 seconds, so a comparison of smaller break sizes could be completed without having issues with the O_2 sensors.

The oxygen concentration near the break location B01 and B04 at $t = 50$ seconds is less than 0.3% for all scenarios and less than 10% near the break location B03 and B06. At $t = 75$ seconds, the O_2 concentration near B01 and B04 is less than 5%, and less than 20% near B03 and B06. At 100 seconds from the beginning of the depressurization, the oxygen concentration near B01 and B04 significantly differs from experiment to experiment. The oxygen concentration increases as the active ventilation time is delayed. For an active ventilation time of 12 and 22 seconds, the O_2 concentration remains below 3% near B01 and B04, whereas for an active ventilation time of 50, the concentration was about 6%. The oxygen concentration for the other two experiments was about 12 and 13% for the 65 seconds and indefinite times of active ventilation, respectively.

The sensitivity study that looks into the effects of the gas dynamics of the cavity section for varying break sizes sheds light on what could potentially happen if the system experiences relatively small and large breaks. An expected behavior corroborated with the experimental data collected in this study is that the depressurization process is elongated as the break size is reduced. A phenomenon that is worth noting is that more air is vented for small breaks (e.g., $D = 125$ in.) compared to relatively large breaks (e.g., $D = 0.410$ in.). Oxygen measurements indicate that the smaller the break size, the lower the oxygen concentration in the reactor cavity. The vertical oxygen concentration and temperature stratification for different break sizes are plotted and shown in Figure 6.62.

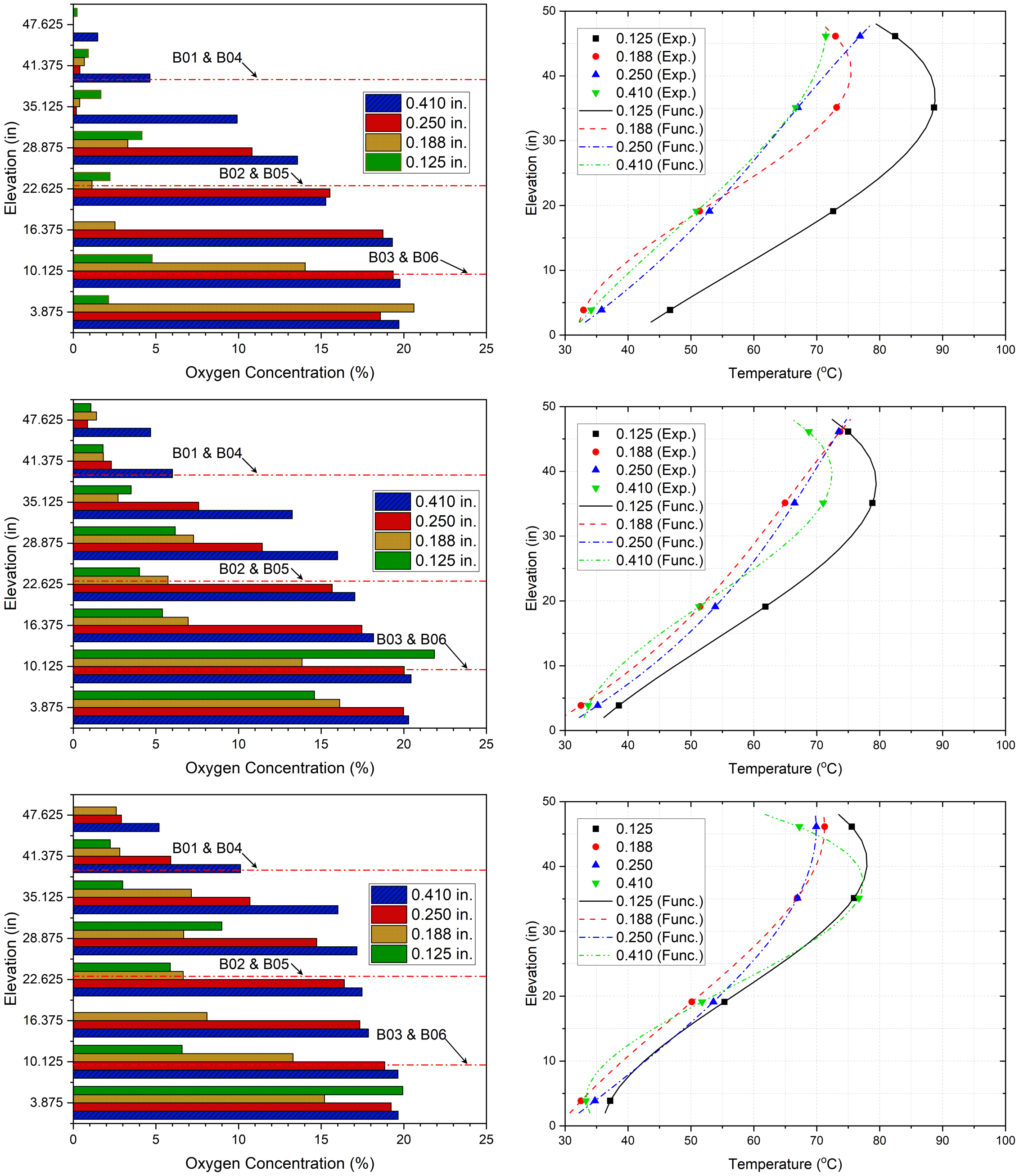

FIGURE 6.62: Oxygen concentration (left) and temperature (right) measurements at different elevations in the reactor cavity at $t = 50$ sec. (top), 75 sec. (middle), and 100 sec. (bottom) for different break sizes.

The temperature plots shown on the right-hand side of Figure 6.62 were obtained by averaging the temperature measurements obtained from the back of the reactor cavity section. Thereafter, a polynomial function of third order was developed to predict the temperature of the reactor cavity as a function of height. Figure 6.63 shows a schematic of the position of the thermocouples used to collect the temperature measurements displayed on the right-hand side of Figure 6.62. The colors indicate which temperature measurements were averaged. Table 6.5 summarizes the correlations developed to predict the temperature stratification in the reactor cavity. The coefficient of determination, R squared (R^2), for the third order polynomial equations is 1.0.

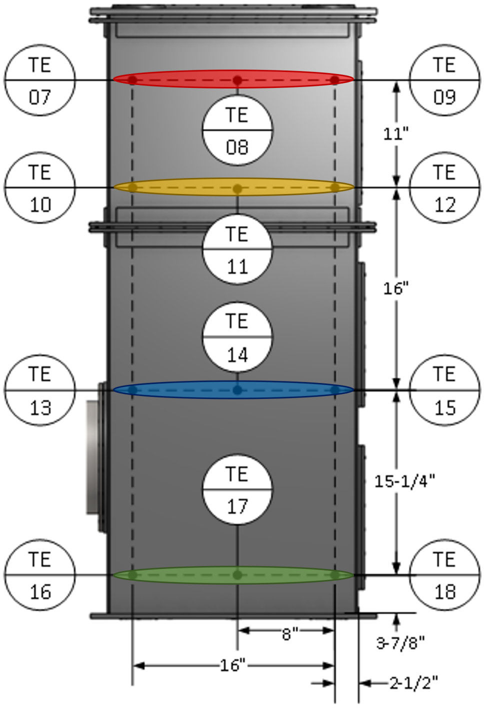

FIGURE 6.63: Schematic of the back view of the RPV containment building indicating what thermocouple measurements were averaged.

Table 6.5: Temperature correlations for different break sizes as a function of height at different times.

Break	**Correlation**
50 seconds	
0.125"	$T(y) = -8.40308x10^{-4}y^3 + 2.646654x10^{-2}y^2 + 1.474118y + 40.62115$
0.188"	$T(y) = -1.32212x10^{-3}y^3 + 8.171668x10^{-2}y^2 - 0.06850536y + 32.04839$
0.250"	$T(y) = 2.02064x10^{-4}y^3 - 1.956449x10^{-2}y^2 + 1.481566y + 30.34686$
0.410"	$T(y) = -3.95215x10^{-4}y^3 + 1.929912x10^{-2}y^2 + 0.8349685y + 30.64556$
75 seconds	
0.125"	$T(y) = -8.870840x10^{-4}y^3 + 3.668633x10^{-2}y^2 + 1.087079y + 33.84275$
0.188"	$T(y) = 2.619643x10^{-4}y^3 - 2.800417x10^{-2}y^2 + 1.766753y + 26.09686$
0.250"	$T(y) = 2.026146x10^{-4}y^3 - 2.579327x10^{-2}y^2 + 1.726141y + 28.87994$
0.410"	$T(y) = -1.320138x10^{-3}y^3 + 7.920026x10^{-2}y^2 - 0.06636044y + 32.84254$
100 seconds	
0.125"	$T(y) = -1.228393x10^{-3}y^3 + 7.447907x10^{-2}y^2 + 0.03649986y + 35.97868$
0.188"	$T(y) = -4.850367x10^{-4}y^3 + 2.469626x10^{-2}y^2 + 0.8077598y + 29.06693$
0.250"	$T(y) = -1.901337x10^{-4}y^3 - 1.759017x10^{-3}y^2 + 1.361958y + 29.50639$
0.410"	$T(y) = -2.383857x10^{-3}y^3 + 1.496698x10^{-1}y^2 - 1.147013y + 35.64733$

The information presented in Figure 6.62 and Table 6.5 could potentially be used to adjust the initial boundary conditions for simulations that look into analyzing the air ingress in HTGR during a LOCA event.

The experimental data collected from experiments that look into the difference between different break locations were compared for different case scenarios. The comparison analysis shows that the temperatures were higher in the first few seconds subsequent to the beginning of the depressurization process when the break is located in the upper sections. In general, a distinguishable difference that can be mainly attributed to the location or orientation of the break could not be pinpointed. The plots indicated that despite the break location and orientation, the gas mixture takes longer to reach steady-state conditions in upper sections than in lower ones, as shown in Figure 6.42. The vertical oxygen concentration and temperature were collected and plotted in Figure 6.64 for three different times, $t = 50$, 75, and 100 seconds.

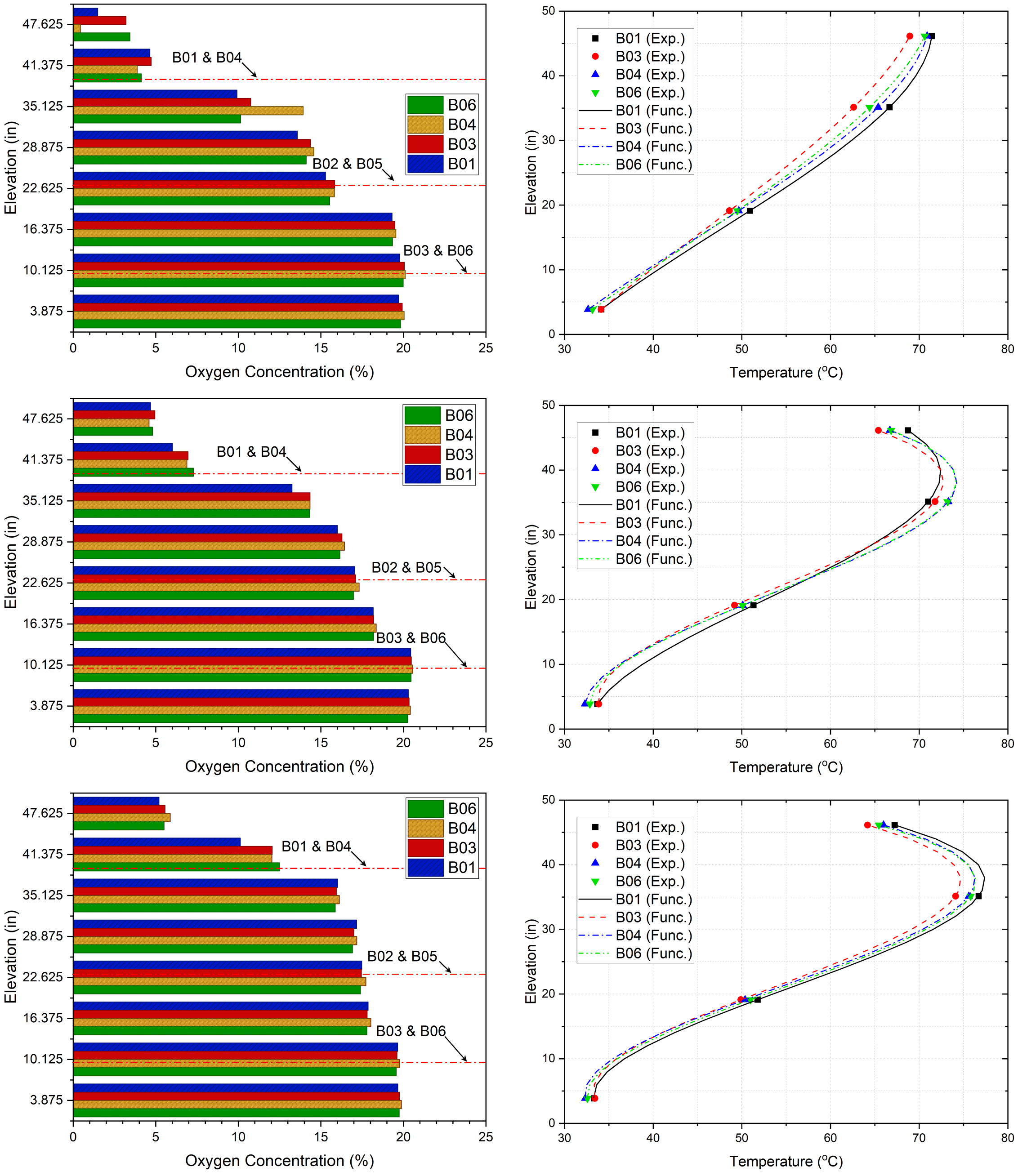

FIGURE 6.64: Oxygen concentration (left) and temperature (right) measurements at different elevations in the reactor cavity at $t = 50$ sec. (top), 75 sec. (middle), and 100 sec. (bottom) for different break locations.

Oxygen measurements on the left-hand side of Figure 6.64 show small differences for the four different break locations for the three different times. Small variations can be observed at the top of the RPV cavity section at $t = 50$ seconds. The temperature stratification plots of the cavity of the RPV show small temperature differences. Third-order polynomials were developed and plotted to compute the temperature stratification on the right-hand side of Figure 6.64. These correlations are summarized in Table 6.6.

Table 6.6: Temperature correlations for different break locations as a function of height at different times.

Location	**Correlation**
50 seconds	
B01	$T(y) = -3.952145x10^{-4}y^3 + 1.929912x10^{-2}y^2 + 0.8349685y + 30.64556$
B03	$T(y) = -2.074949x10^{-4}y^3 + 9.730605x10^{-3}y^2 + 0.8189954y + 30.83381$
B04	$T(y) = -3.224317x10^{-4}y^3 + 1.456449x10^{-2}y^2 + 0.9253267y + 28.87612$
B06	$T(y) = -2.172251x10^{-4}y^3 + 8.222059x10^{-3}y^2 + 0.9802846y + 29.23837$
75 seconds	
B01	$T(y) = -1.320138x10^{-3}y^3 + 0.07920026y^2 - 6.636044x10^{-2}y + 32.84254$
B03	$T(y) = -2.057356x10^{-3}y^3 + 0.1326544y^2 - 1.110455y + 36.28861$
B04	$T(y) = -2.010103x10^{-3}y^3 + 0.1258720y^2 - 0.8138697y + 33.69670$
B06	$T(y) = -2.011362x10^{-3}y^3 + 0.1269764y^2 - 0.8756290y + 34.45802$
100 seconds	
B01	$T(y) = -2.383857x10^{-3}y^3 + 0.1496698y^2 - 1.147013y + 35.64733$
B03	$T(y) = -2.448309x10^{-3}y^3 + 0.1562328y^2 - 1.400983y + 36.66432$
B04	$T(y) = -2.450159x10^{-3}y^3 + 0.1550719y^2 - 1.270127y + 35.07595$
B06	$T(y) = -2.446519x10^{-3}y^3 + 0.1532728y^2 - 1.206570y + 35.09994$

Generally, the experiments covered in this study were executed with a configuration that vents the cavity through the lower section of the PCV containment building. However, the location of the ventilation system cannot be neglected in this study, given that buoyancy forces play a crucial role in the gas dynamics of the gas mixture. The elevation of the ventilation system in the short and long term directly influences the system's efficiency in venting air. Hence, experiment #8 has the same configuration as experiment #1, except for the location of the ventilation duct. Section 6.5 compares these two experimental setups, where one evaluates the system's performance when the ventilation system is mounted in a high elevation on the PCV containment building (experiment #8). The other evaluates the system's behavior when the ventilation system is located at a lower elevation (experiment #1). Experimental results indicate that air is better vented when the ventilation system is located in the upper section than in the lower, as shown in Figures 6.51

through 6.52. All these plots show that the oxygen concentration is lower if the ventilation system is placed at a high elevation, except for the right-hand side of Figure 6.52. Sensors OT-07 and OT-08, unfortunately, failed within a few seconds post the beginning of the depressurization of the vessel. In the cavity section where the scaled-down PCV is located, the oxygen concentration difference at the elevation of the zirconium dioxide oxygen sensors OT-09 and OT-10 is considerably different. In the case of experiment #8, the concentration difference between these two oxygen sensors is noticeable subsequent to the beginning of the depressurization. Thereafter, this difference shrinks until about $t = 200$ seconds. The concentration difference is considerably small after 200 seconds. Helium is potentially discharged into the RB cavity during the depressurization process. Gases move from the RB to PCV cavity through the axial cross-vessel duct. In this cavity region, the gas dynamics of the mixture are predominantly dominated by the buoyancy forces due to the molecular weight of helium and air and the forced convection due to the helium jet generated by the break. Helium will tend to move to high elevations, whereas air will move to low sections. More helium will be vented if the ventilation system is placed at a high elevation.

On the other hand, the placement of the ventilation system at a lower elevation retains most of the helium within the system. Thus, one can conclude that the placement of the ventilation duct in the upper section of the PCV containment building will result in lower oxygen concentration in the RB cavity, but the higher concentration in the PCV cavity section. Inversely, a ventilation system placed in the lower section of the PCV containment building will result in higher oxygen concentration in the RB cavity but lower concentration in the PCV cavity region.

The temperature stratification and oxygen concentration in the vertical direction of the RPV cavity are plotted in Figure 6.65.

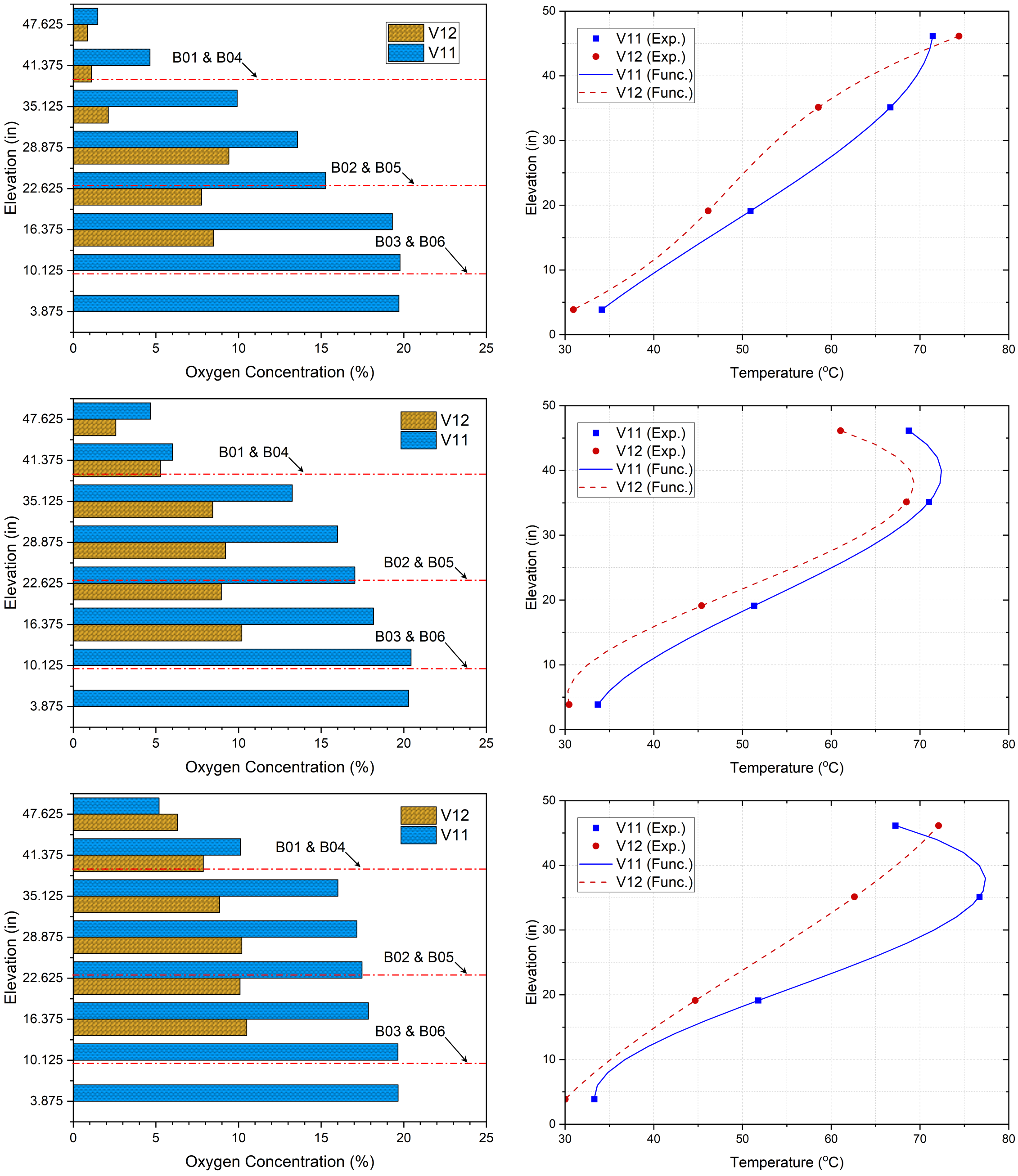

Figure 6.65: Oxygen concentration (left) and temperature (right) measurements at different elevations in the reactor cavity at $t = 50$ sec. (top), 75 sec. (middle), and 100 sec. (bottom) for different ventilation locations.

The correlations developed to predict the changes of temperature in the reactor cavity as a function of elevation for times $t = 50, 75$, and 100 seconds are summarized in Table 6.7.

Table 6.7: Temperature correlations for different ventilation locations for three different times.

Location	Correlation
50 seconds	
V11	$T(y) = -3.952145x10^{-4}y^3 + 1.929912x10^{-2}y^2 + 0.8349685y + 30.64556$
V12	$T(y) = 7.487582x10^{-4}y^3 - 5.053331x10^{-2}y^2 + 1.816880y + 24.62348$
75 seconds	
V11	$T(y) = -1.320138x10^{-3}y^3 + 7.920026x10^{-2}y^2 - 0.06636044y + 32.84254$
V12	$T(y) = -2.208181x10^{-3}y^3 + 0.1431895y^2 - 1.309747y + 33.51333$
100 seconds	
V11	$T(y) = -2.383857x10^{-3}y^3 + 0.1496698y^2 - 1.147013y + 35.64733$
V12	$T(y) = -3.495949x10^{-4}y^3 + 2.545041x10^{-2}y^2 + 0.5347945y + 27.58948$

6.6.2 *Lock-exchange phenomena*

The experiments covered in this study were executed with the heaters turned on throughout the entire experiment. Following the depressurization, natural circulation was established over time. The gas mixture nearby the scaled-down pressure vessel is heated through the vessel's walls. Since the system is not insulated, the hot gases will cool down through the walls of the RB. Because the pressure vessel is the only section heated, the walls surrounding the vessel are relatively warmer than the walls surrounding the PCV. Hence, the helium and air will move from the RPV cavity section towards the PCV cavity through the axial cross-vessel duct. The gas mixture then moves from the axial cross-vessel duct to the upper section of the cavity section due to density difference. As this gas mixture cools down, the gases move downwards, maxing their way towards the bottom of the cavity section of the RPV, where it is heated gain.

To further shed light on the gas dynamics of an HTGR cavity during a LOCA event, instrumentation was mounted at the top and bottom of the axial cross-vessel duct to measure the velocity and temperature of the gases moving from one cavity section to the other. The flow area of the hot and cold gas mixture is computed using the experimental data gathered, and theoretical correlations developed and used to understand the lock-exchange flow phenomena. In the past, the lock-exchange flow has been studied using two fluids of different densities separated by a vertical partition in a horizontal channel, as shown in Figure 6.66. When the partition between both fluids is removed, the fluid with light density starts propagating at a constant speed along the upper section of the horizontal channel. The heavy fluid also propagates along the lower section of the horizontal channel (Rotunno *et al.*, 2011; Birman *et al.*, 2005; Lowe *et al.*, 2005).

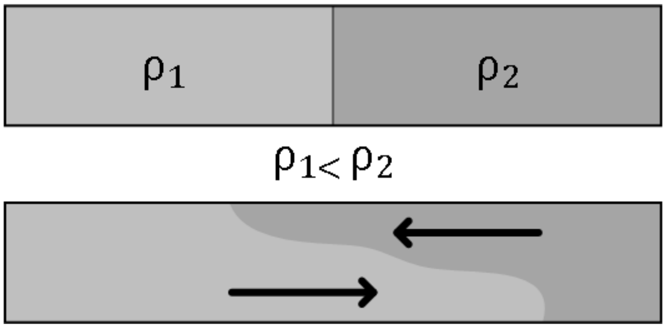

FIGURE 6.66: Schematic of a horizontal channel with two fluids of different densities separated by a vertical partition (top). Flow propagation of the light and heavy densities (bottom) after removing the vertical partition.

While this configuration seems quite simple, the physics behind it is complex (Rotunno *et al.*, 2011) and some of the flow phenomena still defy definite theoretical explanation (Lowe *et al.*, 2005).

A journal paper published by Lowe *et al.* (2005) analyzes the experimental results of a non-Boussinesq lock-exchange problem. These experimental results were compared against a theoretical approach that predicts the height of the heavy current front. Figure 6.67 shows the comparison between the experimental and theoretical results covered in Lowe *et al.* (2005) study.

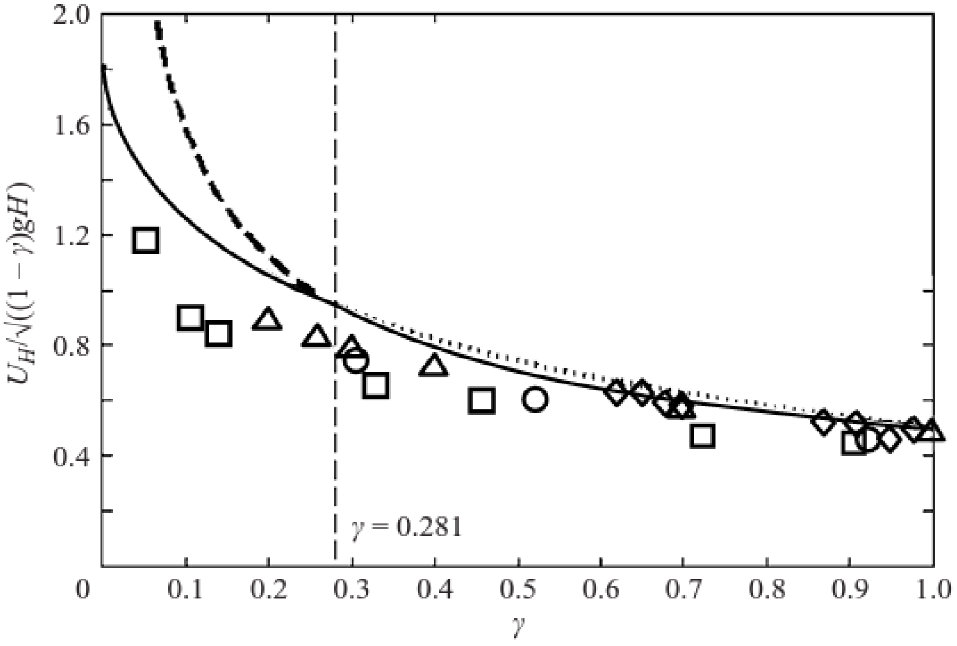

Figure 6.67: Comparison between experimental and theoretical front speed as a function of the density ratio of both fluids. The theoretical results are plotted as solid, dashed, and dotted lines, while the experimental results are plotted as symbols (Lowe *et al.*, 2005).

In Figure 6.67, the Greek letter gamma, γ, is used to represent the ratio of the lighter density, ρ_2, over the heavier, ρ_1. U_H and H represent the speed of the heavy current and the total height of the horizontal channel, respectively. Figure 6.67 indicates that as the density ratio of the heavy and light currents equals one, the velocity of the heavy current decreases. Using the Benjamin's energy-conserving gravity current theory, the velocity of the heavy current for different density ratios is computed using the following relationships (Benjamin, 1968):

for $0.281 < \gamma \leq 1$:

$$U_H = \frac{1}{2}\sqrt{\frac{(1-\gamma)gH}{\gamma}}, \tag{6.2}$$

for $0 < \gamma \leq 0.281$:

$$U_H = \sqrt{(1-\gamma)gH}\left[\frac{h_H}{\gamma H}\left(2 - \frac{h_H}{H}\right)\frac{1 - h_H/H}{1 + h_H/H}\right]^{1/2}, \tag{6.3}$$

where h_H is the height of the heavy current. To estimate the flow area of the hot and cold gas mixtures in the scaled-down HTGR, it is assumed that when natural circulation is established, the containment building of the scaled-down experimental facility is air-tight sealed, and no accumulation of mass takes place in either cavity section. Based on these assumptions, one can assume the following:

$$\frac{\dot{m}_L}{\dot{m}_H} = 1 = \frac{(\rho AU)_L}{(\rho AU)_H} = \gamma \frac{(AU)_L}{(AU)_H}. \tag{6.4}$$

From the above equation, the densities and areas are not known. The velocities, however, can be obtained from the velocity measurements obtained in this study. The density ratio can be identified from Figure 6.67. When the density ratio is plugged into either Equation 6.2 or 6.3, the computed velocity should be equal to the measured velocity. In Figure 6.47, the average velocity for the the experiment #1 is about $0.3137\,\mathrm{m\,s^{-1}}$ for the heavy current (cold gas mixture) and about $0.0407\,\mathrm{m\,s^{-1}}$ for the light current (hot gas mixture). Based on this experimental data, it is estimated that the density ratio should be about 0.8506, as shown in Figure 6.68.

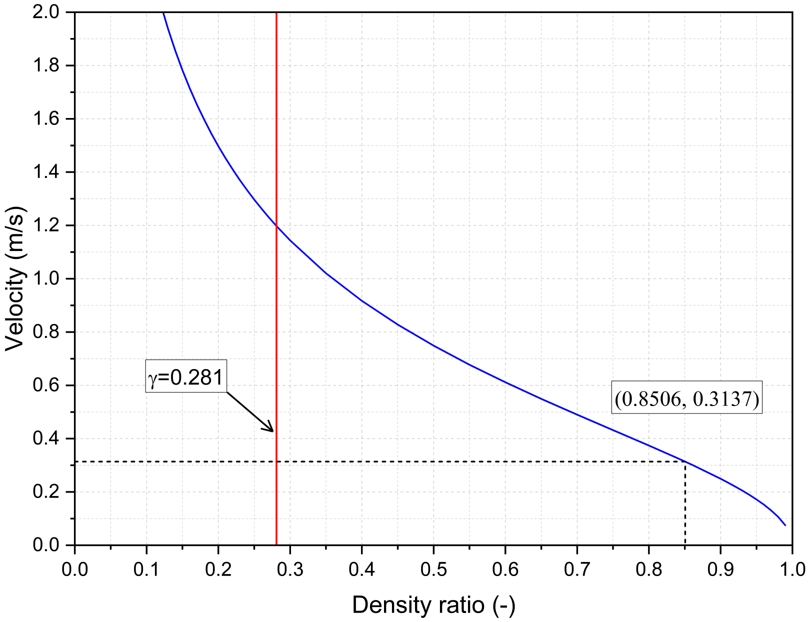

FIGURE 6.68: Heavy current height ratio with respect to the total height of the axial cross-vessel duct inner diameter as a function of density ratio. Dashed black lines indicate the density ratio that should yield the measured velocity.

The area ratio from Equation 6.4 can be computed from knowing the velocities and density ratio, as shown below:

$$\frac{A_H}{A_L} = \gamma \frac{U_L}{U_H} = 0.8506 \frac{0.0407}{0.3137} = 0.2668. \tag{6.5}$$

If the cross-sectional area of the the cross-vessel duct is 63.6173 $in.^2$, then one can compute for the heights and areas of both the heavy and light currents. Table 6.8 summarizes the results obtained in this analysis.

TABLE 6.8: Results from lock-exchange analysis of experiment #1.

Description	Temperature	Velocity	height	Area
Heavy (hot) current	44.8445^{o}C	0.0407m/s	1.4023in.	6.3229in.^{2}
Light (cold) current	26.2676^{o}C	0.3137m/s	7.5977in.	57.2943in.^{2}

Based on the information presented above, one can assume that the flow area of the hot gases at the top is about nine times larger than the cold gases at the bottom. Figure 6.69 visually represents the flow direction of the gases passing through the axial cross-vessel duct.

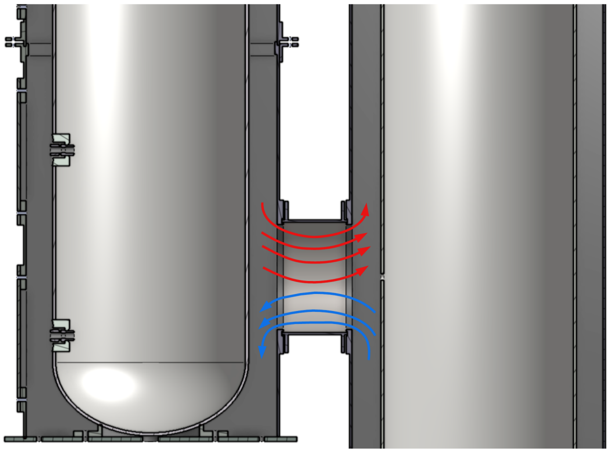

FIGURE 6.69: Schematic of the scaled-down HTGR axial cross-vessel duct indicating the flow direction of the hot and cold gases.

CHAPTER 7

CONCLUSION

The present study aims to answer a particular question regarding the oxygen concentration in the reactor cavity, particularly the concentration at the break location. To answer the question in consideration and further shed light on the VLPC cavity gas dynamics and how to optimize the system's ventilation, a $1/20^{th}$ scaled-down experimental facility was designed and built at the University of Idaho - Idaho Falls campus. The series of experiments summarized in Section 5.2 aim to provide a better understanding of the gas-mixing behavior of a HTGR during a LOCA event. These tests evaluate different configurations to determine the system's behavior involving different active ventilation time scales, break sizes and locations, and the placement of the ventilation system.

The time of active ventilation was evaluated to identify the time scale that would allow for better ventilation of the cavity section. Experimental results indicate that active ventilation of 22 seconds, ten seconds after fully depressurizing the vessel, yields positive results. The system was tested with an active ventilation time of 12 seconds, but the oxygen sensors failed due to prolonged exposure to an atmosphere with low oxygen concentration. After testing smaller break sizes, the oxygen sensors started failing. Therefore, to evaluate different configurations while keeping a consistent timing for the closing of the ventilation duct gate, it was decided to allow the system to vent for a total of 50 seconds following the beginning of the depressurization process. Air re-ingress from the ventilation system during this time frame is believed. Nonetheless, the probability of drifting the oxygen sensors decreased significantly.

The system was also evaluated with different break sizes, including outlets with an outer diameter of 0.410, 0.250, 0.188, and 0.125 inches. Results indicate that the smaller the break size, the longer it takes to depressurize the vessel. The elongation of the depressurization process led the system to better vent air out of the cavity section. Additionally, the orientation and elevation of the break were evaluated as well. Results showed that the different location of the breaks has little influence on the oxygen concentration in the cavity. However, it did influence the velocities of the gases vented. A break in a lower section of the pressure vessel results in higher velocities at the ventilation duct.

The ventilation duct placement was also tested as part of the last sensitivity study. The comparison analysis evaluates the system's performance when the ventilation duct is placed at a high and low elevation in the containment building of the PCV. Interestingly, the oxygen concentration is higher and lower at the cavity section of the RPV and PCV, respectively, when the ventilation duct is placed at a low elevation in the containment building of the PCV. Conversely, when the ventilation duct is mounted at a high elevation, the oxygen concentration in the cavity section of the RPV is lower. However, it is higher at the cavity section of the PCV. This behavior is mainly attributed to buoyancy effects due to the significant molecular mass difference between air and helium.

In the analysis subsection of the experimental results, a comparison of the oxygen concentration and temperature stratification was executed for different experiments. In this comparison analysis, the oxygen concentration for three times, $t = 50$, 75, and 100 seconds, was plotted to better indicate the oxygen concentration at different heights and times. In addition, this information was complemented with temperature measurements. The measurements captured from the thermocouples mounted on the back of the containment building of the RPV, $TE - 07$ through $TE - 18$, were used to develop a third-order polynomial correlation to predict the temperature stratification of the RPV cavity section. With the oxygen concentration and temperature correlations, the density of the cavity section can be used to better choose the initial conditions of the cavity during the ingress of air into the HPB.

7.1 LIMITATIONS AND FUTURE WORK

As mentioned in some sections of this work, the chosen zirconium dioxide oxygen sensors were one of the limiting factors that prevented us from running experiments at higher pressures and temperatures. Also, The time of active ventilation for the scaled-down experimental facility was heavily influenced by the performance of the oxygen sensors. Their inability to properly operate in environments with little oxygen for prolonged time lapses limited our ability to close the ventilation gate sooner to avoid air re-ingress. To further better characterize the mixing of air and helium in the cavity of the VLPC, replacing or modifying the O_2 sampling method is recommended.

While this study evaluated multiple configurations where a break takes place on the RPV, it is essential to evaluate the system's behavior when a break takes place on the axial cross-vessel and the PCV. For the axial cross-vessel, it is recommended to look into the oxygen concentration in the VLPC when a break of different sizes and angles take place. Additionally, looking into the time-scale of air ingress into the HPB is recommended. The experiments executed in this study measured the O_2 concentration in the cavity section only. However, it is also essential to look into the time scale at which oxygen makes its way towards the inside of the HPB. It is recommended that UI-IF evaluates the probability of installing oxygen sensors inside the scaled-down pressure vessel.

Finally, evaluating other potential ventilation system designs is recommended, including using more than one ventilation duct. This study has contributed to the body of knowledge by evaluating the time of active ventilation and ventilation placement. However, this study can be complemented if different geometries and the number of ventilation ducts are evaluated. While this can be executed experimentally, it could be executed using computational tools such as CFD and Multi-physics Object-Oriented Simulation Environment (MOOSE).

Bibliography

Alshehri S.M., Said I.A., and Usman S. 2021. A review and safety aspects of modular high-temperature gas-cooled reactors. International Journal of Energy Research 45:11479–11492.

Arcilesi D.J., Ham T.K., Sun X., Christensen R.N., and Oh C. 2011. Development of scaling analysis for air ingress experiments for a vhtr. Transactions 105:987–989.

Arcilesi Jr D.J. 2018. Experimental Verification of the Initial Stages of an HTGR Double-ended Guillotine Break. Ph.D. thesis, The Ohio State University.

Arcilesi Jr D.J., Ham T.K., Kim I.H., Sun X., Christensen R.N., and Oh C.H. 2015. Scaling and design analyses of a scaled-down, high-temperature test facility for experimental investigation of the initial stages of a vhtr air-ingress accident. Nuclear Engineering and Design 288:141–162.

Atomics, Gerneral. 2014. General atomics' prismatic modular high temperature gas cooled reactor. International Atomic Energy Agency, nd Web 7.

Balderrama Prieto S.A., Christensen R.N., and Sabharwall P. 2021. Numerical analysis of helium-air concentration of a scaled-down htgr system. *In* 19th International Topical Meeting on Nuclear Reactor Thermal Hydraulics (NURETH-19).

Ball S., Richards M., and Shepelev S. 2008. Sensitivity studies of air ingress accidents in modular htgrs. Nuclear Engineering and Design 238:2935–2942.

Ball S.J. 2014. Overview of modular htgr safety characterization and postulated accident behavior licensing strategy. ORNL. TM 187.

Banerjee A. and Andrews M.J. 2007. A Convection Heat Transfer Correlation for a Binary Air-Helium Mixture at Low Reynolds Number. Journal of Heat Transfer 129:1494–1505.

Beck J. and Pincock L. 2011. High temperature gas-cooled reactors lessons learned applicable to the next generation nuclear plant. Tech. rep., Idaho National Laboratory (INL).

Benjamin T.B. 1968. Gravity currents and related phenomena. Journal of Fluid Mechanics 31:209–248.

Birman V., Martin J., and Meiburg E. 2005. The non-boussinesq lock-exchange problem. part 2. high-resolution simulations. Journal of Fluid Mechanics 537:125–144.

Chapman S. and Cowling T.G. 1990. The mathematical theory of non-uniform gases: an account of the kinetic theory of viscosity, thermal conduction and diffusion in gases. Cambridge university press.

Chase Jr M.W. 1998. Nist-janaf thermochemical tables. J. Phys. Chem. Ref. Data, Monograph 9.

Dilling D., Dunn T., and Silady F. 1994. A vented low pressure containment strategy for the modular high temperature gas-cooled reactor (mhtgr). Tech. rep., General Atomics.

Dong Y. 2018. Design, safety features and progress of htr-pm. *In* Gen IV International Forum. Enero, pages 2018–02.

Ferng Y. and Chi C. 2012. Cfd investigating the air ingress accident for a htgr simulation of graphite corrosion oxidation. Nuclear engineering and design 248:55–65.

Gauthier J.C., Brinkmann G., Copsey B., and Lecomte M. 2006. Antares: The htr/vhtr project at framatome anp. Nuclear Engineering and Design 236:526–533.

General Atomics. 1996. Gas turbine-modular helium reactor (gt-mhr) conceptual design description report. GA Project 7658.

GIF. 2014. Technology roadmap update for generation iv nuclear energy systems. *In* OECD Nuclear Energy Agency, vol. 17.

Ham T.K., Arcilesi D.J., Kim I.H., Sun X., Christensen R.N., and Oh C.H. 2013. On the effects of containment design to gt-mhr air-ingress accidents. Transactions 109:316–319.

Haque H. 2008. Consequences of delayed air ingress following a depressurization accident in a high temperature reactor. Nuclear Engineering and Design 238:3041–3046.

Haynes M., Moreno E., and Owens M. 2017. Evaluation and testing of htgr reactor building response to depressurization accidents.

Hicks T. 2011. Modular htgr safety basis and approach. Tech. rep., Idaho National Laboratory (INL).

Hishida M. and Takeda T. 1991. Study on air ingress during an early stage of a primary-pipe rupture accident of a high-temperature gas-cooled reactor. Nuclear Engineering and Design 126:175–187.

Ishii M., Revankar S., Leonardi T., Dowlati R., Bertodano M., Babelli I., Wang W., Pokharna H., Ransom V., Viskanta R., *et al*. 1998. The three-level scaling approach with application to the purdue university multi-dimensional integral test assembly (puma). Nuclear Engineering and Design 186:177–211.

Kadoya K., Matsunaga N., and Nagashima A. 1985. Viscosity and thermal conductivity of dry air in the gaseous phase. Journal of physical and chemical reference data 14:947–970.

Kim E.S., Oh C., Schultz R., and Petti D. 2008. Analysis on the density driven air-ingress accident in vhtrs. Tech. rep., Idaho National Laboratory (INL).

Lemmon E.W., Jacobsen R.T., Penoncello S.G., and Friend D.G. 2000. Thermodynamic properties of air and mixtures of nitrogen, argon, and oxygen from 60 to 2000 k at pressures to 2000 mpa. Journal of physical and chemical reference data 29:331–385.

Li F., Chen F., Wang H., Dong Y., and Zhang Z. 2020. One implementation of vented low pressure containment for htr. Nuclear Engineering and Design 356:110412.

Lowe R.J., Rottman J.W., and Linden P. 2005. The non-boussinesq lock-exchange problem. part 1. theory and experiments. Journal of Fluid Mechanics 537:101–124.

Mason E.A. and Saxena S.C. 1958. Approximate formula for the thermal conductivity of gas mixtures. The Physics of Fluids 1:361–369.

McDowell B.K., Nickolaus J.R., Mitchell M.R., Swearingen G.L., and Pugh R. 2011. High temperature gas reactors: Assessment of applicable codes and standards. Tech. rep., Pacific Northwest National Lab.(PNNL), Richland, WA (United States).

Moe W. 2010. Htgr mechanistic source terms white paper. Tech. rep., Idaho National Laboratory (INL).

Moses D.L. 2010. Very high-temperature reactor (vhtr) proliferation resistance and physical protection (pr&pp). ORNL/TM-2010/163, Oak Ridge National Laboratory, Oak Ridge, Tennessee .

Oh C. 2006. Development of safety analysis codes and experimental validation for a very high temperature gas-cooled reactor final report. Tech. rep., Idaho National Laboratory (INL).

Oh C.H. and Kim E.S. 2010. Air ingress analysis: Computational fluid dynamics models. *In* International Heat Transfer Conference, vol. 49422, pages 337–346.

Omega Engineering, Inc. 2018. FMA900A SERIES, Air Velocity Transmitter With One SPST Relay Contact Closure: User's Guide. Omega Engineering, Inc., United States.

Petersen H. 1970. The properties of helium: density, specific heats, viscosity, and thermal conductivity at pressures from 1 to 100 bar and from room temperature to about 1800 k. Tech. Rep. Risoe-R No. 224, Risø National Laboratory, Denmark.

Pioro I. and Duffey R. 2018. Current and future nuclear-power reactors and plants,(pp. 117-197), chapter 4 in book: Managing global warming, an interface of technology and human issues, t. letcher.

Reitsma F., Strydom G., De Haas J., Ivanov K., Tyobeka B., Mphahlele R., Downar T., Seker V., Gougar H.D., Da Cruz D., *et al*. 2006. The pbmr steady-state and coupled kinetics core thermal-hydraulics benchmark test problems. Nuclear Engineering and Design 236:657–668.

Reyes Jr J., Groome J., Woods B., Jackson B., and Marshall T. 2010. Scaling analysis for the high temperature gas reactor test section (grts). Nuclear Engineering and Design 240:397–404.

Rotunno R., Klemp J., Bryan G., and Muraki D. 2011. Models of non-boussinesq lock-exchange flow. Journal of fluid mechanics 675:1–26.

Silberberg M.B. 2017. Design and Preliminary Measurements Inside a Simplified High Temperature Gas-Cooled Reactor Building. Ph.D. thesis, Texas A&M.

Simnad M.T. 1991. The early history of high-temperature helium gas-cooled nuclear power reactors. Energy 16:25–32.

SST Sensing Ltd. 2017. Zirconium Dioxide OXY-LC Interface Board User's Guide. SST Sensing Ltd., Coatbridge, United Kingdom.

SST Sensing Ltd. 2018. What is a zirconium dioxide oxygen sensor?

Subki H. 2020. Advances in small modular reactor technology developments. IAEA Advanced Reactors Information System (ARIS) .

Takeda T. 2008. Air ingress phenomena in a depressurization accident of the very-high-temperature reactor. *In* High Temperature Reactor Technology, vol. 48548, pages 633–640.

Takeda T., Hishida M., Imanishi S., and Takenaka S. 1996. Analysis of air ingress process during the primary-pipe rupture accident of the htgr. *In* Proceedings of the 3rd JAERI symposium on HTGR technologies, pages 272–288, Japan Atomic Energy Research Inst., Tokyo, Japan.

Yan X. 2016. Very high-temperature reactor. *In* Handbook of Generation IV Nuclear Reactors, pages 55–90, Elsevier.

Yang S.R., Kappes E., Nguyen T., Vaghetto R., and Hassan Y. 2018. Experimental study on 1/28 scaled ngnp htgr reactor building test facility response to depressurization event. Annals of Nuclear Energy 114:154–164.

Yildiz M.A. 2017. Numerical Analysis of 1/28 Scaled HTGR Reactor Building Test Facility Response to Depressurization Event. Ph.D. thesis, Texas A&M.

APPENDIX A

Fluid and Solid Material Properties

This section summarizes the thermophysical properties of the materials used in this study. The units of the correlations and values displayed in this section are in accordance with the International System of Units (SI) or metric system. These units are: temperature - K, density - kg/m^3, thermal conductivity - W m^{-1} K^{-1}, dynamic viscosity - kg m^{-1} s^{-1}, isobaric specific heat capacity - J kg^{-1} K^{-1}.

A.1 AIR

Air is assumed to be only composed of 78.12% N_2, 20.96% O_2, and 0.92% Ar. This means that the concentration of carbon dioxide is neglected. The thermophysical properties of air are display below (Lemmon *et al.*, 2000; Kadoya *et al.*, 1985). These correlations are valid for a temperature range of 100 K to 3000 K at an atmospheric pressure.

$$\rho(T_f) = \frac{345.57}{T_f - 2.6884} \tag{A.1}$$

$$\mu(T_f) = 2.5914x10^{-15}T_f^3 - 1.4346x10^{-11}T_f^2 + 5.0523x10^{-8}T_f + 4.1130x10^{-6} \tag{A.2}$$

$$Cp(T_f) = 1.3864x10^{-10}T_f^4 - 6.4747x10^{-7}T_f^3 + 1.0234x10^{-3}T_f^2 - 0.43282T_f + 1061.3 \tag{A.3}$$

A.2 HELIUM

The thermophysical properties of helium were computed based on the correlations presented below (Chase Jr, 1998; Petersen, 1970).

$$\rho(T_f,P) = 48.14x10^{-5}\frac{P}{T_f}\left[1+0.4446x10^{-5}\frac{P}{T_f^{1.2}}\right] \tag{A.4}$$

$$\begin{aligned} Cp(T_f) = \frac{1}{MW}\Bigg[&20.78603+4.850638x10^{-10}\left(\frac{T_f}{1000}\right)-1.582916x10^{-10}\left(\frac{T_f}{1000}\right)^2 \\ &+1.525102x10^{-11}\left(\frac{T_f}{1000}\right)^3+\frac{3.196347x10^{-11}}{(T_f/1000)^2}\Bigg] \end{aligned} \tag{A.5}$$

$$k(T_f,P) = 2.682x10^{-3}\big(1.0+1.123X10^{-8}P\big)T_f^{[0.71(1.0-2.0x10^{-9}P)]} \tag{A.6}$$

$$\mu(T_f) = 3.674x10^{-7}T_f^{0.7} \tag{A.7}$$

APPENDIX B

PYTHON SCRIPT FILE

---

upquote

upquote

```
# -*- coding: utf-8 -*-
"""
Created on Tue Aug 24 11:36:00 2021

@author: Silvino A. Balderrama Prieto
Email: sbalderrama@uidaho.edu

The following code calculates the depressurization of the RPV
and pressurization of the cavity assuming a polytropic process
"""
# =========================== PACKAGES ============================
# Import packages
import math
import pandas as pd
import matplotlib.pyplot as plt
# =========================== FUNCTIONS ===========================
# Ideal gas law equation
def ideal_gas_law(P_IG, rho_IG, MW_IG):
    # Calculate temperature
    return (P_IG*MW_IG)/(R*rho_IG)
# Function to calculate temperature at the throat when flow is choked
def outlet_temp(T_o, M_t, gamma_t):
    return T_o*(1.0-((gamma_t-1.0)/2.0)*M_t**2.0)**(-1.0)
# Function to calculate density at the throat when flow is choked
def outlet_rho(rho_o, M_t, gamma_t):
    return rho_o*(1.0+((gamma_t-1.0)/2.0)*M_t**2.0)**(-1.0/(gamma_t-1.0))
# Function to calculate the speed of sound in ideal gas
```

```
def velocity(T_t, M_t, gamma_t, MW_t):
    return M_t*(gamma_t*(R/MW_t)*T_t)**(0.5)
# Function to calculate the rate of change of density with respect to time
def drho_dt(rho_o, A, M_t, gamma_t, MW_t):
    # Calculate density at throat
    rho_t = outlet_rho(rho_o, M_t, gamma_t)
    # Calculate temperature at throat
    T_t = outlet_temp(T_o, M_t, gamma_t)
    # Calculate velocity at throat
    v_t = velocity(T_t, M_t, gamma_t, MW_t)
    # Calculate mass flow rate at throat
    m_dot=Cd*rho_t*A*v_t
    # Calculate change of density in the vessel
    drho_dt_vessel = -m_dot/V_V
    # Calculate change of density in the cavity
    drho_dt_cavity = m_dot/V_C

    return drho_dt_vessel, drho_dt_cavity, m_dot
# Density function for helium
def density_helium(T_he, P_he):
    return 48.14e-5*(P_he/T_he)*(1.0+0.4446e-5*(P_he/T_he**1.2))
# Density function for air
def density_air(T_air):
    return 345.57*(T_air-2.6884)**(-1.0)

# ***********************************************************************
# ***********************************************************************
# ************************** INITIAL CONDITIONS *************************
# ***********************************************************************
# ***********************************************************************

# ---------------------------- Vessel -----------------------------
Ti_V = 140; # Initial temperature [C]
```

```
Pi_V = 137.45282+14.696; # Initial pressure [psia]

# ---------------------------- Cavity ----------------------------
Ti_C=21; # Initial temperature [C]
Pi_C=14.69; # Initial pressure [psia]
# ---------------------------- System ----------------------------
OD = 0.41;  # Vessel outlet diameter [in]
Vent_b = 10;# Ventilation base size [in]
Vent_h = 4; # Ventilation height size [in]
Cd = 0.90;   # Discharge coefficient
# ------------------------ Time settings -------------------------
t = 10000.0; # Total time to calculate depressurization [sec.]
dt = 0.05; # Time-step [sec.]

# ********************** CHANGE TO SI UNITS *********************

# ---------------------------- Vessel ----------------------------
Ti_V = Ti_V+273.15; # C to K
Pi_V = Pi_V*6894.7572931783; # psi to Pa

# ---------------------------- Cavity ----------------------------
Ti_C = Ti_C+273.15; # C to K
Pi_C = Pi_C*6894.7572931783; # psi to Pa
# ---------------------------- System ----------------------------
Vb = Vent_b/39.37; # in to m
Vh = Vent_h/39.37; # in to m
d_star = OD/39.37; # in to m

# ************************** CONSTANTS **************************
V_V = 0.13835576; # Volume of vessel in m^3
V_C = 0.50448504; #Volume of cavity in m^3
Patm = 101325.0; # Atmospheric pressure [Pa]
Tatm = 298; # Atmospheric temperature [K]
```

```
gamma_he = 5.0/3.0; # Heat capacity ratio [-]
gamma_air = 1.005/0.718; # Heat capacity ratio of air [-]
R = 8.3144626; # University gas constant [J/mol-K]
MW_he = 4.002602*(1.0/1000.0); # Molecular weight of helium [kg/mol]
MW_air = 28.9645*(1.0/1000.0); # Molecular weight of air [kg/mol]
P_vent = 6894.7572931783+Patm

# ***********************************************************************
# ***********************************************************************
# ************************** MAIN CODE ********************************
# ***********************************************************************
# ***********************************************************************

# Create lists to append values
Pvessel = [Pi_V]
Pcav = [Pi_C]
Tvessel = [Ti_V]
Tcav = [Ti_C]
T_he = [0.0]
# Initial density in vessel
rhoi_V = density_helium(Tvessel[-1], Pvessel[-1])
rhoi_C = density_air(Tcav[-1]) # Initial density in cavity
rho_atm =density_air(Tatm)
dvessel = [rhoi_V]
dcav = [rhoi_C]
m_he = [0.0]           # Mass of helium in cavity
mole_fr_he = [0.0]     # Number of moles of helium in cavity
mole_fr_air = [1.0]    # Number of moles of air in cavity
mass_fr_he = [0.0]     # Mass fraction of helium in cavity
mass_fr_air = [1.0]    # Mass fraction of air in cavity
rho_he = [0.0]         # Density of helium in cavity
rho_air = [rhoi_C]     # Density of air in cavity
mdot = [0.0]
```

```
time = [0.0]

Mach = [0.0]

n = [gamma_he]#[gamma_he]

# Calculate initial mass of air in cavity

mass_air = rhoi_C*V_C

# Calculate initial number of moles of air in cavity

mole_air = (Pi_C*V_C)/(R*Ti_C)

# Calculate area of break

A_t = (math.pi/4.0)*d_star**2.0

# Area of ventilation system

A_vent = 1.0;

# Counter

counter = (int)((t-0.0)/dt)

# ======================= Initiate For loop =======================

for i in range(1,counter+1):

    # Evaluate if depressurization/pressurization is complete

    if Pvessel[-1]>Pcav[-1]:

        # Assign variables

        P_o=Pvessel[-1]      # Pressure of control volume

        rho_o=dvessel[-1]    # Density of gas in control volume

        T_o=Tvessel[-1]      # Temperature of gas in control volume

        MW_o=MW_he

        Pb=Pcav[-1]          # Outside pressure of control volume

        rho_b=dcav[-1]       # Outside density of control volume

        Tb=Tcav[-1]          # Outside temperature of control volume

        Pr=P_o/Pb            # Determine pressure ratio (Pr)

        gamma_ = gamma_he

        # Determine if the flow is choked

        if Pr>=((2.0/(gamma_+1.0))**(1.0/(1.0-(1.0/gamma_)))):

            # Mach number of 1 when flow is choked

            M_t = 1.0

        else:

            # Mach number for subsonic flow
```

```
    M_t =
    ((2.0/(gamma_-1.0))*((P_o/Pb)**((gamma_-1.0)/gamma_)-1.0))**0.5

[rho_V_temp, rho_C_temp, m_dot_new] =
drho_dt(rho_o, A_t, M_t, gamma_, MW_o)
# Calculate the change of density using a
#finite-difference approximation
# Change of density in vessel
rho_new_V = dvessel[-1] + rho_V_temp*dt
# Calculate new pressure using polytropic relationship
# Change of pressure in vessel
P_new_V = Pvessel[-1]*(rho_new_V/dvessel[-1])**n[-1]
# Calculate new temperature using ideal gas law
# Change of temperature in vessel
T_new_V = ideal_gas_law(P_new_V, rho_new_V, MW_o)
# Calculate the mass of helium in cavity
m_new_he = m_he[-1] + m_dot_new*dt
# Calculate the number of moles of helium in cavity
mole_he = m_new_he/MW_he
# Calculate mole fractions
mole_frac_new_he = mole_he/(mole_air+mole_he)
mole_frac_new_air = mole_air/(mole_air+mole_he)
# Calculate mass fractions
mass_frac_new_he = m_new_he/(mass_air+m_new_he)
mass_frac_new_air = mass_air/(mass_air+m_new_he)
# Calculate the density of helium and mixture in cavity
rho_new_he = rho_he[-1] + rho_C_temp*dt
rho_new_air = mass_air/(V_C*mole_frac_new_air)
rho_new_mix = rho_new_he*mole_frac_new_he+rho_new_air*mole_frac_new_air

# Calculate total pressure in cavity
P_new_mix = Pcav[-1]*(rho_new_mix/dcav[-1])**n[-1]
# Calculate partial pressures in cavity
```

```
    P_new_he = P_new_mix*mole_frac_new_he
    P_new_air = P_new_mix*mole_frac_new_air
    # Calculate new temperature using ideal gas law
    MW_mix = mole_frac_new_he*MW_he+mole_frac_new_air*MW_air
    T_new_mix = ideal_gas_law(P_new_mix, rho_new_mix, MW_mix)
    T_new_he = ideal_gas_law(P_new_he, rho_new_he, MW_he)
    T_new_air = ideal_gas_law(P_new_air, rho_new_air, MW_air)

    # Calculate properties of binary gas mixture
    rho_new_mix = rho_new_he*mole_frac_new_he+rho_new_air*mole_frac_new_air

    # Update time
    t_temp = time[-1]+dt
else:
    print(1.0-(rho_new_he/rho_new_air))
    # Stop for loop when depressurization is complete
    break
# Append results
time.append(t_temp)         # Time
dvessel.append(rho_new_V)   # Density of vessel
Pvessel.append(P_new_V)     # Pressure of vessel
Tvessel.append(T_new_V)     # Temperature of vessel
mdot.append(m_dot_new)      # Mass flow rate at pressure vessel outlet
dcav.append(rho_new_mix)    # Density of cavity
Pcav.append(P_new_mix)      # Pressure of cavity
Tcav.append(T_new_mix)      # Temperature of cavity
m_he.append(m_new_he)       # Mass of helium
mole_fr_he.append(mole_frac_new_he) # Mole fraction of helium
mole_fr_air.append(mole_frac_new_air) # Mole fraction of air
mass_fr_he.append(mass_frac_new_he) # Mass fraction of helium
mass_fr_air.append(mass_frac_new_air) # Mass fraction of air
T_he.append(T_new_he)       # Temperature of helium
T_he.append(T_new_he)       # Pressure of helium in cavity
```

```
    rho_he.append(rho_new_he)   # Density of helium in cavity
    rho_air.append(rho_new_air) # Density of air in cavity

# ***********************************************************************
# ***********************************************************************
# ******************************* PLOT RESULTS **************************
# ***********************************************************************
# ***********************************************************************

# ************ Plot mass flow rate ************
plt.title(label="Mass flow rate",fontsize=15)
plt.plot(time, mdot,'g')
plt.ylabel('Mass Flow Rate (kg/s)')
plt.xlabel('Time (sec.)')
plt.show()
# ************ Plot helium and air mole fractions in cavity ************
plt.title(label="Mole Fraction in Cavity",fontsize=15)
plt.plot(time, mole_fr_he,'g')
plt.plot(time, mole_fr_air,'b')
plt.ylabel('Mass Fraction (-)')
plt.xlabel('Time (sec.)')
plt.show()
# ************ Plot helium and air mass fractions in cavity ************
plt.title(label="Mass Fraction in Cavity",fontsize=15)
plt.plot(time, mass_fr_he,'g')
plt.plot(time, mass_fr_air,'b')
plt.ylabel('Mass (kg)')
plt.xlabel('Time (sec.)')
plt.show()
# ************ Plot density ************

# Vessel
plt.title(label="Density",fontsize=15)
```

```
plt.plot(time, dvessel,'r',label = "RPV")

plt.ylabel('Density (kg/m3)')

plt.xlabel('Time (sec.)')

plt.legend()

plt.show()

# Cavity

plt.plot(time, dcav,'b',label = "Cavity")

plt.ylabel('Density (kg/m3)')

plt.xlabel('Time (sec.)')

plt.legend()

plt.show()

# He and Air in Cavity

plt.plot(time, rho_he,'g',label = "Helium")

plt.plot(time, rho_air,'b',label = "air")

plt.ylabel('Density (kg/m3)')

plt.xlabel('Time (sec.)')

plt.legend()

plt.show()


# ************ Plot pressure ************

# Vessel

plt.plot(time, Pvessel,'r',label = "RPV")

plt.ylabel('Pressure (Pa)')

plt.xlabel('Time (sec.)')

plt.legend()

plt.show()

# Cavity

plt.plot(time, Pcav,'b',label = "Cavity")

plt.axhline(y=P_vent, color='r', linestyle='-', label='Max. pressure limit')

plt.ylabel('Pressure (Pa)')

plt.xlabel('Time (sec.)')

plt.legend()

plt.show()
```

```
# ************ Plot temperature ************
# Vessel
plt.plot(time, Tvessel,'r')
plt.ylabel('Temperature (K)')
plt.xlabel('Time (sec.)')
plt.show()

# Cavity
plt.plot(time, Tcav,'r')
plt.ylabel('Temperature (K)')
plt.xlabel('Time (sec.)')
plt.show()
```

APPENDIX C

Experimental Data

C.1 BASELINE EXPERIMENT 1

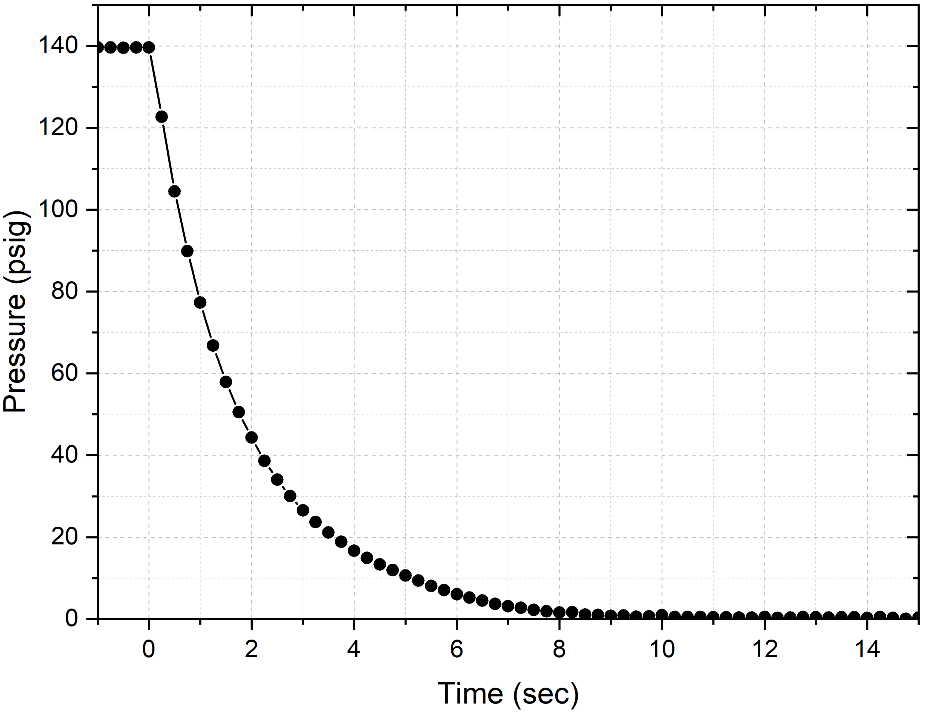

Figure C.1: Pressure evolution for experiment #1.

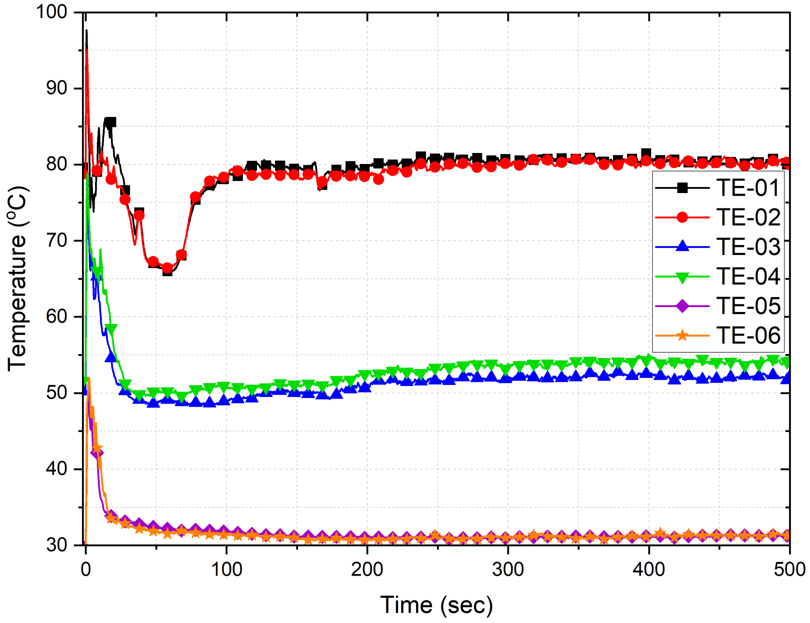

Figure c.2: Temperature measured from sensors TE-01 through TE-06 for experiment #1.

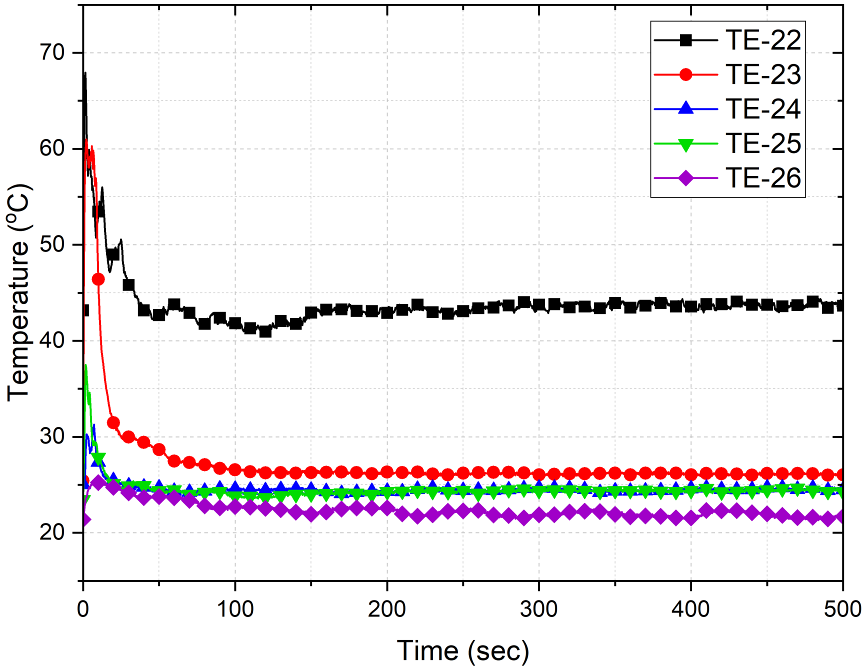

Figure c.3: Temperature measured from sensors TE-22 through TE-26 for experiment #1.

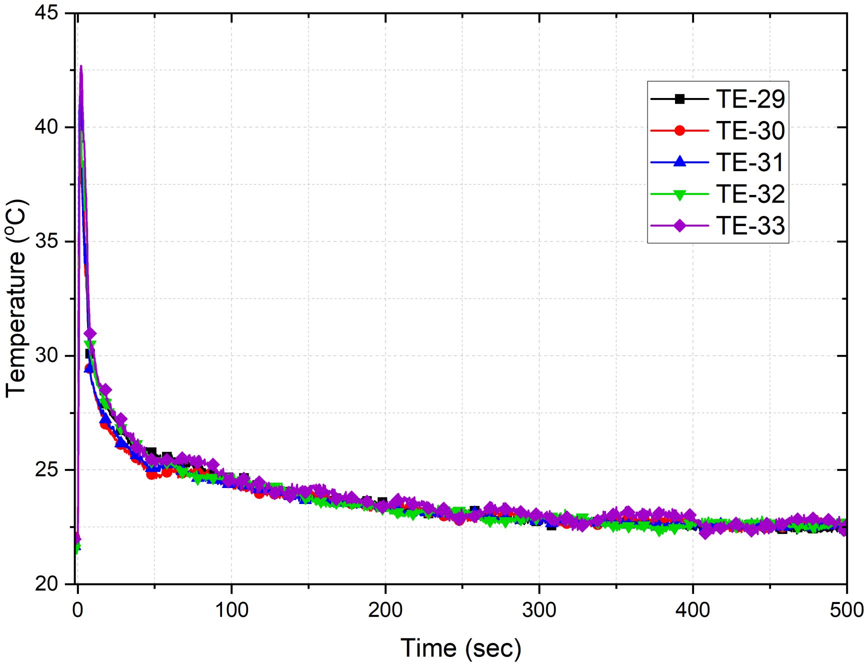

Figure c.4: Temperature measured from sensors TE-29 through TE-33 for experiment #1.

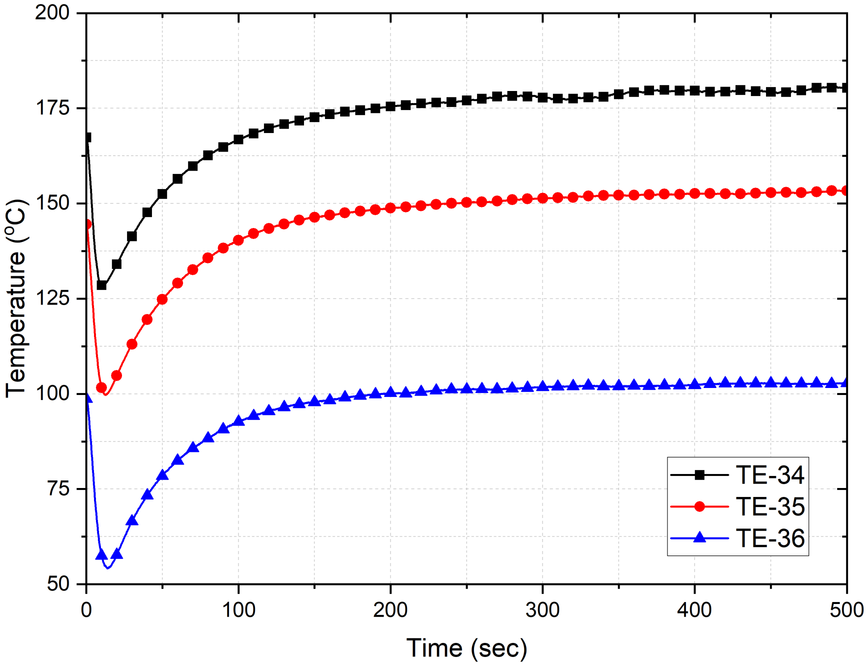

Figure c.5: Temperature measured from sensors TE-34 through TE-36 for experiment #1.

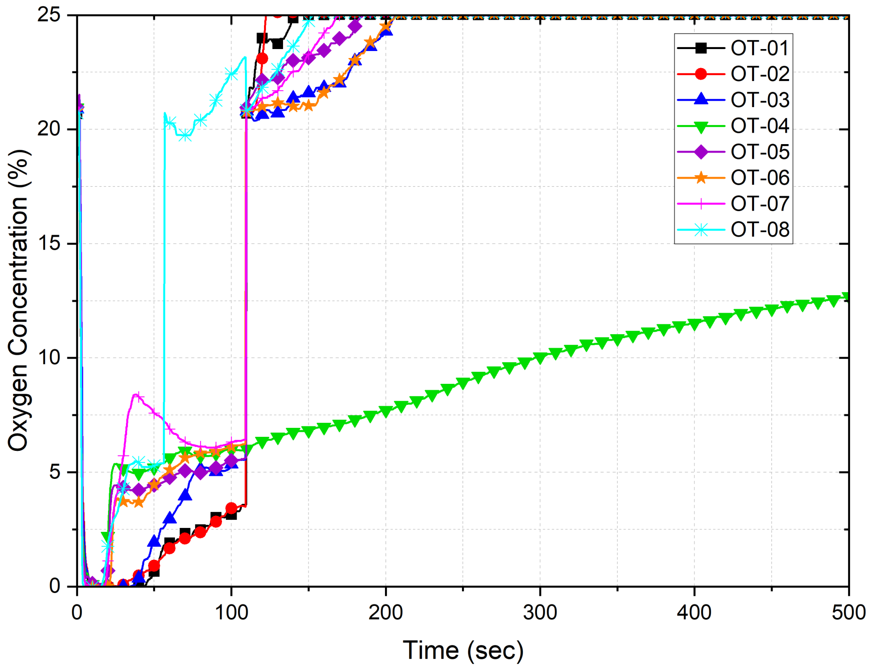

Figure c.6: Oxygen measured from sensors OT-01 through OT-08 for experiment #1.

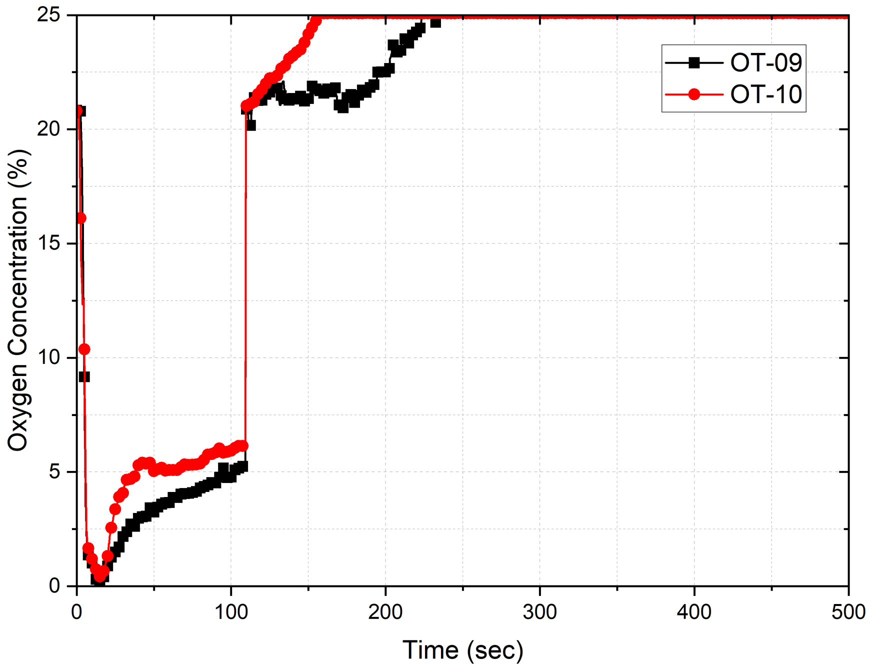

Figure c.7: Oxygen measured from sensors OT-09 through OT-10 for experiment #1.

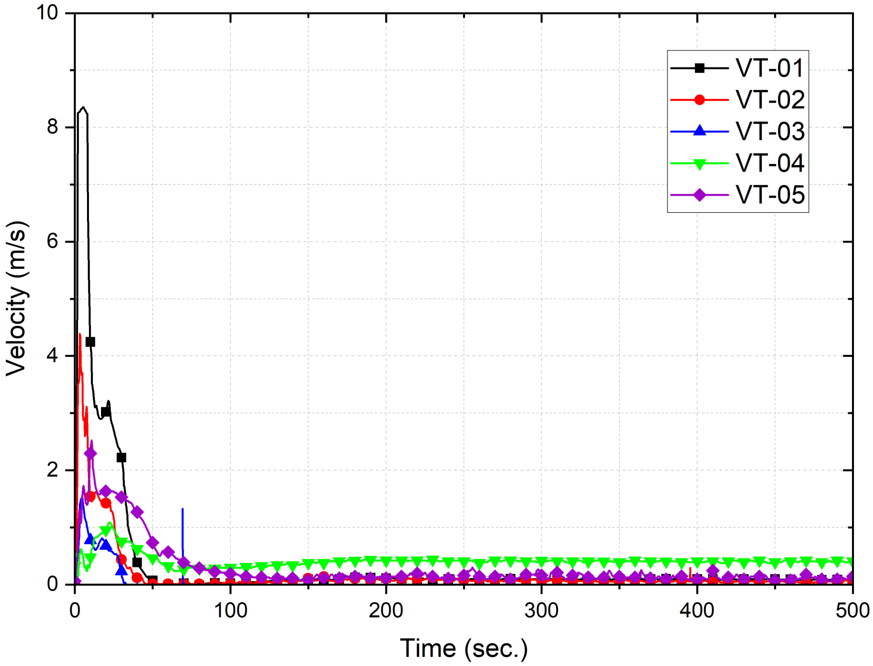

FIGURE C.8: Velocity measured from sensors VT-01 through VT-05 for experiment #1.

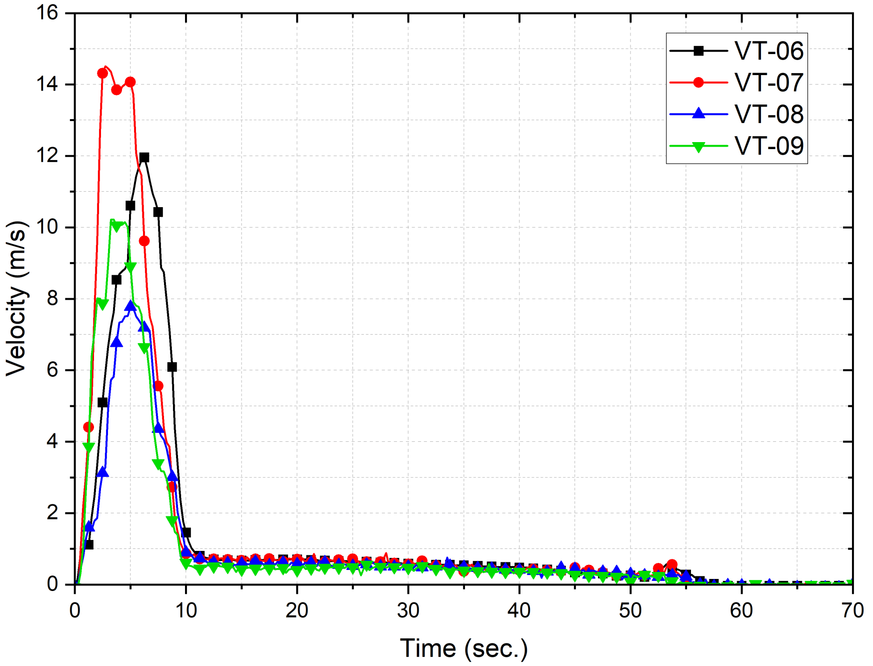

FIGURE C.9: Velocity measured from sensors VT-06 through VT-09 for experiment #1.

C.2 EXPERIMENT 4

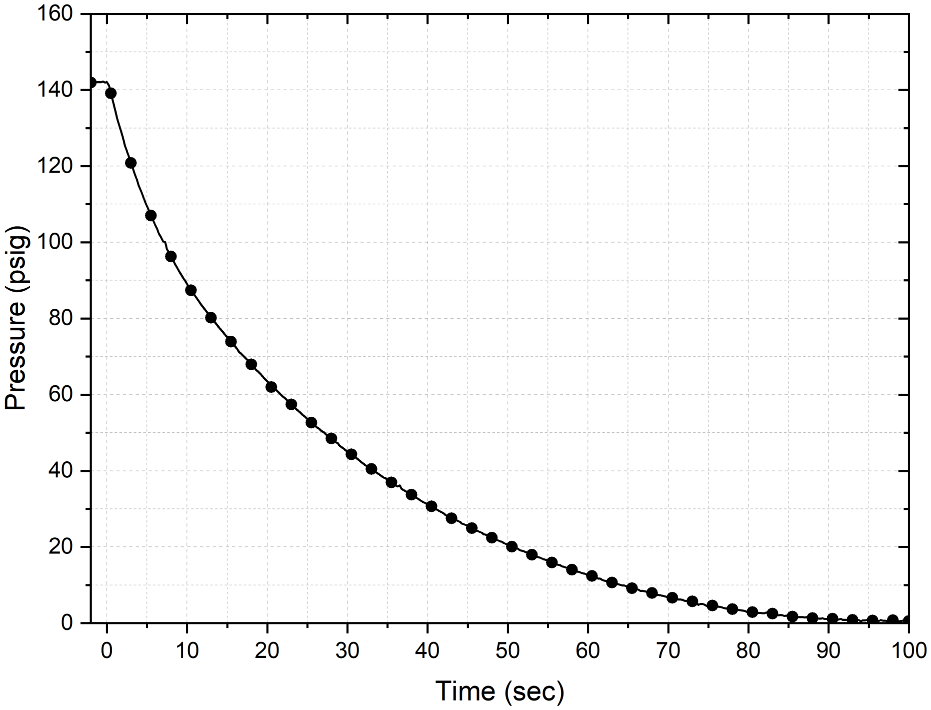

Figure C.10: Pressure evolution for experiment #4.

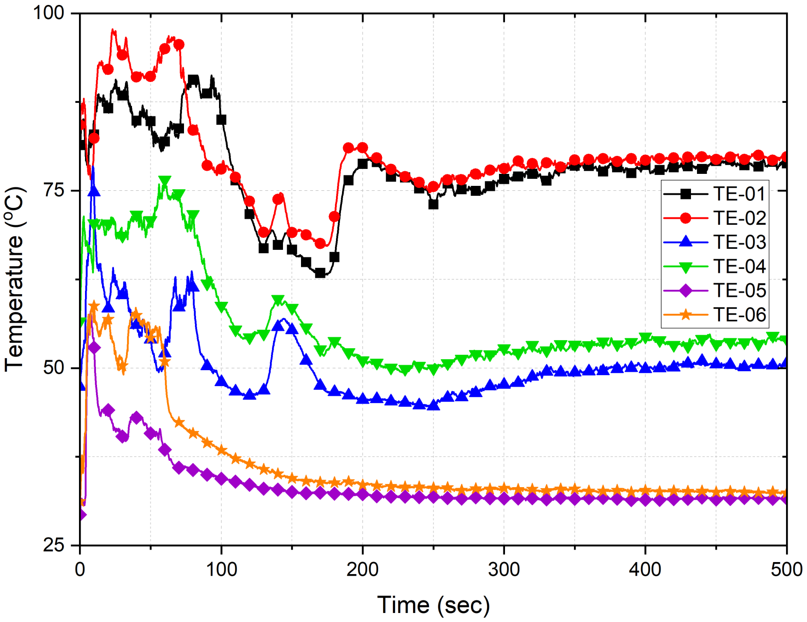

Figure C.11: Temperature measured from sensors TE-01 through TE-06 for experiment #4.

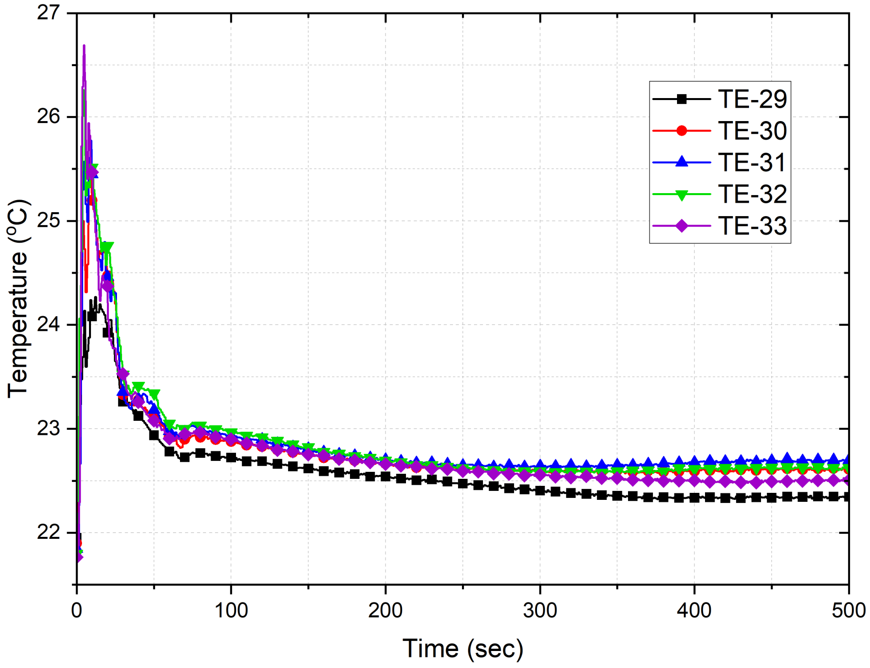

FIGURE C.12: Temperature measured from sensors TE-29 through TE-33 for experiment #4.

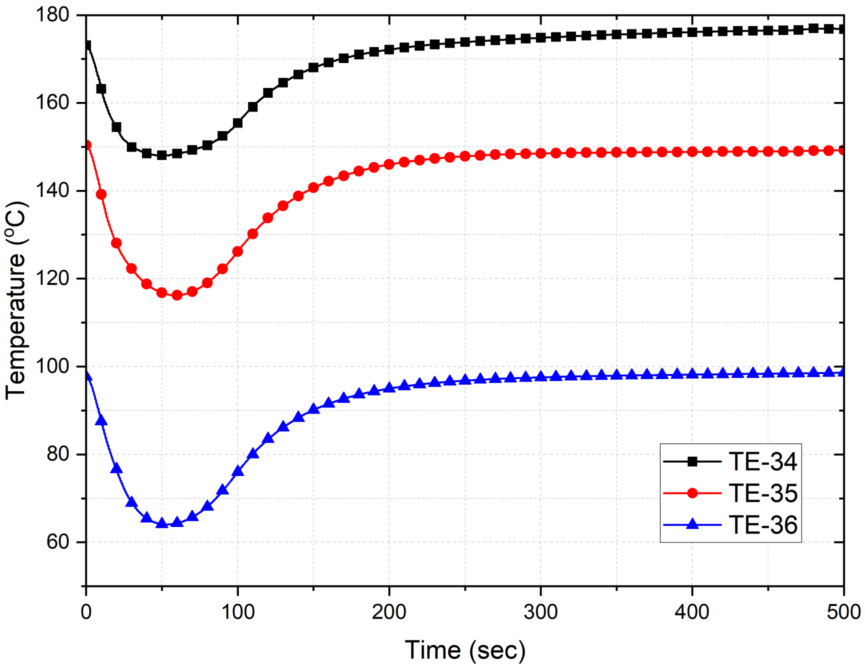

FIGURE C.13: Temperature measured from sensors TE-34 through TE-36 for experiment #4.

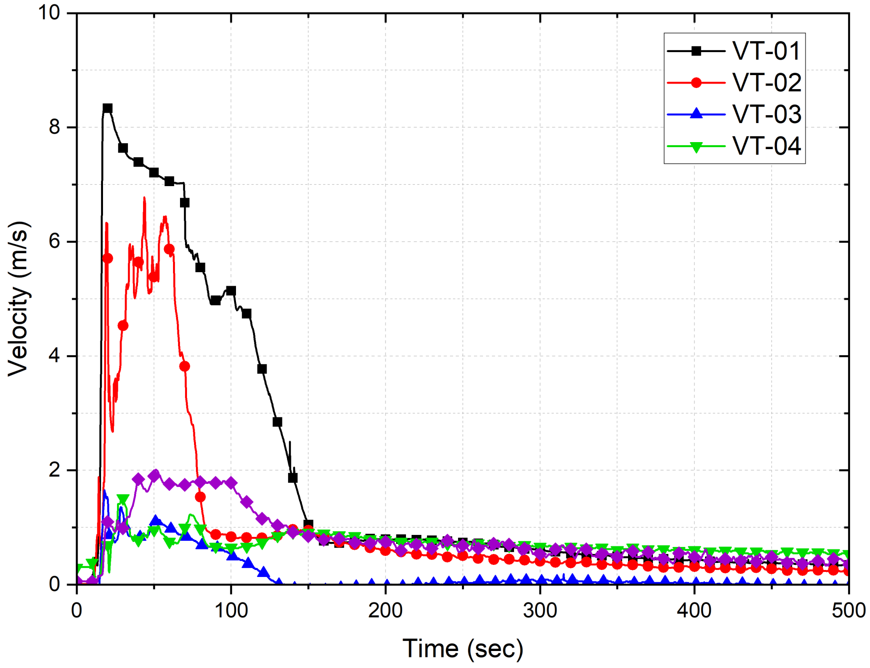

Figure c.14: Velocity measured from sensors VT-01 through VT-04 for experiment #4.

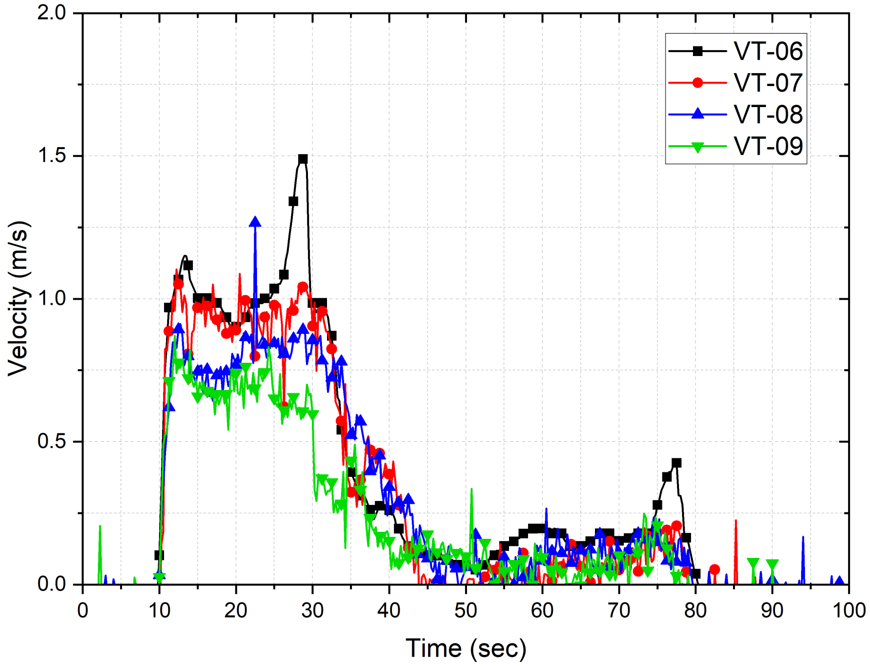

Figure c.15: Velocity measured from sensors VT-06 through VT-09 for experiment #4.

C.3 EXPERIMENT 12

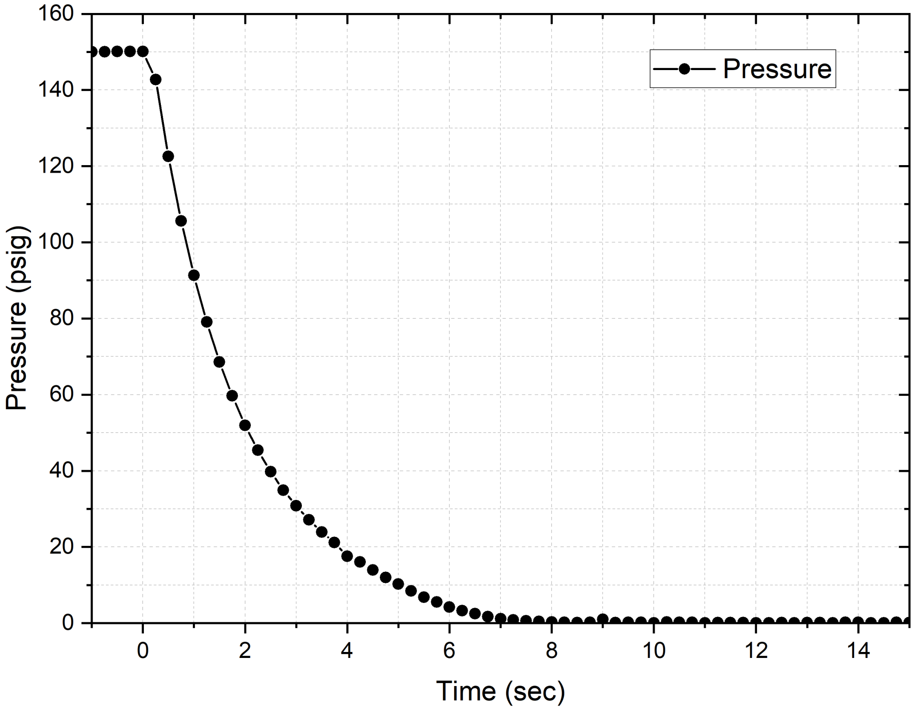

FIGURE C.16: Pressure evolution for experiment #12.

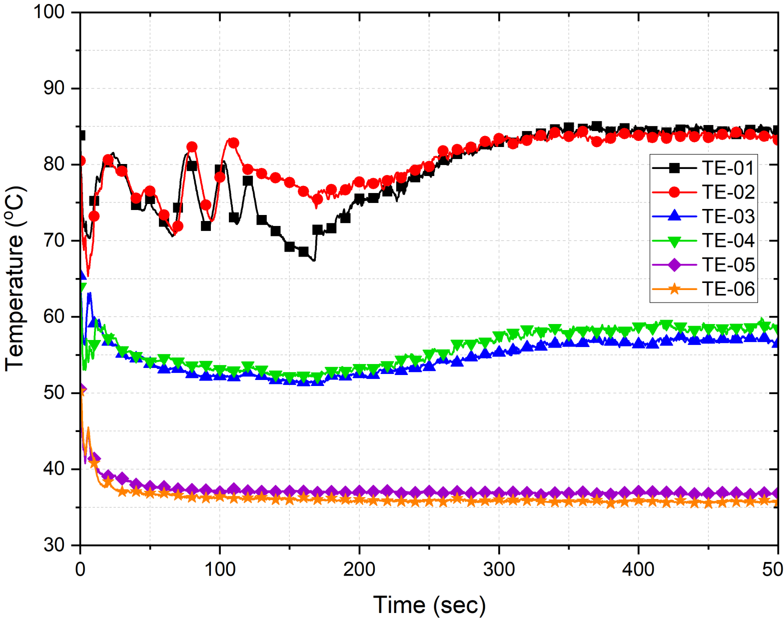

FIGURE C.17: Temperature measured from sensors TE-01 through TE-06 for experiment #12.

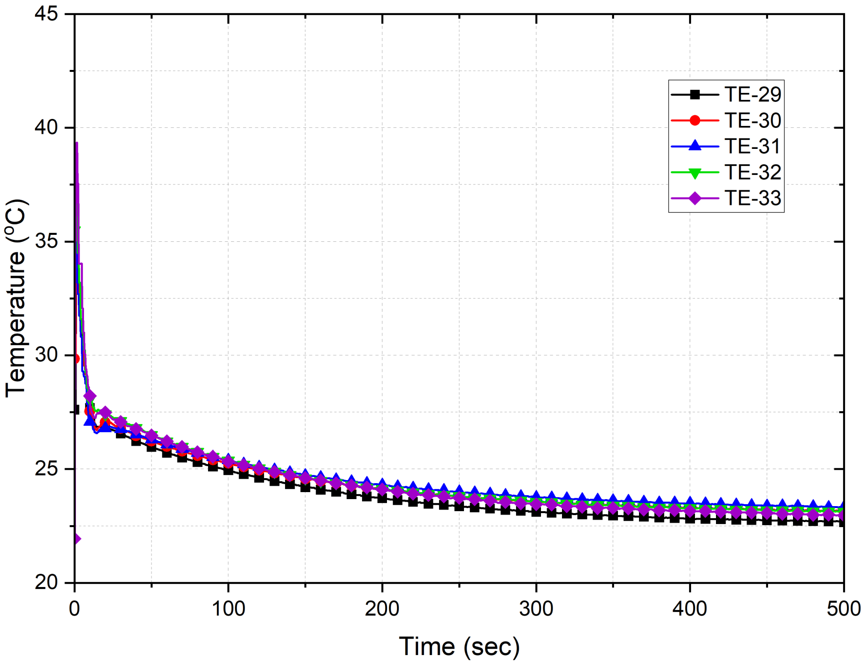

Figure c.18: Temperature measured from sensors TE-29 through TE-33 for experiment #12.

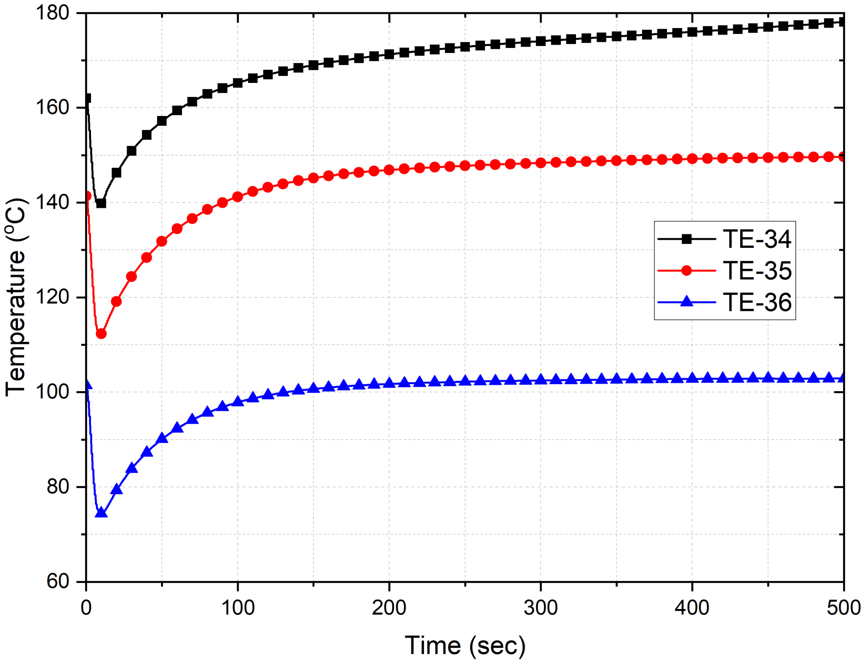

Figure c.19: Temperature measured from sensors TE-34 through TE-36 for experiment #12.

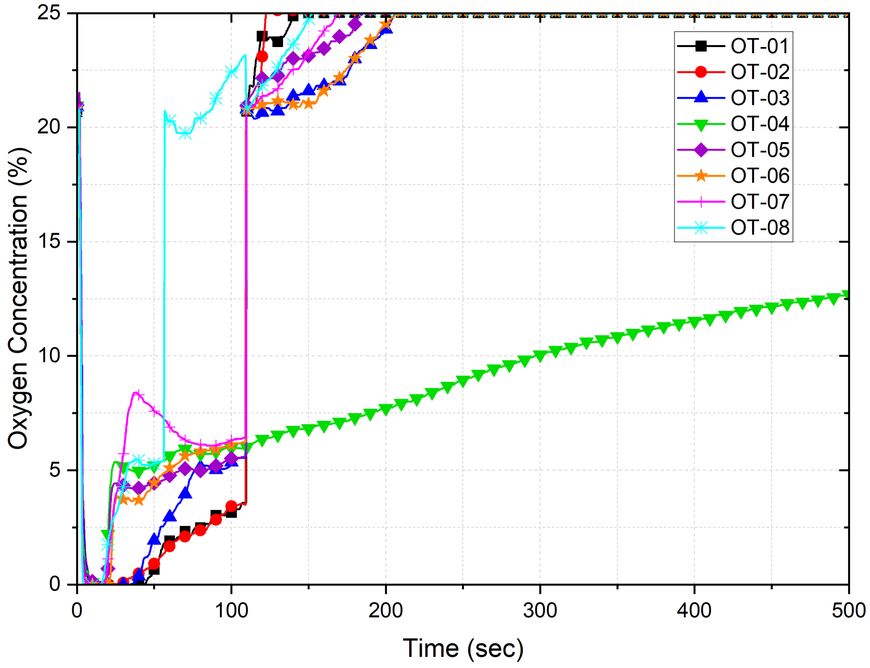

Figure c.20: Oxygen measured from sensors OT-01 through OT-08 for experiment #12.

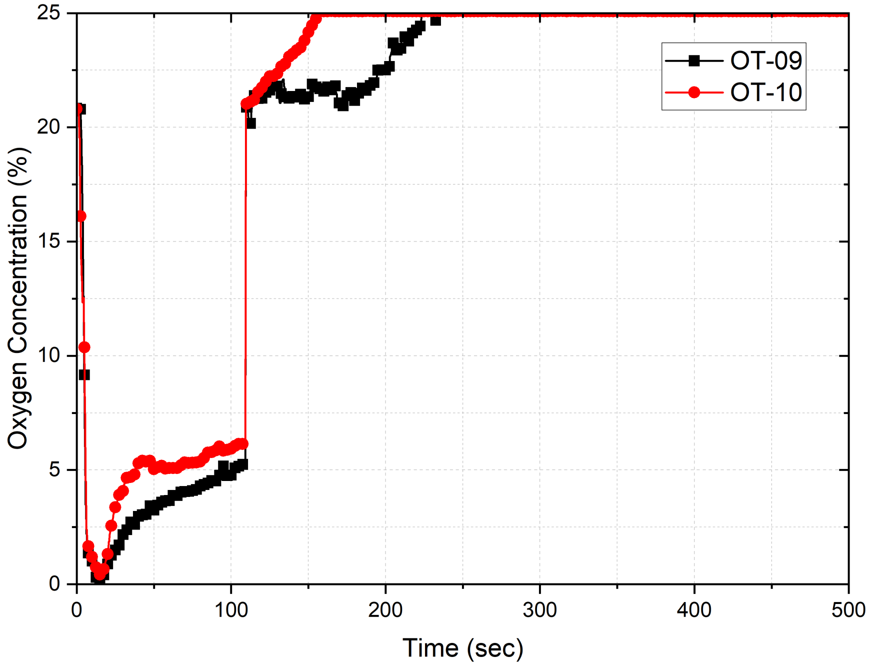

Figure c.21: Oxygen measured from sensors OT-09 through OT-10 for experiment #12.

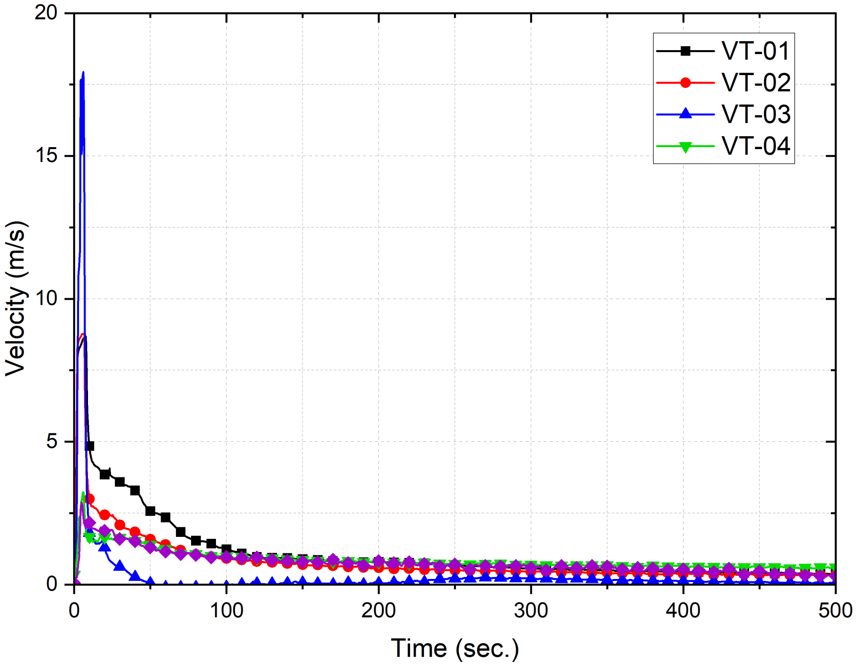

Figure C.22: Velocity measured from sensors VT-01 through VT-05 for experiment #12.

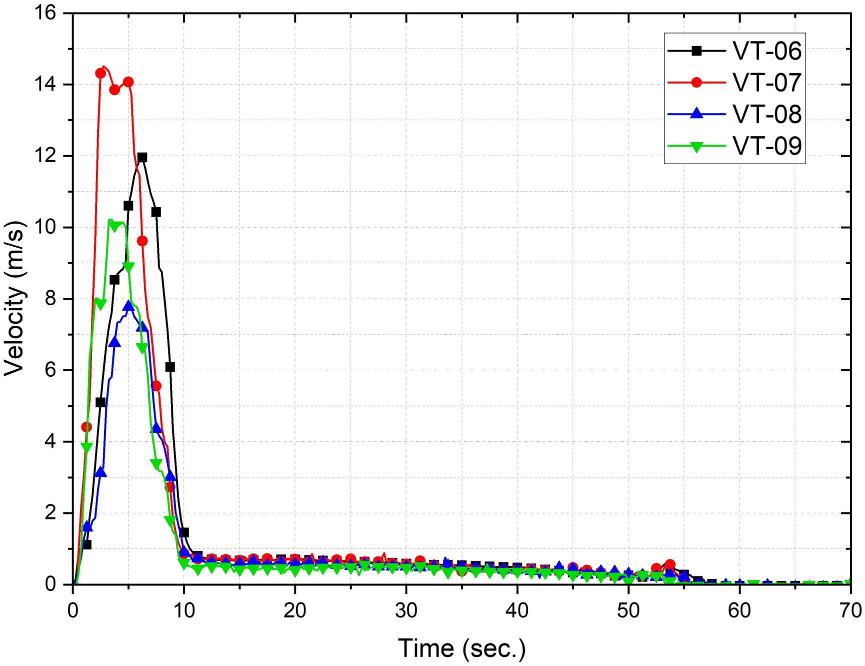

Figure C.23: Velocity measured from sensors VT-06 through VT-09 for experiment #12.